Title
A Tale of Two Planet(ary bodie)s: The Origin of Ice on Mercury and the Moon

Author
Rubanenko, Lior

Publication Date
2020

Peer reviewed|Thesis/dissertation

UNIVERSITY OF CALIFORNIA

Los Angeles

A Tale of Two Planet(ary bodie)s:
The Origin of Ice on Mercury and the Moon

A dissertation submitted in partial satisfaction

of the requirements for the degree

Doctor of Philosophy in Geophysics and Space Physics

by

Lior Rubanenko

2020

ABSTRACT

A Tale of Two Planet(ary bodie)s:
The Origin of Ice on Mercury and the Moon

by

Lior Rubanenko
Doctor of Philosophy in Geophysics and Space Physics
University of California, Los Angeles, 2020
Professor David A. Paige, Chair

The low obliquity of Mercury and the Moon causes topographic depressions located near their poles to cast persistent shadows, which may cold-trap volatiles for geologic time periods. Despite their similar thermal environments, telescopic and remote sensing observations have previously detected thick, pure water ice deposits near the poles of Mercury but not the Moon - where ice was found to be superficial or mixed with the regolith. This work attempts to resolve the apparent difference between the two planetary bodies employing physical models and spacecraft observations. We study how topographic roughness affects the temperature distribution and the ensuing prevalence of cold-traps, and constrain the amount, age and origin of polar ice deposits on Mercury and the Moon. Our results suggest that the difference between the amount of cold-trapped volatiles on these planetary bodies may not be as significant as previously thought, and that the presence of heavier carbonaceous volatiles on Mercury may explain the higher purity of its ice deposits relative to the Moon.

The dissertation of Lior Rubanenko is approved.

Seul Gi Moon

Hilke E. Schlichting

David Jewitt

David A. Paige, Committee Chair

University of California, Los Angeles

2020

לאילון,
שהביא עמו אור חזק מכל כוכב

TABLE OF CONTENTS

LIST OF FIGURES

LIST OF TABLES

ACKNOWLEDGMENTS

The work presented here could not have existed without the efforts of a number of people.

First and foremost, I wish to thank my collaborators. To Pierre Williams, Joshua Bandfield, Ben Greenhagen, and Matt Siegler for offering advice to a young eager planetary scientist. To Norbert Schrghofer, for posing impossible challenges and guiding me on my way to find a solution. To Paul Hayne, whose dedication inspired me to pursue this dream. To Tyler Powell, for sharing an office - but also ideas and endless chats. I will miss our improvised chalk-talks on the little whiteboard. To Jessica Ban who gracefully welcomed a stranger in a strange land.

To Oded Aharonson, my friend and my teacher. I will forever be in your debt for introducing me to planetary sciences. Your dedication and attention to details have taught me the value of carefulness and critical thinking. I wish to thank Dave Jewitt for his support and advice, and for teaching me that great scientific ideas often come from the lowest hanging fruits. To Hilke Schlichting, whose door was always open to hear my ideas and concerns. Thank you for inspiring me with optimism and confidence. To Seulgi Moon, whose insightful words and comments have vastly improved this work.

To David Paige, my advisor, who welcomed me to UCLA with open arms. Dave, I cannot thank you enough for the endless hours we spent discussing our work, and for teaching me the value of passive thinking. I will always aspire to adopt your approach to science, which is rare in this world. Thank you for your patience and guidance, and for showing me life within the academia can coexist with the outside world.

To my mom and dad, my siblings, Yaniv, Shlomit, Tamar and Noga, thank you for supporting me in the wildest years of my life. Thank you for the many hours you spent traveling, listening and encouraging. This work could not have happened without your complete (albeit sometimes exaggerated) confidence in my skills.

To my wife, Moran, and my son, Elon, who was born in the middle of this fantastic journey: this work is as yours as it is mine.

CHAPTER 1

Introduction

At first glance, Earth's Moon and Mercury are nearly indistinguishable. Both bodies are gray, rocky and airless, and have a tiny obliquity to the ecliptic plane. In 1952, The renown chemist and Nobel laureate Harold Urey suggested topographic depressions near the poles of the Moon may cast permanent shadows (Urey, 1952). Urey postulated that in the absence of atmospheric heat transport, these shadows may be sufficiently cold to trap volatiles. About a decade later, Watson et al. (1961) showed water ice may become cold-trapped inside these permanently shadowed regions (PSRs) for geologic time periods. Recently, Urey's clairvoyant prediction was found to be surprisingly accurate; ice was detected near the poles of both the Moon and Mercury (e.g. Harmon et al., 2001; Colaprete et al., 2010; Harmon et al., 2011; Paige et al., 2013; Chabot et al., 2014). However, the ice deposits on Mercury were found to be orders of magnitude thicker than the seemingly superficial deposits on the Moon. How could these nearly identical thermal environments produce such remarkable differences?

This question was the main motivation for the work presented here. The path to answering it began with understanding how topographic roughness affects the temperature of airless surfaces and the ensuing prevalence of cold-traps. It continued by exploring the origin and age of the smallest ice deposits on Mercury and the Moon, and concluded by synthesizing recent results with both analyzed and neglected, previously unanalyzed, remote sensing data.

The data employed throughout this work were collected by four prolific instruments on board two orbiters that explored the surfaces of Mercury and the Moon: the MErcury Surface, Space ENvironment, GEochemistry and Ranging (MESSENGER, Solomon et al.

(2001)) and the Lunar Reconnaissance Orbiter (LRO, Chin et al. (2007)). The Mercury Laser Altimeter (MLA, Cavanaugh et al. (2007)) and the Lunar Orbiter Laser Altimeter (LOLA, Smith et al. (2010)) sampled the planets' topography by timing the round-trip flight of infrared (1064 nm) laser pulses fired at their surface. Along with the topographic relief, these instruments also measured the surface reflectance as the ratio between the emitted and the absorbed beam power. The Mercury Dual Imaging System (MDIS, Hawkins et al. (2007)) and the Lunar Reconnaissance Orbiter Camera (LROC, Robinson et al. (2010)) photographed the surface of Mercury and the Moon down to a resolution of a 20 $\mathrm{m\,px^{-1}}$ and 0.5 $\mathrm{m\,px^{-1}}$, respectively. The lunar radiometer experiment (Diviner, Paige et al. (2010a)) measured the surface temperatures of the Moon at a resolution of $\sim 250\ \mathrm{m\,px^{-1}}$.

The surface temperature of the Moon and Mercury is dominated by insolation. The porous regolith covering these bodies is thermally insulating, and in the absence of atmospheric convection sharp temperature gradients form over short distances (Keihm and Langseth Jr, 1973; Langseth et al., 1976; Hayne et al., 2017). During the day, illuminated slopes quickly reach radiative equilibrium, while shadows are more affected by scattering from topography and heat diffusion into the subsurface (Bandfield et al., 2015; Rubanenko and Aharonson, 2017). Shortly after sunset, thermal emission from the warmest slopes still affects the surface temperature. However, this effect quickly subsides as warm slopes radiate heat faster than cold slopes (Rubanenko et al., 2017b).

Calculating the temperatures from this heat balance (Figure 1.1) is simple but computationally demanding due to the need to account for scattered and emitted flux from all nearby slopes. Sometimes, it is possible to estimate this flux by assuming the topography is composed of idealized shapes such as hemispherical craters (Buhl et al., 1968; Ingersoll et al., 1992) or Gaussian surfaces (Chapter 2). However, in the general case, there is no alternative but to use techniques such as Ray Casting (Roth, 1982). A modified version of this algorithm, which was popular in early 3-D video games (Kushner, 2002), is adopted here to simulate cast shadows and scattering from the surface. A full description of this thermal model may be found in chapter 2 of this work.

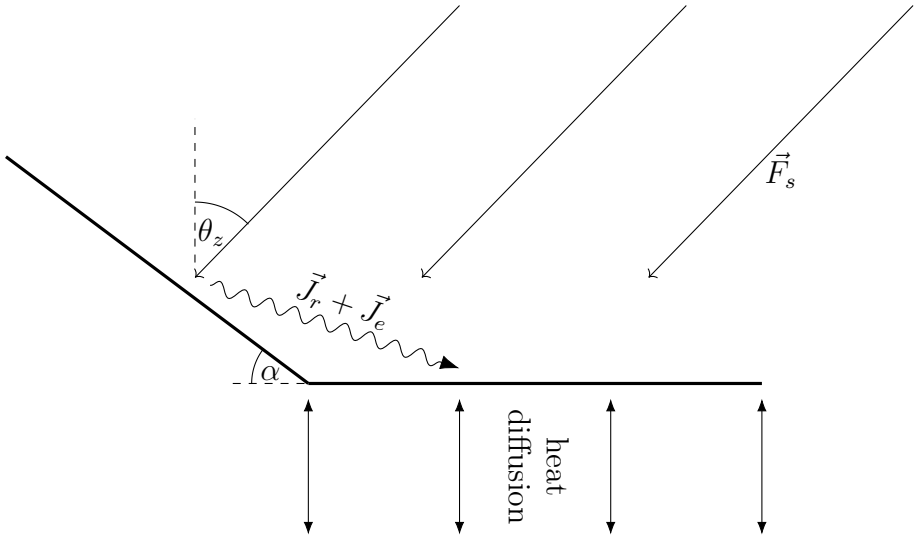

Figure 1.1: The radiation balance on a rough, airless surface is composed of insolation (F_s), reflected and emitted radiosity ($\vec{J}_r + \vec{J}_e$) and subsurface conduction. α is the slope angle, and θ_z is the solar zenith angle.

All rotating planetary bodies experience a diurnal change in the amount of insolation they receive, which affects their temperature. The amplitude of the temperature variation, often termed *the thermal wave*, decreases as it diffuses into the subsurface. It is sometimes convenient to define the thermal skin depth, or the depth at which the surface temperature decreases e-fold,

$$\delta = \sqrt{\frac{k}{\rho c}\frac{P}{2\pi}} \tag{1.1}$$

where P is the planetary body rotation rate, k is the thermal conductivity and ρc is the volumetric thermal heat capacity. For lateral scales larger than δ, it is possible to model heat diffusion into the subsurface by solving the 1-D thermal diffusion equation,

$$\rho c\frac{\partial T}{\partial t} = k\frac{\partial^2 T}{\partial z^2} \tag{1.2}$$

the thermal skin depth on airless, slowly rotating bodies such as Mercury and the Moon is of the order of a few decimeters. By calculating the surface and subsurface temperatures on Mercury and the Moon, it is possible to model how volatiles migrate on their surface.

Due to their weak gravity, Mercury and the Moon both have tenuous atmospheres; the

particles that compose them move in ballistic hops whose height h depends on their thermal energy,

$$h = \frac{2k_B T}{\mu g} \tag{1.3}$$

where T is the temperature, g is the gravitational acceleration of the planet, μ is the particle mass and $k_B \approx 1.38 \times 10^{-23}\ \mathrm{m^2\,kg\,s^{-2}\,K^{-1}}$ is the Boltzmann constant. The factor of two in the expression above is due to the particle's higher probability to travel upwards, being bounded by the surface below (Schorghofer, 2015). Table 1.1 shows the hop height h for three different types of volatiles on Mercury and the Moon. The time the molecules spend stuck to the surface between hops is called the residence time, the ratio between the number density of water molecules per unit area θ and the loss rate J_{tot},

$$\tau = \frac{\theta}{\alpha J_{tot}} \tag{1.4}$$

where α is a coefficient indicating how many molecules will be reflected from the surface upon impact (Schorghofer and Taylor, 2007).

If the thermal energy of the hopping molecule is sufficiently high, it will escape the gravity of the planet it was bound to. Conversely, molecules with very low thermal energies will become trapped for geologic time periods, nearly unable to leave the surface they landed on. Watson et al. (1961) calculated the rate at which volatile molecules will sublimate from an airless surface,

$$E = \frac{P_v(T)}{\sqrt{2\pi k T \mu}} \tag{1.5}$$

where $P_v(T)$ is the temperature dependent saturation vapor pressure of the molecule. As an example, Figure 1.2 shows the sublimation rate of exposed water molecules. At low enough temperatures, molecules may become cold-trapped for geologic time periods. The exact value of the sublimation threshold defining these cold-traps varies in the literature, ranging from 1 $\mathrm{mm\,Ga^{-1}}$ to 1 $\mathrm{m\,Ga^{-1}}$ (e.g. Watson et al., 1961; Arnold, 1979; Lanzerotti et al., 1981; Paige et al., 1992, 2010b). However, for $E < 1\ \mathrm{m\,Ga^{-1}}$, other temperature independent destruction mechanisms such as UV photolysis (Lyα), space weathering and impact gardening dominate over spontaneous sublimation (Figure 1.2) (Lanzerotti et al., 1981; Morgan and Shemansky,

	g ($m\,s^{-2}$)	T (K)	h (km)		
			H_2O	CO_2	Xe
Mercury	3.7				
Equator maximum		600	150	62	20
Equator minimum		100	25	10	3
Polar Crater PSR		180	45	18	6
Moon	1.6				
Equator maximum		400	230	41	32
Equator minimum		90	52	9	7
Polar Crater PSR		110	65	11	9

Table 1.1: Temperatures and hop scale for water, CO_2 and Xenon molecules on Mercury and the Moon. For Mercury, I show the modeled equatorial maximum and minimum temperatures (Vasavada et al., 1999). For the Moon, I show the measured maximum and minimum temperatures measured by the LRO Diviner radiometer (Williams et al., 2017). The PSR temperature was estimated based on the results of an analytic thermal model (Ingersoll et al., 1992)

1991; Schorghofer and Taylor, 2007). Consequently, a surface cold-trap is defined here as an area in which the sublimation rate never exceeds 1 $m\,Ga^{-1}$. For water ice, which will be the main subject of this work, this sublimation rate is achieved at the cold-trap temperature, $T_{ct} = 120$ K.

Unlike exposed volatiles, buried volatiles benefit from the protection of the overlaying regolith that acts both as a physical and as a diffusion barrier. Molecules sublimating from a buried deposit hop between the grains of the regolith covering it. The additional time it takes these molecules to randomly walk from pore to pore decreases the volatile sublimation rate. If σ is the surface molecular density and τ is the temperature dependent residence time, the mass flux between two adjacent subsurface layers at depths $z = z_n$ and $z_{n+1} = z + \ell$ is

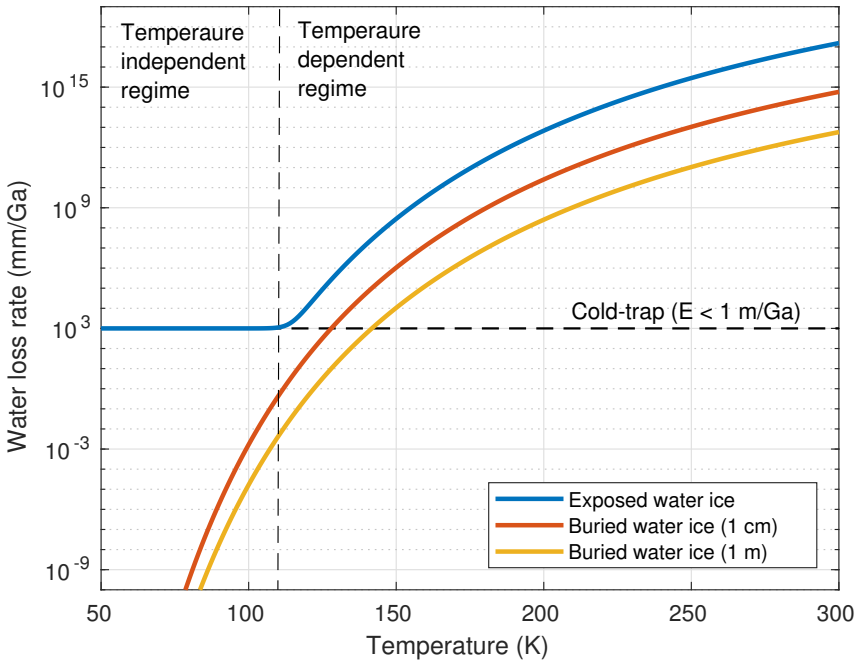

Figure 1.2: The sublimation rate into vacuum of exposed (blue) and buried (red, yellow) water molecules. Cold-traps are defined as areas in which the sublimation rate never exceeds $1\,\mathrm{m\,Ga^{-1}}$.

given by,

$$J(z) = -\frac{\mu}{2}\left(\frac{\sigma_{n+1}}{\tau_{n+1}} - \frac{\sigma_n}{\tau_n}\right) = -\frac{\mu\ell}{2}\frac{\partial}{\partial z}\left(\frac{\sigma_n}{\tau_n}\right) \tag{1.6}$$

where the factor of $1/2$ was added due to the equal probability of the molecule to travel up or down. We can now write the loss rate in terms in terms of the mass density, $\rho = \mu\sigma/\ell$,

$$J(z) = -\frac{\ell^2}{2}\frac{\partial}{\partial z}\left(\frac{\rho(z)}{\tau(z)}\right) \tag{1.7}$$

Below the thermal skin depth, the temperature dependent residence time is relatively constant. Assuming the amount of buried ice is much greater than the amount that can be buffered in the overlaying regolith, the density profile becomes linear (Schorghofer and Taylor, 2007). Its gradient can be determined by the difference between the surface density and the density at the ice-regolith boundary ($\mu\theta/\ell$),

$$J(z) = \frac{\ell^2}{2\tau}\frac{d\rho}{dz} = \frac{\ell}{2\tau}\frac{\mu\theta}{z} = \frac{\mu\ell}{2}\frac{E(T)}{z} \tag{1.8}$$

so the subsurface loss rate is simply the temperature dependent sublimation rate (Equation 1.5) scaled by the depth z. As can be seen in Figure 1.2, buried ice is significantly more durable than exposed ice. For example, the loss rate of ice buried at a depth of only 1 cm is two orders of magnitude lower than that of ice found on the surface.

This thesis is divided into six chapters: the first serves as an introduction, describes the problem and provides necessary background. The second chapter describes how surface roughness affects the temperature distribution of airless planetary bodies. The third discusses the link between the temperature distribution of a rough, airless surface and the ensuing prevalence of cold-traps with applications to the Moon. The fourth chapter applies numerical models and observations to estimate the thickness and prevalence of micro cold-traps on the surface of Mercury to estimate their age and origin. Chapter five explores the possibility the the thickness of the ice deposits on Mercury and the Moon may be smaller than previously thought. The sixth and final chapter concludes this work and proposes a potential explanation for the pristine cold-trapped ices on Mercury relative to the Moon.

CHAPTER 2

Equilibrium Temperatures and Directional Emissivity of Sunlit Airless Surfaces with Applications to the Moon

This chapter was submitted for publication in: Rubanenko L, Schorghofer, N., Greenhagen, B. T. and Paige, D. A., Equilibrium Temperatures and Directional Emissivity of Sunlit Airless Surfaces with Applications to the Moon. *Journal of Geophysical Research: Planets*. 2020.

Abstract

Solar irradiance dominates the heat flux incident on airless planetary bodies. In thermal equilibrium, surface roughness affects the temperature distribution by changing the incidence angle local to each slope. In order to simulate temperatures and thermal emissions at different phase angles, existing thermophysical models usually employ computationally expensive techniques such as ray-tracing. Here we derive the equilibrium surface temperature distribution of sunlit Gaussian rough surfaces, providing an exact solution for the sun at the zenith and an approximate solution for the general case. We find that although the slope distribution of realistic airless surfaces is often non-Gaussian, their temperature distribution is well-modeled assuming a Gaussian slope distribution. We additionally present closed-form expressions that describe the radiation emitted from rough surfaces at different emissions angles and employ them to radiometrically estimate the roughness of the lunar surface using measurements obtained by LRO Diviner. Our model may also be applied to studying the

surface roughness of both resolved and unresolved airless planetary bodies such as asteroids.

2.1 Introduction

The energy balance on the surface of airless planetary bodies is dominated by radiation which, in the absence of significant geothermal and atmospheric heat transport, causes steep temperature gradients over short horizontal distances. During the day, the main source of energy is incoming solar radiation (insolation). For slowly rotating planetary bodies with low near-surface thermal inertia, illuminated slopes quickly reach thermal equilibrium with incoming radiation (Spencer, 1990; Bandfield et al., 2015). As a result, the slope angle directly affects the temperature distribution by changing the incident solar flux vector.

The best studied airless planetary body in the solar system is Earth's Moon. A common way to characterize the lunar surface roughness is through its slope distribution (e.g. Smith, 1967b; Rosenburg et al., 2011a; Kreslavsky et al., 2013). The degree of roughness at a given lateral scale may be described by the root mean square (RMS) slope, and the dependence of the roughness on lateral scale is often expressed by a power law whose exponent is related to the well known Hurst exponent (Hurst, 1951; Schroeder, 2009). On the Moon, the RMS slope increases at smaller lateral scales (Figure 2.1a).

The Lunar Reconnaissance Orbiter (LRO) studies the lunar surface roughness employing laser altimetry (Smith et al., 2010), visible imagery (Robinson et al., 2010) and IR emission (Paige et al., 2010a) and radar (Nozette et al., 2010). The effect of subpixel topography on the temperature distribution may be numerically or analytically modeled assuming the surface is composed of idealized topographic features. Buhl et al. (1968) described topographic roughness as a collection of hemispherical bowl-shaped cavities and modeled the daytime temperature of the Moon. Later, Ingersoll et al. (1992), Hayne and Aharonson (2015) and others adopted similar methods to model ice stability on the Moon and the dwarf planet Ceres. Another common practice is to assume the surface slopes have a Gaussian distribution (Hagfors, 1964; Smith, 1967b; Jamsa et al., 1993; Lagerros, 1997; Li et al., 1999; Adler, 2010;

Rozitis and Green, 2011; Davidsson et al., 2015; Bandfield et al., 2015; Rubanenko and Aharonson, 2017). These so-called Gaussian surfaces have uniformly distributed phases in Fourier space, and can accommodate any power spectrum and spatial correlation function.

Nearly a century ago, Pettit and Nicholson (1930) and others observed that emitted thermal radiation flux across the lunar disc decreases more slowly than the cosine of the emission angle expected from a Lambert surface. Similarly, Sinton (1962) measured the infrared brightness of the subsolar point of the Moon and determined its angular dependence is different than that of a Lambert sphere. A few studies have since attempted to explain this deviation. Smith (1967b) and Buhl et al. (1968) modeled the effect of surface roughness of unresolved features on the directional emissivity, as different parts of the surface are seen or obstructed when viewed from different observation angles. Others have employed granular scattering (e.g. Hapke, 1981, 1986) or geometric scattering (e.g. Hagfors, 1970; Vogler et al., 1991) to describe this effect, sometimes termed the *thermal phase function*. More recently, Bandfield et al. (2015) compared different spectral channels of the Diviner lunar radiometer experiment on board LRO (Paige et al., 2010a) to relate the surface anisothermality to its subpixel RMS slope distribution at the thermal isolation scale. The directional dependence of infrared emissivity has also been studied extensively for terrestrial surfaces (e.g., Sobrino and Cuenca, 1999).

Here we consider Gaussian topography and Lambert radiation to model the temperature distribution of airless surfaces. In section 2.2 we derive two separate analytical models to calculate the equilibrium temperature distribution of sunlit rough Gaussian surfaces and their directional emissivity - the radiation they emit at different emission (observation) angles. In section 2.3, we apply our models to radiometrically estimate the roughness of the Moon at the thermal isolation scale.

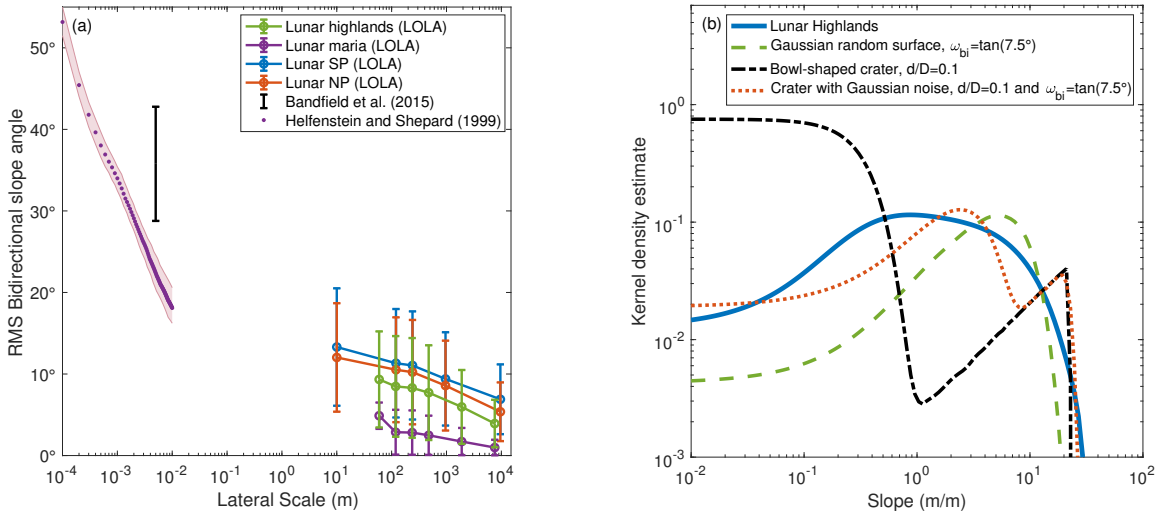

Figure 2.1: (a) The surface roughness of the Moon decreases with scale. We quantify the surface roughness by calculating the bi-directional RMS slope angle measured using altimetry data obtained by the Lunar Orbiter Laser Altimeter (LOLA). RMS slope on scales < 1 cm is based on estimates by Bandfield et al. (2015) and Helfenstein and Shepard (1999). Error bars indicate one standard deviation. (b) The bi-directional slope angle distribution of the lunar highlands at the 240 m baseline compared to three commonly used artificial surface representations: a Gaussian random surface with the same $\omega_{bi} \approx \tan(7.5°)$, a cratered surface with depth/diameter ratio of 0.1 and a combination of a Gaussian random surface and a cratered surface.

2.2 Models and Theory

2.2.1 Basic Assumptions

In all of the following derivations we assume surface slopes are distributed Gaussian. Even though the slope distribution of realistic surfaces is often non–Gaussian (See Figure 2.1b and Rosenburg et al. (2011a)), the temperature distribution of Gaussian surfaces at some scale closely follows that of the realistic lunar topography at the same scale, making them good statistical analogs for thermal models (e.g. Davidsson et al., 2015; Rubanenko and

Aharonson, 2017; Rubanenko et al., 2018). We constrain the impact of this assumption on our results in section 2.3.1.

To compute thermal emission we assume a Lambert radiator appropriate for a black body (Melvin, 1955; Howell et al., 2015); *i.e.* that the emitted radiation flux is isotropic and the radiation flux received by an observer depends on the cosine of the angle between the slope normal and the ray connecting the center of the slope to the observer (the local emission angle). From a technical point of view, this assumption greatly simplifies calculations compared to other scattering laws such as Fresnel. From a physical point of view, thermally emitted radiation from the lunar regolith is of the same order as the grain size, and granular scattering approaches geometric-optics limits when the wavelength is much smaller than the size of the particle (Van de Hulst, 1981). Consequently, in many cases assuming Lambertian scattering is as appropriate as Fresnel scattering. To demonstrate this, we compare thermal emission from an optically thick granular material to Fresnel and Lambert scattering.

In Figure 2.2 we compare the directional emissivity calculated by a simplified particle scattering model with example single scattering albedo and asymmetry parameter (see 2.5 for exact values and discussion) to Lambert and Fresnel phase functions with different refractive indices. We find Lambert is a reasonable first order approximation for scattering by particulate medium compared to Frensel given the typical range of incidence angles on a realistic rough surfaces (see Figures 2.3 and 2.4).

2.2.2 Equilibrium Temperature Distribution of Gaussian sunlit surfaces

A Gaussian stochastic process is a collection of random variables that follow the well known Gaussian probability density function (PDF),

$$f(x) = \frac{1}{\sqrt{2\pi\sigma^2}} \exp\left[-\frac{(x-\mu)^2}{2\sigma^2}\right] \tag{2.1}$$

where μ and σ are the mean and standard deviation. A *Gaussian random surface* is a 2-D Gaussian stochastic process which is both stationary and isotropic in space. For a

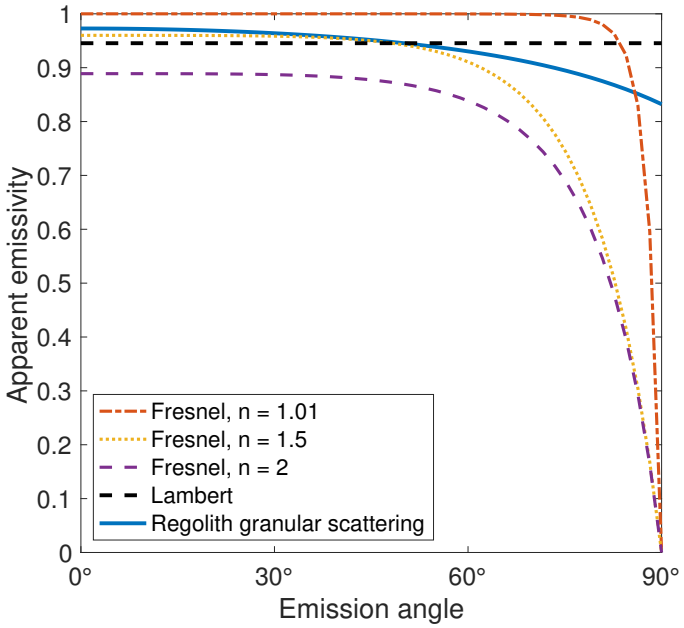

Figure 2.2: Graunlar radiative transfer model (blue line) compared to Lambert (black line) and three cases of Fresnel scattering with varying refractive indices. Lambert scattering is an appropriate first-order approximation to granular scattering compared to geometric Fresnel scattering. For the granular scattering model, we assumed a representative asymmetry parameter $g = 0.7$ and single scatter albedo $\tilde{\omega} = 0.5$ (see appendix for detailed explanation). The bolometric emissivity of the Lambert surface was chosen such that it would emit the same average amount of energy as the granular surface.

stationary and isotropic process, the covariance function depends only on the absolute value of the distance between two points and not on their individual locations. The local slope and elevation are not correlated (e.g Smith, 1967b; Bourlier et al., 2002). Consequently, an isotropic Gaussian surface is defined solely by its 1-D covariance function, making it a convenient mathematical analog of realistic topography (Schroeder, 2009).

The height of the topography h of any rough surface may be described in terms of the horizontal Cartesian coordinates x and y. A single slope on the surface is given by the local gradient $\nabla h \equiv \vec{s} = (p, q)$, where $p = \partial h/\partial x$ and $q = \partial h/\partial y$. The slope angle α, the angle between the slope and a flat reference plane, is simply $\tan\alpha = |\vec{s}| = \sqrt{p^2 + q^2}$. The slope

aspect, the angle between $\vec{s}$ and the positive direction of the Cartesian x axis ("east"), may be calculated as $\tan\theta = q/p$.

For a Gaussian surface, p, q are normally distributed with zero mean and standard deviation ω. For a zero-mean process, ω is also the unidirectional slope distribution RMS. It is important to distinguish between the *unidirectional* RMS slope across a topographic transect, ω, and the *bidirectional slope* RMS in the direction of the steepest descent, which we abbreviate ω_{bi}. The ratio between those two RMS slope values is $\omega_{bi}/\omega = \sqrt{2}$ (Shepard et al., 2001; Aharonson and Schorghofer, 2006).

The distribution of α is obtained by calculating the joint probability distribution $f_{p,q}$,

$$f_\alpha(\alpha) = \frac{\tan\alpha}{\omega^2\cos^2\alpha}\exp\left(-\frac{\tan^2\alpha}{2\omega^2}\right) \tag{2.2}$$

The distribution of θ for an isotropic surface is simply,

$$f_\theta(\theta) = \frac{1}{2\pi} \tag{2.3}$$

we show the full derivation of those distributions in appendix 2.6.1.

In order to find an analytical expression for the equilibrium temperature distribution of rough surfaces we employ the change of variables technique (see appendix 2.6.2). We first derive expressions relating the slope and aspect angles to the incidence angle, and then use them to calculate the surface irradiation and its ensuing equilibrium temperature.

We define the normalized slope normal vector using α and θ as,

$$\hat{N} = \frac{\vec{N}}{|N|} = (\sin\alpha\sin\theta, \sin\alpha\cos\theta, \cos\alpha) \tag{2.4}$$

and the solar vector between the slope center and the position of a point-Sun as,

$$\hat{S} = (\sin z\cos a, \sin z\sin a, \cos z), \tag{2.5}$$

where z is the solar zenith angle and a is the solar azimuth angle.

The cosine of the incidence angle Θ, the angle between the slope normal vector and the Sun, is given by the scalar product of Eq. 2.4 and 2.5,

$$\cos\Theta = \hat{N}\cdot\hat{S} = \cos\alpha\cos z + \sin\alpha\sin z\cos(\theta - a). \tag{2.6}$$

The solar irradiance, the energy flux received from the Sun, is given by,

$$F = \frac{S_0(1-A)}{(r/1\ \mathrm{AU})^2}\cos\Theta \equiv \beta\cos\Theta, \tag{2.7}$$

where $S_0 = 1367\ \mathrm{W\ m^{-2}}$ is the solar constant at 1 AU, A is the bolometric albedo and r is the distance from the Sun. Neglecting scattering and thermal emission, which are small compared to solar radiation (Bandfield et al., 2015), the equilibrium temperature may be derived using the Stefan-Boltzmann law of blackbody radiation,

$$F = \sigma\varepsilon T^4 \tag{2.8}$$

where $\sigma = 5.67\times10^{-8}\ \mathrm{W\,m^{-2}\,K^{-4}}$ is the Stefan-Boltzmann constant and ε is the bolometric emissivity. Throughout this paper we take $A = 0.1$ and $\varepsilon = 0.95$ as example values (Buratti et al., 1996).

2.2.2.1 Special case: the Sun at zenith ($z = 0$)

When the Sun is at zenith, $z = 0$, and Eq. 2.6 may be reduced into $\cos\Theta = \cos\alpha$. In that case, the incidence angle distribution is simply given by Eq. 2.2 with $\alpha = \Theta$. We now use change of variables to obtain the solar irradiance distribution of the surface for $z = 0$,

$$f_{F_0}(F) = f_\Theta(\Theta(F))\frac{\partial\Theta}{\partial F} = \frac{\beta^2}{\omega^2F^3}\exp\left(-\frac{1}{2\omega^2}\frac{\beta^2-F^2}{F^2}\right), \tag{2.9}$$

where F_0 indicates the probability distribution with respect to the incidence flux a zero zenith angle. Similarly the surface equilibrium temperature distribution for $z = 0$,

$$f_{T_0}(T) = f_{F_0}(F(T))\frac{\partial F}{\partial T} = \frac{4}{\omega^2\rho^2T^9}\exp\left(-\frac{1}{2\omega^2}\frac{1-\rho^2T^8}{\rho^2T^8}\right) \tag{2.10}$$

where we defined $\rho \equiv \sigma\varepsilon/\beta$.

A useful result is the mean of the direct irradiance with the Sun at zenith,

$$\bar{F_0} = \int_0^\beta F f_{F_0}(F)dF = \frac{\beta}{\sqrt{2}\omega}\Gamma\left(\frac{1}{2},\frac{1}{2\omega^2}\right)\exp\left(\frac{1}{2\omega^2}\right) \tag{2.11}$$

where $\Gamma(a,x) = \int_x^\infty t^{a-1}e^{-t}dt$ is the upper incomplete gamma function. Note that Γ can be further simplified using the complementary error function, as $\Gamma(1/2,x) = \sqrt{\pi}\,\mathrm{Erfc}(\sqrt{x})$.

Expanding Eq. 2.11 around $\omega = 0$ we find $\bar{F}_0 \approx \beta\,(1-\omega^2)$. Since the total absorbed energy is β, this expansion implies a fraction ω^2 is scattered between surface slopes. Similarly, the mean of the temperature distribution is,

$$\bar{T}_0 = \int_0^{\rho^{-1/4}} T f_{T_0}(T) dT = \frac{1}{\left(2\omega^2\rho^2\right)^{1/8}} \Gamma\left(\frac{7}{8}, \frac{1}{2\omega^2}\right) \exp\left(\frac{1}{2\omega^2}\right) \tag{2.12}$$

In Section 2.2.2.3 we compare these derivations with a numerical model and remote sensing data.

2.2.2.2 The general case ($z > 0$)

When the Sun in not in zenith, Eq. 2.6 can no longer be reduced as in section 2.2.2.1. In this case, the incidence angle distribution is,

$$f_{\cos\Theta} = \frac{1}{\pi\omega^2} \exp\left(\frac{1}{2\omega^2}\right) I_\Theta(\cos\alpha), \tag{2.13}$$

where,

$$I_\Theta(\cos\alpha) = \int_{c_+}^{c_-} \frac{1}{\cos^3\alpha} \sqrt{\frac{1}{(\cos\alpha - c_+)\,(c_- - \cos\alpha)}} \exp\left(-\frac{1}{2\omega^2\cos^2\alpha}\right) d\cos\alpha, \tag{2.14}$$

and $c_+ = \cos(\Theta + z)$ and $c_- = \cos(\Theta - z)$. Unfortunately, I_Θ does not appear to have a closed-form analytical solution. Here we provide an asymptotic approximation that is valid in a variety of cases, later comparing it with the numerical solution (see appendix 2.6.3).

The asymptotic approximation of $I(v(\Theta))$ is only valid if the product $\omega^2\cos^2(\Theta - z)$ is sufficiently small. As a result, our solution is more accurate for small ω^2 (low roughness) and $\Theta \not\approx z$ (sun-facing surface slopes). We will further explore this parameter space in section 2.2.2.3.

Using Laplace's method, we approximate the integral and derive an expression for the incidence angle distribution,

$$f_{\cos\Theta}(\Theta) \approx \frac{\omega}{\sqrt{\pi\,(1 - c_+/c_-)}} \left(1 + \frac{1}{\omega^2 c_-^2}\right) \exp\left[\frac{1}{2\omega^2}\left(1 - \frac{1}{c_-^2}\right)\right]. \tag{2.15}$$

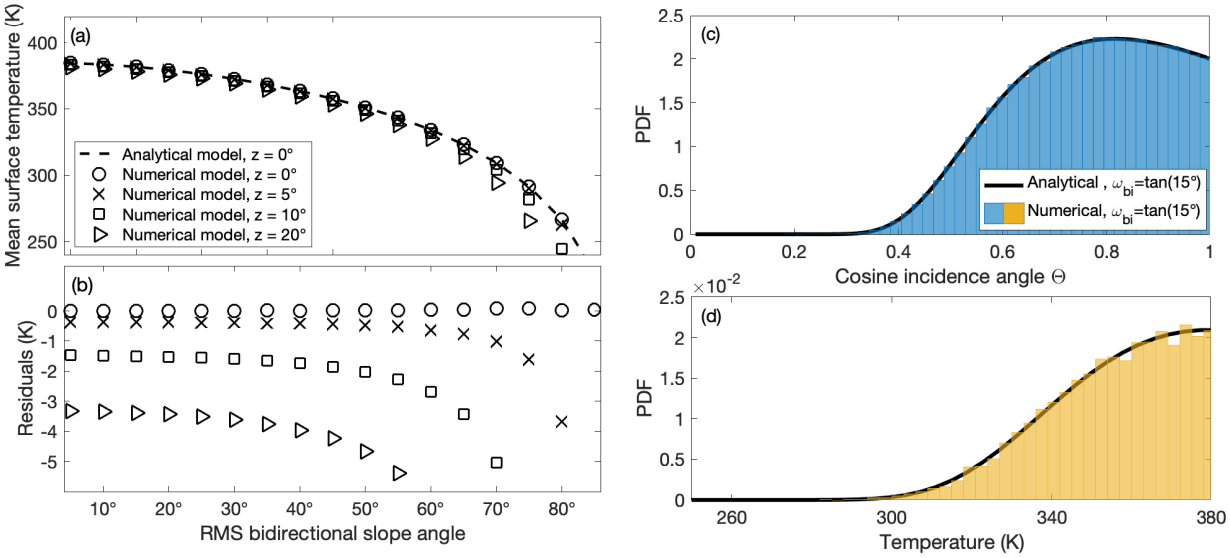

Figure 2.3: (a) The mean temperature of a Gaussian random surface calculated using our analytical model in the $z = 0$ simplification (dashed line), compared to four different runs of our numerical model with varying zenith angle to show its range of applicability. (b) The residual plot (numeric subtracted from analytic) of (a). The prediction made by our analytical model becomes less accurate for higher zenith angles as explained in the text. However, for low to moderate zenith angles and bidirectional RMS slope values, the error is contained at $< 1\%$. (c,d) The distributions of the surface incidence angles and equilibrium temperatures calculated by our analytical model (blue line) match those calculated by the numerical model (orange bars). For comparison, the temperature of a smooth horizontal surface is 384.80 K.

As before, we use change of variables to derive the irradience distribution,

$$f_F(F) \approx \frac{\omega}{\sqrt{2\pi\beta^2}} \frac{\sqrt{1+\Phi_2 \cot z}}{\Phi_1} \left(1 + \frac{1}{\omega^2 \Phi_3}\right) \exp\left[\frac{1}{2\omega^2}\left(1 - \frac{1}{\Phi_3}\right)\right], \tag{2.16}$$

and the equilibrium temperature distribution,

$$f_T(T) \approx \frac{4\omega\rho T^3}{\sqrt{2\pi}} \frac{\sqrt{1+\tau_2 \cot z}}{\tau_1} \left(1 + \frac{1}{\omega^2 \tau_3}\right) \exp\left[\frac{1}{2\omega^2}\left(1 - \frac{1}{\tau_1^2 \tau_3}\right)\right], \tag{2.17}$$

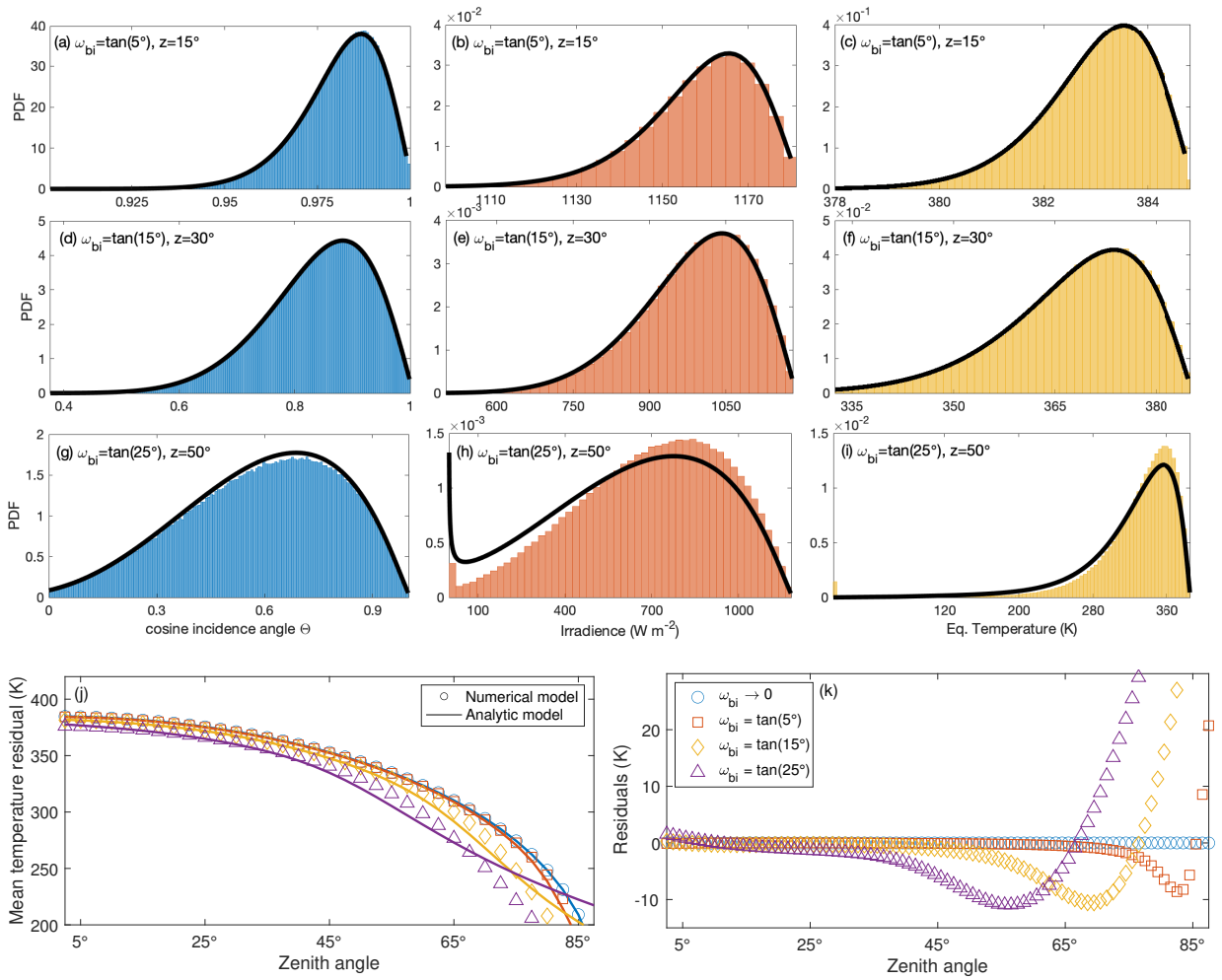

Figure 2.4: (a-i) Numerically computed incidence angle (blue bars), irradiance (orange bars) and equilibrium temperature (yellow bars) distributions compared with our analytical model (black line) for various values of RMS slope ω_{bi} and zenith angles z. As the surface roughness increases, our approximation of the integral in Eq. 2.14 becomes less accurate. Additionally, as roughness and zenith angles increase, shadows appear on the surface, further skewing our analytical results. (j) The mean surface temperature predicted by our analytical model, compared to a numerical model. (k) Residuals plot for (j), showing the two sources of error in our analytical model.

where Φ_i, τ_i are functions of the irradience F and temperature T,

$$\begin{aligned} \Phi_1 &\equiv \sqrt{1 - F^2/\beta^2} & \tau_1 &= \sqrt{1 - \rho^2 T^8} \\ \Phi_2 &= \frac{(F/\beta)\cot z}{\Phi_1} & \tau_2 &= \frac{\rho T^4 \cot z}{\tau_1} \\ \Phi_3 &= \Phi_1^2 \left(1 + \Phi_2\right)^2 \sin^2 z & \tau_3 &= \tau_1^2 \left(1 + \tau_2\right)^2 \sin^2 z. \end{aligned} \tag{2.18}$$

Since the integral $\int f_T(T)TdT$ most likely does not have an analytical solution, we do not derive a closed-form expression for the mean equilibrium temperature of Gaussian surfaces in the general case. For the same reason, the above distributions have to be numerically normalized to 1 in order for them to be used as probability density functions.

2.2.2.3 Model validation and uncertainties

We validate our analytical model in the $z = 0$ case with a numerical model that accounts for insolation and self shadowing, but not scattering which may be neglected for low solar incidence angles (Bandfield et al., 2015). In order to numerically calculate the equilibrium temperatures distribution of a Gaussian surface we generate an artificial Gaussian random field and use Eqs. 2.6 through 2.8 to calculate the incidence angle, irradiance and temperature for each slope on the field. Self shadows are accounted for by setting the irradiance of all slopes with negative cosine incidence angle to zero. In Figure 2.3(a,b) we compare the analytically derived to the numerically calculated mean temperature. As expected, our analytic model becomes inaccurate for $z > 0$ as the surface roughness grows and the contribution of the slope aspect to the incidence angle can no longer be neglected (Eq. 2.6). For zero zenith angle the surface is completely illuminated, so shadows do not contribute to the error in Figure 2.3.

In the general case we no longer assume the solar zenith angle is zero. This generalization carries two major sources of error, one rooted in using Laplace's asymptotic approximation to solve the integral in Eq. 2.14 and the other is related to shadowing.

Laplace's method is more accurate when the coefficient in the exponential function (x in Eq. 2.40) is very large. In our model, this condition holds if both the surface roughness is small and $\Theta \not\approx z$. Figure 2.4 (panels a-f) show our analytical model agrees well with the numerical model for small roughness and small zenith angles. However, as the surface roughness increases the analytical model becomes less accurate relative to the numerical model, as demonstrated in panels (g-i). For sufficiently high surface roughness and solar

zenith angles, self shadowing affects our predictions as well.

To quantify this error, we compare the mean surface temperature predicted by the analytical and the numerical models in Figure 2.4 (panels j,k). The residuals plot shown in panel (k) demonstrates the two errors discussed above. For a Gaussian surface with $\omega_{bi} = \tan(25°)$, the mean incidence angle roughly equals the solar zenith angle, $z \sim 55°$. For a surface with $\omega_{bi} = \tan(15°)$ this happens at $z \sim 67°$ (see arrows in panel k). At even higher angles, the no-shadows assumption in our analytical model causes it to be warmer compared to the numerical model that includes self-shadowing. Overall, the errors in our approximate analytical model are contained below 10% for $\omega_{bi} < 25°$ and $z < 75°$.

2.2.3 Thermal emission from rough surfaces illuminated from zenith

Due to sub-resolution topographic roughness, a surface has a distribution of temperatures that is averaged over the footprint of the observing instrument (Shepard, 2017). About a century ago, observers noticed the emitted thermal radiation decreases along the full Moon disk more slowly than the cosine of the emission angle expected from a smooth Lambertian surface (e.g. Pettit and Nicholson, 1930; Sinton, 1962; Saari et al., 1972). This deviation was attributed to topographic relief at the subpixel scale obscuring other thermally emitting surface slopes from the detector.

A few studies have since modeled these effects by numerically integrating the observed brightness, assuming the surface is composed of normally distributed slopes (Smith, 1967b), or hemispherical craters (Buhl et al., 1968). In these models, each surface element is assumed to be a perfect Lambertian emitter of infrared radiation, neglecting lateral heat flow and scattering which are less important during the day (Bandfield et al., 2015; Rubanenko and Aharonson, 2017). Other notable works, such as the comprehensive formalism derived by Hapke (1981), incorporated empirical work with physical scattering laws to provide an approximated closed form description of surface roughness. More recently, Bandfield et al. (2015); Davidsson et al. (2015); Delbo et al. (2015) and others employed computationally

expensive numerical models to measure the thermophysical properties of the Moon and other airless planetary bodies. Here we provide a closed-form expression for the average radiation emitted from a rough surface illuminated from zenith as a function of the emission angle.

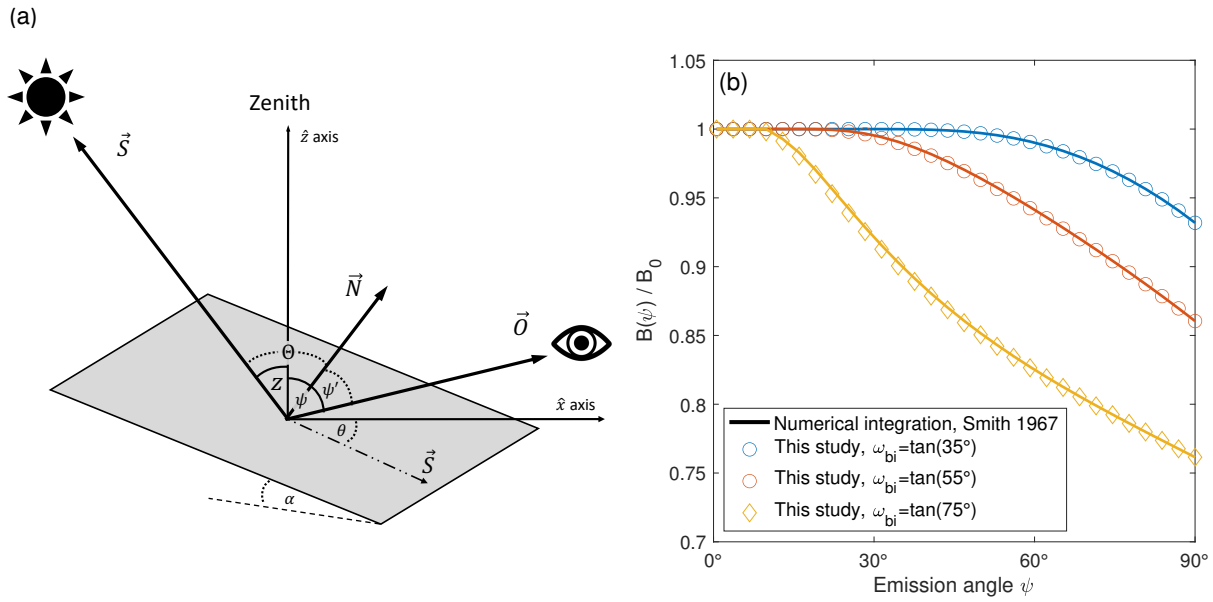

Figure 2.5: (a) The angles involved in calculating the mean brightness. ψ is the emission angle, ψ' is the angle between the slope normal vector and the observer, z is the solar zenith angle and Θ is the angle between the slope normal and the Sun (solar incidence angle). As ψ decreases, more slopes on the surface are obscured from the observer. A surface illuminated form zenith becomes more isothermal as ω decreases. (b) Our closed-form approximation (markers) is in excellent agreement with the complete numerical solution (line) to the integral appearing in Smith (1967b) for all values of ω_{bi}.

The infrared brightness of a flat surface is related to the surface temperature as $B = \epsilon\sigma T^4/\pi$ (Buhl et al., 1968). The observed mean brightness $\bar{B}(\psi)$ may be calculated by averaging the total energy reaching the observer from all surface slopes, normalized and divided by the projected area,

$$\bar{B}(\psi) = \frac{\int B\cos\psi' dA}{\int \cos\psi' dA} \tag{2.19}$$

where ψ' is the angle between the slope normal vector and the observer (see Figure 2.5) and the integration is performed only over the part of the surface seen by the observer. As the

global emission angle relative to the mean plane ψ increases, a growing number of slopes is obscured from the observer by the topographic relief, reducing $\bar{B}(\psi)$. For an isothermal surface, B is constant regardless of the shape of the surface, and the brightness is constant as expected from a Lambertian surface. This highlights that directional emissivity can be caused by the anisothermality of rough Lambertian surfaces.

For a Gaussian surface illuminated from zenith, we may rewrite Eq. 2.19 as,

$$\bar{B}(\psi) = \frac{\bar{B}(0)}{I} \int_{-\infty}^{\infty} \int_{-\infty}^{\infty} \frac{1 - q \tan \psi}{\sqrt{1 + p^2 + q^2}} \exp\left(-\frac{p^2 + q^2}{2\omega^2}\right) S(q, \psi) dp dq \tag{2.20}$$

where I is the normalization factor,

$$I = \int_{-\infty}^{\infty} \int_{-\infty}^{\infty} \frac{1}{\sqrt{1 + p^2 + q^2}} \exp\left(-\frac{p^2 + q^2}{2\omega^2}\right) dp dq \tag{2.21}$$

and $S(q, \psi)$ is the shadowing function after Smith (1967b),

$$S(q, \psi) = \frac{H(\cot \psi - q)}{1 + \Lambda(\cot \psi)} \tag{2.22}$$

where H is the Heaviside step function and,

$$\Lambda(\cot \psi) = \frac{1}{2} \left[\sqrt{\frac{2}{\pi}} \frac{\omega}{\cot \psi} \exp\left(-\frac{\cot^2 \psi}{2\omega^2}\right) - \operatorname{erfc}\left(\frac{\cot \psi}{\sqrt{2\omega^2}}\right) \right]. \tag{2.23}$$

The integral in Eq. 2.20 may be readily reduced to,

$$I_B = \int_{-\infty}^{\cot \psi} (1 - q \tan \psi) K_0\left(\frac{1 + q^2}{4\omega^2}\right) \exp\left(\frac{1 - q^2}{4\omega^2}\right) dq \tag{2.24}$$

where $K_\nu(x)$ is the ν'th order Modified Bessel Function of the Second Kind. To solve this integral, we first separate it into two parts,

$$\begin{aligned} I_{B_1} &= \tan \psi \int_{-\infty}^{\cot \psi} q K_0\left(\frac{1 + q^2}{4\omega^2}\right) \exp\left(\frac{1 - q^2}{4\omega^2}\right) dq \\ &= \frac{\tan \psi + \cot \psi}{2} \exp\left(\frac{1 - \cot^2 \psi}{4\omega^2}\right) \left[K_0\left(\frac{1 + \cot^2 \psi}{4\omega^2}\right) - K_1\left(\frac{1 + \cot^2 \psi}{4\omega^2}\right) \right] \end{aligned} \tag{2.25}$$

and

$$I_{B_2} = \int_{-\infty}^{\cot \psi} K_0\left(\frac{1 + q^2}{4\omega^2}\right) \exp\left(\frac{1 - q^2}{4\omega^2}\right) dq \tag{2.26}$$

I_{B_2} most likely has no closed-form solution. However, upon carefully inspecting the derivative of Eq. 2.24 with respect to ψ, we notice that I_{B_1} holds information about the shape of $\bar{B}(\psi)$ while I_{B_2} controls its scale and offset along the vertical axis. As a result, we may obtain an accurate approximate solution to $\bar{B}(\psi)$ by rescaling the solution to the integral I_{B_1}. We first rewrite Eq. 2.20 as,

$$\bar{B}\left(\psi\right) = \left[\frac{\bar{B}(0) - \bar{B}\left(\frac{\pi}{2}\right)}{\tilde{B}\left(0\right) - \tilde{B}\left(\frac{\pi}{2}\right)}\right]\left(\tilde{B}\left(\psi\right) - \tilde{B}(0)\right) + \bar{B}(0) \tag{2.27}$$

where we defined,

$$\tilde{B}(\psi) = \frac{\bar{B}(0)}{2\pi I\omega^2}\frac{I_{B_1}}{1+\Lambda(\cot\psi)}. \tag{2.28}$$

and where,

$$\tilde{B}(0) = 0 \tag{2.29}$$

$$\bar{B}\left(\frac{\pi}{2}\right) = \tilde{B}\left(\frac{\pi}{2}\right) = \sqrt{\frac{2\pi}{\omega^2}}\frac{\bar{B}(0)}{4\pi I\omega^2}\exp\left(\frac{1}{4\omega^2}\right)\left[K_1\left(\frac{1}{4\omega^2}\right) - K_0\left(\frac{1}{4\omega^2}\right)\right] \tag{2.30}$$

Overall, we obtain a closed form expression for the thermal radiation emitted by a rough surface illuminated from zenith as a function of the emission angle ψ,

$$\bar{B}\left(\psi\right) = \bar{B}(0) - \frac{\bar{B}(0) - \bar{B}\left(\frac{\pi}{2}\right)}{\bar{B}\left(\frac{\pi}{2}\right)}\tilde{B}\left(\psi\right) \tag{2.31}$$

To validate our analytical thermal emission model, we compare it with the numerical solution of the integral in Eq. 2.20 (Figure 2.5b). We find that scaling I_{B_1} provides an excellent approximation to the mean observed brightness $B(\psi)$. We also note that for $\omega \to 0$, $\bar{B}(\psi)$ becomes constant as expected from a flat (isothermal) Lambert surface.

2.3 Results: applications for the Moon

2.3.1 The Temperature Distribution of Realistic Sunlit Surfaces

A major assumption in our analytical model is that the surface slopes have a Gaussian distribution. However, the slope distribution of the Moon is different from that of a Gaussian rough surface (see Figure 2.1b above). To asses how this assumption affects the temperature

distribution, we again compare our analytical model to a numerical simulation, this time employing realistic topography.

We choose two locations on the Moon whose topographic relief was measured using stereoscopy of Narrow Angle Camera (NAC) image pairs obtained by the Lunar Reconnaissance Orbiter Camera (LROC, Robinson et al. (2010); Henriksen et al. (2017)). To avoid thermal effects caused by large-scale slopes, we selected areas that are not dominated by large scale topographic features. The first region we consider (Figure 2.6a) is the famous Mandel'shtam scarp, located on the floor of the ~ 200 km Mandel'shtam crater in the highlands region of the Moon ($6°\mathrm{N}, 162°\mathrm{E}$). The second site (Figure 2.6b) is located in the maria region, near the Luna 16 landing site ($-0.5°\mathrm{N}, 56°\mathrm{E}$). The bi-directional RMS slope of the highlands site is $\omega_{bi} \approx \tan(9.63°)$ (5 m baseline), and the bi-directional RMS slope of the maria site is, as expected, slightly lower, $\omega_{bi} \approx \tan(4.63°)$ (2 m). The digital terrain models (DTM), constructed using images M191909925 L/R and M191895630 L/R (for Mandel'shtam scarp) and M159582808 L/R and M159589596 L/R (for the Luna 16 landing site), may be downloaded from the planetary data system (PDS).

For each region, we calculate the bidirectional RMS slope ω_{bi} and derive equilibrium temperatures using the numerical model. Then, we feed the calculated ω_{bi} of each surface to our analytical model and derive the temperature distribution for various solar zenith angles. Results are shown in Figure 2.7. We find that although the slope distributions (panels c,e) are significantly different from those of a Gaussian surface, the temperature distributions and their mean predicted by the analytical model are similar to those derived using the numerical model. Consequently, the Gaussian approximation appears to be sufficient when describing the temperatures of realistic rough surfaces.

2.3.2 Thermal Emission from Rough Surfaces

The lateral scale of the roughness affecting the thermal phase function has been a question of much debate. Smith (1967b) suggested the observations conducted by Saari et al. (1966) are

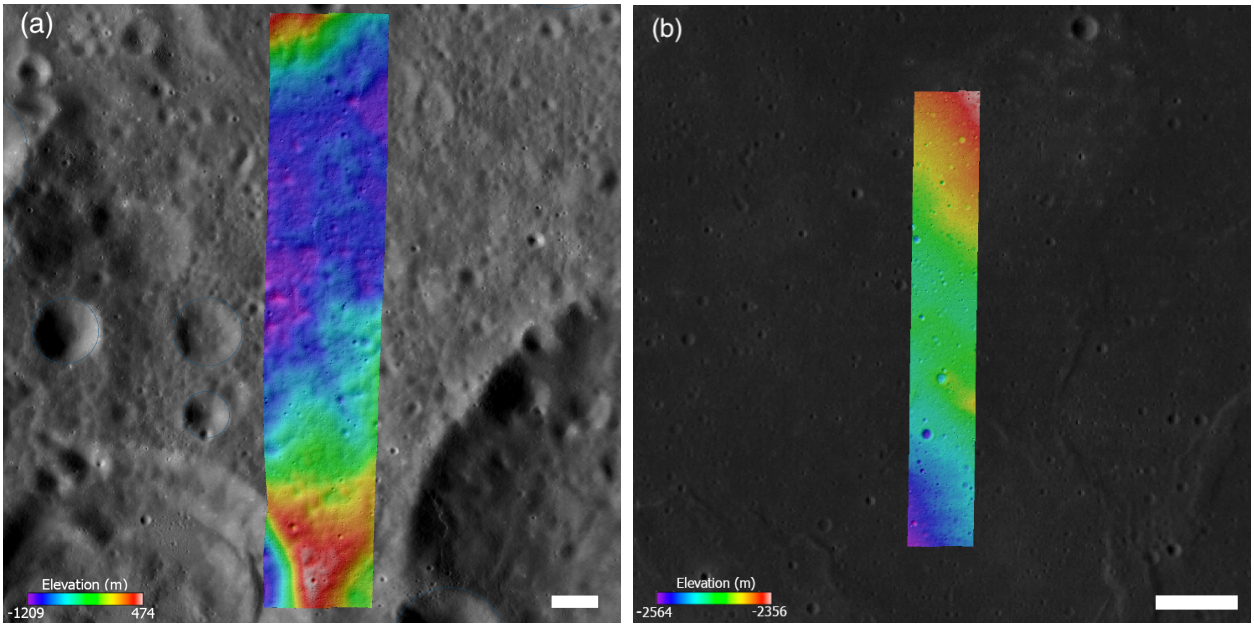

Figure 2.6: We compare our Gaussian surface temperature model with the modeled temperature distribution of two realistic lunar sites. (a) Highlands region near Mandel'shtam crater ($6°\mathrm{N}, 162°\mathrm{E}$). (b) Maria region near the Luna 16 landing site ($-0.5°\mathrm{N}, 56°\mathrm{E}$). The colored strips shows the stereographically derived DTMs we used and whose resolutions are (a) 5 m/pixel (b) 2 m/pixel. White scale bar indicates 5 km.

mostly affected by large scale topographic features. By incorporating subsurface conduction in their rough surface model, Spencer (1990), Rozitis and Green (2011) and others noted that the thermal phase function is probably affected by roughness at the thermal isolation scale - which to first order is comparable to the diurnal skin depth. More recently, Bandfield et al. (2015) employed a 2-D thermal conduction model to more accurately constrain the length scale of thermally isolated features on the Moon to $\sim 0.5 - 5$ mm.

The RMS slope appearing in our analytical emission model (Eq. 2.31) should thus be treated as the roughness at the scale affecting the thermal phase function. As the scale of this roughness is much smaller than the resolution of the instrument, it is appropriate to treat it as thermal equivalent of an optical property of the surface, separate from the roughness of thermally resolved features (as shown, *e.g.*, in Figure 2.7). To describe this property we

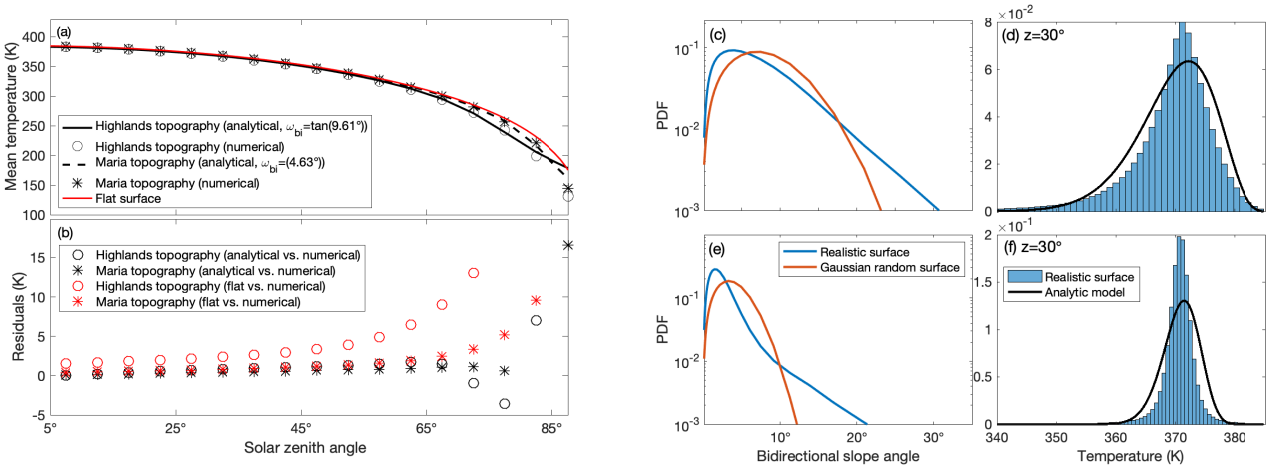

Figure 2.7: (a) Mean surface temperatures and (b) residuals for the two realistic lunar topographies we consider. (c) The slope distribution of the highlands region compared to the slope distribution of a Gaussian random surface. (d) The temperature distribution of the highlands region (blue bars) compared to the temperature distribution of our analytical model (black line). (e,f) same for maria region. For moderately rough surfaces, our model is more accurate in predicting surface temperatures compared to a model that assumes no roughness at all (red).

introduce the roughness parameter, R, that represents the bidirectional RMS slope at *the scale that affects the measured phase function*. For different detectors, R would represent different lateral scales. Next we use our model to derive R for the lunar surface.

One advantage of our closed-form expression over numerical simulations is that it may be used as a model function for non-linear fitting. We demonstrate this in Figure 2.8, where we use nonlinear least-squares regression to fit R to two sets of thermal emission measurements. Panel (a) shows telescopic observations of thermal emissions from the lunar surface (Sinton, 1962). Fitting Eq. 2.31 to the data we obtain $R \approx \tan\left(67.22^\circ \pm 33.45^\circ\right)$, where the error indicates 95% confidence intervals. The high relative error is heavily influenced by measurements at high emission angles. For the data in panel (b) we find $R \approx \tan\left(49.70^\circ \pm 6.62^\circ\right)$, in agreement with the RMS slope at the $0.1 - 10$ mm lateral scale measured using DTMs (Helfenstein and Shepard, 1999) and thermally (Smith, 1967b; Rozitis and Green, 2011;

Bandfield et al., 2015) (Figure 2.1). The good agreement between our measurements and those obtained using the DTM bolsters the conclusion of Bandfield et al. (2015) who determined Diviner measurements are sensitive by the roughness at the thermal isolation scales.

We apply our results to estimate the Moon's roughness using measurements obtained by Diviner during the off-nadir campaign. We group high emission ($\psi \approx 50°$) and low emission ($\psi < 10°$) channels 3 and 4 brightness temperatures ($8.20 \pm 0.22\ \mu m$) in $0.5° \times 0.5°$ and $1° \times 1°$ bins, discarding measurements for which the solar zenith angle was greater than 15°. We elected to use these channels as they closely resemble the bolometric temperatures in the equatorial region of the Moon. Due to the emissivity difference between the Mare and Highlands regions, we used the channel that produced higher average temperatures in low emission angle. Due to the limited duration of the off-nadir campaign, not all the locations in our surveyed area were sampled at the same zenith angle for both high and low emission angles. To suppress that artifact, we correct the measured brightness temperatures by first converting them to energy flux, assuming they are blackbody emitters, and then dividing them by the cosine of the zenith angle in which the measurement was acquired. For each bin, we calculate the thermal phase function and use our model to invert for R. Finally, we remove missing values by interpolating cross-track measurements with a moving median filter with window size of 5 pixels.

In Figure 2.8 we map R in part of the equatorial region sampled by Diviner during the off-nadir campaign, indicating in Table 2.1 the mean value for a few selected features. As expected, R is generally lower in the maria (longitudes $\sim 60° - 100°$) and higher in the highlands (longitudes $\sim 100° - 160°$). The good agreement between our measured R and the RMS slope angle measured by Helfenstein and Shepard (1999) at the $0.1 - 1$ mm lateral scale confirms Bandfield et al. (2015)'s conclusions about the lunar thermal isolation scale ($R \sim 30 - 40°$). In the maria, small craters are rougher than their surroundings, potentially due to the presence of small rocks increasing the surface roughness at the thermal isolation lateral scale. The floors of basins such as Mare Smythii ($\sim -1°\mathrm{N}, 85°\mathrm{E}$) and Mendeleev Crater ($\sim 5°\mathrm{N}, 141°\mathrm{E}$) are slightly smoother than their immediate surroundings, but are not

distinctly different from similar geologic regions. We note the low resolution of the map in Figure 2.8 is a consequence of the limited duration of the Diviner off-nadir campaign, and expect to improve it in the future by conducting additional observations.

R	Maria	Highlands	Floor of Mare Smythii	Floor of Mendeleev Crater
Mean	30.2°	36.8°	31.9°	35.0°
Standard deviation	5.9°	4.4°	1.6°	4.3°

Table 2.1: Representative values for R in the Maria, highlands and the Floors of Mare Smythii and Mendeleev Crater. Regions were manually masked based on LROC imagery data.

2.4 Discussion

Insolation dominates the radiation balance on airless planetary bodies. Surface roughness affects the temperature distribution by scattering incoming radiation and decreasing the downward component of the energy flux vector. Above we derived exact closed-form expressions for the incidence angle, flux and equilibrium temperature distribution of rough Gaussian surfaces illuminated from zenith (section 2.2.2.1), and approximate closed-form expressions in the general case (section 2.2.2.2). Expanding our solution for small ω, we find a fraction $1-\omega^2$ of the absorbed energy is scattered between surface slopes. Additionally, we find that although the slope distributions of realistic airless surfaces are often non-Gaussian, their equilibrium temperature distribution closely follows that of a Gaussian surface with the same RMS slope ω.

In addition to changing the temperature distribution, topographic roughness affects the bolometric temperature at emission (observation) angles greater than zero. To account for this effect, we derive a closed-form expression for the directional emissivity of a rough surface illuminated from zenith at any emission angle (section 2.2.3). Previous studies found that due to the higher roughness at smaller scales, this thermal phase function effect is most likely

sensitive to roughness at the thermal isolation scale, which on the Moon is $\sim 0.5-5$ mm (Bandfield et al., 2015). In order to distinguish the roughness at the thermal isolation scale from roughness of resolved topographic features, we introduce R, the roughness parameter, which corresponds to the bidirectional RMS slope at the thermal isolation scale.

We employ our model to measure R in two cases: telescopic observations and Diviner measurements. While in both cases we find the model agrees well with the observations, a potential deviation occurring at emission angles greater than 70° may imply non-Lambertian scattering on scales smaller than the thermal isolation scale (Bandfield et al., 2015). To measure R for the lunar surface, we fit our model to the thermal phase function measured by Diviner during its off-nadir campaign. We find our estimates for the roughness of the lunar Maria ($R \approx \tan(30.17°)$) and Highlands ($R \approx \tan(36.77°)$) agree well with previous measurements at the $0.1-1$ mm lateral scale, (Helfenstein and Shepard, 1999). This bolsters Bandfield et al. (2015) findings that Diviner is sensitive to roughness features at this sub-centimeter lateral scale. In the future, we intend to increase the resolution of the map we show in Figure 2.8 by conducting more off-nadir observations using Diviner.

Due to the closed form of our model it may be readily applied to any airless body as long as its rotation rate and thermal inertia are sufficiently small so that its surface is close to thermal equilibrium. For example, slowly rotating asteroids may be observed from different phase angles with the Sun in zenith to estimate their surface roughness at the thermal isolation scale which may hint at their composition, and will also allow to better constrain the thermal and dynamical parameters of other asteroids whose surfaces are not in thermal equilibrium.

2.5 Appendix A: Simplified Granular Scattering Model

Scattering by granular media consisting of spherical particles is given by Mie theory. To compute it here we adapt a 1-D two-stream radiative transfer model originally designed for thermal scattering and emission from optically-thick layer of snow grains based on the

delta-Eddington approximation (Wiscombe and Warren, 1980). The direct-beam albedo of the grains as a function of the emission angle e is given by,

$$a(e) = \frac{\tilde{\omega}^*}{1+P}\frac{1-b^*\xi\cos e}{1+\xi\cos e} \tag{2.32}$$

with,

$$\begin{aligned}
\tilde{\omega}^* &= \frac{(1-g^2)\tilde{\omega}}{1-g^2\tilde{\omega}} \\
b^* &= \frac{g^*}{1-\tilde{\omega}^* g^*} \\
\xi &= \sqrt{3(1-\tilde{\omega}^* g^*)(1-\tilde{\omega}^*)} \\
P &= \frac{2\xi}{3(1-\tilde{\omega}^* g^*)} \\
g^* &= \frac{g}{1+g}.
\end{aligned} \tag{2.33}$$

where $\tilde{\omega}$ is the single-scatter albedo and $-1 < g < 1$ is the asymmetry parameter of the single-scatter phase function, defined as the mean cosine of the scattering angle. $g = \pm 1$ corresponds to forward-directed or backward-directed scattering and $g = 0$ to isotropic scattering. Here we choose to adopt representative $\tilde{\omega} = 0.5$ and $g = 0.7$, appropriate for Diviner wavelengths and typical lunar regolith grain sizes (Mishchenko, 1994; Wiscombe and Warren, 1980). Finally, albedo is converted to directional emissivity using Kirchhoff's well-known law of thermal radiation. This result is also stemmed from Helmholtz Reciprocity principle that allows to mathematically treat a scattering medium as a thermal emitter.

Geometric scattering is given by the Fresnel equations, which describe directional emissivity by the parallel (s) and the perpendicular (p) components of an electromagnetic wave relative to the plane of incidence. For a perfect dielectric material Fresnel equations only depend on the real part of the refractive index, n,

$$r_s = \left(\frac{n^2\cos e - \sqrt{n^2-\sin^2 e}}{n^2\cos e + \sqrt{n^2-\sin^2 e}}\right)^2 ;\; r_p = \left(\frac{\cos e - \sqrt{n^2-\sin^2 e}}{\cos e + \sqrt{n^2-\sin^2 e}}\right)^2 \tag{2.34}$$

we average r_s and r_p to obtain the total Fresnel scattering shown in figure 2.2.

2.6 Appendix B: Some derivations

2.6.1 Deriving the slope and aspect distributions

Assuming independence, the joint probability distribution of the normally distributed surface slopes p, q is,

$$f(p,q) = \frac{1}{2\pi\omega^2} \exp\left(-\frac{p^2+q^2}{2\omega^2}\right) dpdq \tag{2.35}$$

For the slope magnitude $s = \sqrt{p^2+q^2}$ and aspect $\tan\theta = q/p$ the determinant of the Jacobian is trivially s. We use change of variables to find s is Rayleigh distributed with parameter ω,

$$f(s,\theta) = \frac{s}{\omega^2} \exp\left(-\frac{s^2}{2\omega^2}\right) \tag{2.36}$$

similarly, we use change of variables to find the distribution of the slope angle $\tan\alpha = s$. Since s and θ are independent, it immediately follows that θ is uniformly distributed between 0 and 2π.

2.6.2 The change of variable technique

In order to find the probability distribution of the solar incidence angle given the distributions of the slope angle and slope aspect we use the well-known change of variables technique (DeGroot and Schervish, 2012).

Let X be a continuous random variable with PDF $f_X(x)$, defined on $[c_1, c_2]$. Let $Y = u(X)$ be an invertible function of X with $X = v(Y)$. The probability density function of Y is,

$$f_Y(y) = f_X(x) \cdot |v'(y)| \tag{2.37}$$

Let X_1, X_2 be two continuous random variables with joint PDF $f_{X_1,X_2}(x_1,x_2)$. Let $Y_1 = u_1(X_1,X_2)$ and $Y_2 = u_2(X_1,X_2)$ be two invertible functions of X_1, X_2 with $X_1 = v_1(Y_1,Y_2)$ and $X_2 = v_2(Y_1,Y_2)$. The joint PDF of Y_1 and Y_2 is,

$$f_{Y_1,Y_2}(y_1,y_2) = |J| f(v_1,v_2) \tag{2.38}$$

where J is the Jacobian of the transformation, and $|J|$ the absolute value of its determinant.

2.6.3 Using Laplace's method to find the asymptotic approximate of the incidence angle distribution

We obtain an approximate solution to the integral I_Θ appearing in Eq. 2.14 using Laplace's method (Bender and Orszag, 2013). This method, also known as the method of steepest descent, is a technique for obtaining the asymptotic behavior of integrals of the form,

$$I(x) = \int_{t_0}^{t_1} f(t) \exp\left(x\phi(t)\right) dt. \tag{2.39}$$

Laplace's method states that if $\phi(t)$ has a nonzero maximum at $t = m$ on the interval $t_0 \leq t \leq t_1$, then only the immediate neighborhood of this maximum contributes to the asymptotic expansion of $I(x)$ for large x. If these conditions are met, $I(x)$ may be approximated as,

$$I(x) \sim \sqrt{\frac{2\pi}{-x\phi''(m)}} f(m) \exp\left(x\phi(m)\right) \quad \text{as} \quad x \to \infty. \tag{2.40}$$

In order to use Laplace's method, we must manipulate I such that $f(t = m)$ does not diverge. To do so, we first use Leibniz's rule for differentiation under the integral sign (commonly known as "Richard Feynman's integration trick") and substitute $\cos\alpha = b/(1 - c\sin^2 v)$ to obtain,

$$I_\Theta(v(\Theta)) = \int_{-\pi/2}^{\pi/2} \exp\left(-\frac{(1 - c\sin^2 v)^2}{2\omega^2 c_-^2}\right) dv. \tag{2.41}$$

where $c = 1 - c_+/c_-$.

Acknowledgments

In memory of Joshua Bandfield, whose pioneering scientific work inspired this study. The DTMs used to prepare Figure 2.6 may be downloaded from the LROC NAC website at `http://wms.lroc.asu.edu/lroc/view_rdr/SHAPEFILE_NAC_DTMS`. The Diviner data used to prepare Figure 2.8 may be downloaded from `10.6084/m9.figshare.11530647`.

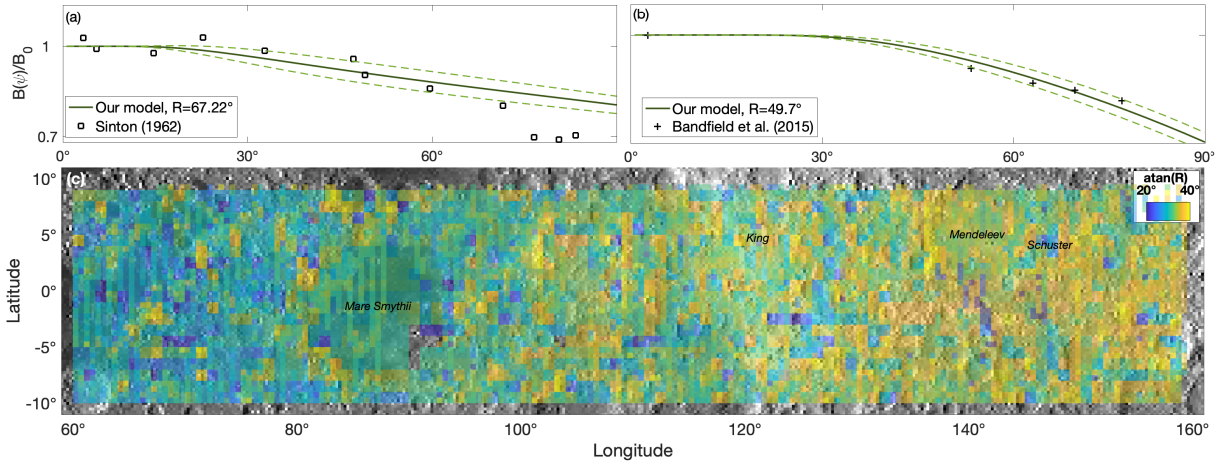

Figure 2.8: The surface RMS slope at the thermal isolation scale, which we term R. Unlike large scale topographic roughness, R more closely resembles an optical property of the surface, affecting its thermal phase function and directional emissivity. We use nonlinear regression with Eq. 2.31 as the model function, and invert relative brightness measurements conducted on the Moon (a,b) to find R. Dashed lines indicate 95% confidence intervals. (c) Same for Diviner data obtained at different emission angles. As expected, R in the maria region is generally lower than in the highlands region. Notably, the floor of Mare Smythii ($\sim -1°\text{N}, 85°\text{E}$) and Mendeleev Crater ($\sim 5°\text{N}, 141°\text{E}$) are smoother than their immediate surroundings. To improve the relatively coarse resolution of the map, which is a consequence of the limited duration of the Diviner off-nadir campaign, we overlaid a $0.5° \times 0.5°$ map (lower transparency) over a $1° \times 1°$ map (higher transparency).

CHAPTER 3

Stability of Ice on the Moon with Rough Topography

This chapter was originally published in: Rubanenko L, Aharonson O., Stability of ice on the Moon with rough topography. *Icarus*. 2017 Nov 1;296:99-109.

Abstract

The heat flux incident upon the surface of an airless planetary body is dominated by solar radiation during the day, and by thermal emission from topography at night. Motivated by the close relationship between this heat flux, the surface temperatures, and the stability of volatiles, we consider the effect of the slope distribution on the temperature distribution and hence prevalence of cold-traps, where volatiles may accumulate over geologic time. We develop a thermophysical model accounting for insolation, reflected and emitted radiation, and subsurface conduction, and use it to examine several idealized representations of rough topography. We show how subsurface conduction alters the temperature distribution of bowl-shaped craters compared to predictions given by past analytic models. We model the dependence of cold-traps on crater geometry and quantify the effect that while deeper depressions cast more persistent shadows, they are often too warm to trap water ice due to the smaller sky fraction and increased reflected and reemitted radiation from the walls. In order to calculate the temperature distribution outside craters, we consider rough random surfaces with a Gaussian slope distribution. Using their derived temperatures and additional volatile stability models, we estimate the potential area fraction of stable water ice on Earth's Moon. For example, surfaces with slope RMS $\sim 15^\circ$ (corresponding to length-scales ~ 10 m on the lunar surface) located near the poles are found to have a $\sim 10\%$ exposed cold-trap area

fraction. In the subsurface, the diffusion barrier created by the overlaying regolith increases this area fraction to $\sim 40\%$. Additionally, some buried water ice is shown to remain stable even beneath temporarily illuminated slopes, making it more readily accessible to future lunar excavation missions. Finally, due to the exponential dependence of stability of ice on temperature, we are able to constrain the maximum thickness of the unstable layer to a few decimeters.

3.1 Introduction

The small obliquity of airless planetary bodies such as the Moon and Mercury causes topographic depressions located near their poles to be in permanent or near-permanent shadow for geologic time periods. Previous works (*e.g.* Watson et al. (1961)) have shown that the lifetime of volatile deposits residing within those cold-traps is comparable to the lifetime of bodies in the Solar System.

The cold-trap distribution is tightly linked to the temperature distribution on and below the surface, which itself is governed by the shape of the topography controlling the abundance of shadows and the amount of radiation reaching them. To a lesser extent, it is also a function of the thermal properties controlling conduction into the subsurface. The latter can be modeled by solving the 1D heat diffusion equation (Schorghofer and Aharonson, 2005; Aharonson and Schorghofer, 2006). The former has been modeled assuming the topography consists of spherical craters (Buhl et al., 1968; Ingersoll et al., 1992; Hayne and Aharonson, 2015) or of normally distributed slopes (Smith, 1967b; Bandfield et al., 2015) to which an analytic solution exists. In the past two decades more general models have been developed utilizing algorithms such as ray casting and ray tracing (Paige et al., 1992; Vasavada et al., 1999; Davidsson and Rickman, 2014), combined with subsurface heat conduction. Using those models, cold-traps were shown to exist near the poles of the Moon and Mercury. Later, temperatures characteristic of cold-traps (Paige et al., 2010b) and direct evidence for frozen volatiles deposits were discovered (Colaprete et al., 2010) on the Moon as well as

remotely sensed on Mercury in RADAR (Harmon et al., 2001), laser altimetry (Neumann et al., 2013; Paige et al., 2013) and visible imagery (Chabot et al., 2014).

3.2 Models

3.2.1 Roughness Models

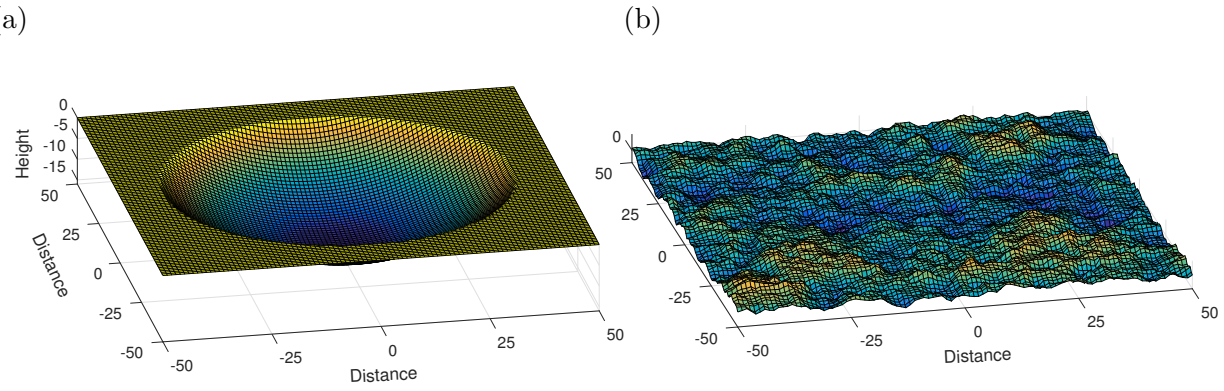

Figure 3.1: Two examples for the topographies we used in modeling the temperature distribution, visualized in natural units. (a) A spherical crater with depth to diameter $\Delta = 0.2$. (b) A rough random Gaussian surface with a slope RMS $\sigma_s = 15°$.

Here we develop and employ a thermophysical model that accounts for insolation, scattering, thermal emission and subsurface conduction, in order to investigate the link between roughness, temperature and cold-trap stability on and below the lunar surface. We first calculate the temperature distribution of two commonly used, idealized representations of rough topography: a hemispherical (bowl-shaped) crater and a rough random surface with a Gaussian slope distribution. Subsequently, we apply our findings to discuss the stability of surface and subsurface water ice.

3.2.1.1 Spherical Craters

A spherical crater is defined as a cavity shaped as a potion of a sphere of radius r, surrounded by a flat plane. The size of the crater is defined by its radius R, its depth h, or by its depth to diameter ratio, $\Delta = h/2R$. Simple craters with diameters < 15 km on the Moon are well approximated by spherical cavities with $\Delta \sim 1/5$ to $\Delta \sim 1/16$ (Pike, 1977; Stopar et al., 2012).

The height of the topography z is given in terms of the horizontal coordinates x and y. The equation describing the topography is $z = r - h \pm \sqrt{r^2 - x^2 - y^2}$. An example for a spherical crater with $\Delta = 1/5$ can be seen in Figure 3.1a.

3.2.1.2 Rough Random Surfaces with a Gaussian Slope Distribution

A common way to quantify rough terrain on airless bodies outside simple craters is to assume it is random with a Gaussian height and slope distributions (*e.g.* Hagfors (1964); Smith (1967b); Jamsa et al. (1993); Davidsson and Rickman (2014); Davidsson et al. (2015); Bandfield et al. (2015)), and describe it via the RMS slope magnitude at a given scale, σ_s. The dependence of the roughness on the 1D lateral scale may be described by a power-law spectrum with an exponent which was measured for the lunar polar regions to be ~ 2.9 (Rosenburg et al., 2011b; Schroeder, 2012). In our model, σ_s is computed at the facet scale. Different values of σ_s may be regarded as corresponding to different scales on the Moon (Rosenburg et al., 2011b). Therefore, in our discussion of ice stability we specify in addition to the RMS slope, the scale that corresponds to this value according to measurements of the lunar surface. These random surfaces could be used to explore topographies in scales lower than the instrument resolution (e.g., Rubanenko et al., 2017a).

In order to construct the model surface, we seed a matrix with a 2D Gaussian random field with a unity standard deviation and zero mean. This field has white spectrum. We compute the 2D discrete Fourier transform of the matrix and multiply its magnitude by a power-law weight function in wave number, shaping its power spectrum to the desired

form. We smoothly truncate the coefficients of the highest 20% of the wavenumbers to avoid unrealistic discontinuities in the field. To obtain the surface elevation map we compute the inverse discrete Fourier transform and scale its overall magnitude to obtain the desired RMS slope at the pixel scale. This results in a height distribution with a normally distributed magnitude and uniformly distributed phase (Wu, 2000). The resulting surface directional slopes are Gaussian distributed, bi-directional slope magnitudes are Rayleigh distributed with slope aspects uniformly distributed. An example for a random rough surface with these properties can be seen in Figure 3.1b.

3.2.2 Thermophysical Model

In order to isolate the different variables that determine the surface and subsurface temperature of airless bodies, we have constructed a thermophysical illumination model. As mentioned above, this has been accomplished by employing different methods, usually involving a versatile illumination algorithm combined with a heat conduction model into the subsurface (e.g., Paige et al., 1992; Salvail and Fanale, 1994; Lagerros, 1997; Davidsson and Rickman, 2014). Our improved model includes a highly efficient illumination algorithm and an implicit subsurface heat conduction model, allowing us to achieve convergence in the subsurface temperatures using only few integration time steps.

3.2.2.1 Shadowing and Multiple Scattering

The Sun is the primary energy source for many airless bodies in the Solar System as the geothermal energy flux can usually be neglected. To estimate the intensity of incident radiation, we start with a topography represented by a matrix of size $N \times N$ square facets of equal area, denoted by their linear index i assuming values between 1 and N^2. For both the spherical craters and Gaussian random surfaces we choose $N = 100$.

For simplicity, the solar flux is computed as from a point source, smoothed in time (see Sec. 2.3). Other approaches (e.g. Davidsson and Rickman, 2014) scale the flux received

by a facet by the fraction of its vertices that are illuminated. We expect this correction to be important only near the shadow edges, therefore we consider an error of 1 pixel when determining the flux reaching pixels located in those areas.

In order to simulate shadows and reflections from the surface we adopt the Ray Casting technique (Roth, 1982). Virtual light rays are cast as probes in all directions, and their intersection points with other objects are used in order to determine the objects scale and distance from one another. This method is relatively simple but computationally intensive due to the need to find all surface-line intersections. Using predefined geometrical shapes may reduce this computational complexity, but for general non-hierarchical algorithms there is no alternative but to iterate over all elements found in the path to the source. The insolation reaching a flat sloped surface at a distance r from the Sun depends the solar incidence angle Θ, which is the angle between the surface normal and the solar vector. In order to account for shadowing we also define the shadowing function ζ, a binary function that determines whether a facet on the surface is exposed to direct solar illumination. The solar irradiance incident on the ith facet is therefore

$$F_{s,i} = S_0 \left(1 - A\right) \zeta_i \left(\frac{r_0}{r}\right)^2 \cos\Theta \tag{3.1}$$

where S_0 is the mean solar constant at Earth, r_0 is the mean Earth-Sun distance (1 AU) and A is the albedo. As a demonstration and to verify our illumination model, in Figure 3.2 we calculate the shadow area fraction on a topographic grid based on data from the Lunar Orbiter Laser Altimeter (LOLA) Smith et al. (2010) with a resolution of 20 $\mathrm{m\,px^{-1}}$ (left panel), and compare it to a picture obtained by the Lunar Reconnaissance Orbiter Camera (LROC) Robinson et al. (2010) with a resolution of $1.5\mathrm{m\,px^{-1}}$ at the same illumination conditions (right panel). To test our model accuracy we compare the shadow area fraction in the two panels and find our modeled shadow area fraction ($\sim 46\%$) agrees well with the shadow fraction measured by LROC ($\sim 47\%$). We attribute the slight difference between the calculated and measured shadow fraction to LOLA measurement and interpolation errors that slightly distort the topography (seen for example as diagonal artifacts on the top left of the model panel).

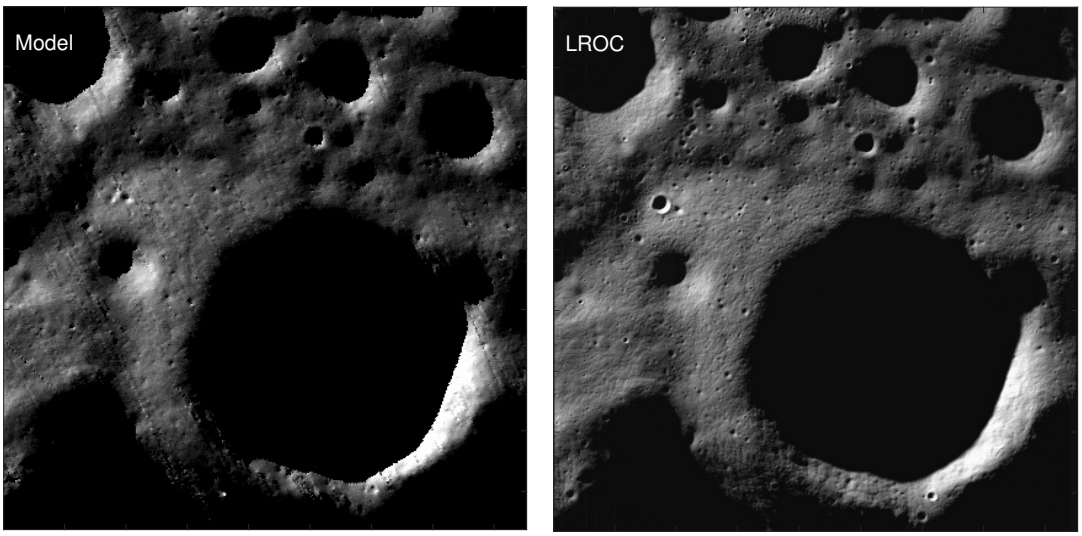

Figure 3.2: We compare our model (left) with an image captured by LROC (right) at the same illumination conditions. The modeled region is of area $\sim 10\text{km}^2$ found near latitude $\sim 86°$. We test our illumination model by comparing the shadow area fraction between the two panels, and find it is the same up to a difference of $\sim 1\%$ attributed to measurement and interpolation artifacts in the collected LOLA topography. For computational feasibility we neglect scattering in the modeled brightness map.

3.2.2.2 Mutual Visibility, Reflection and Emission

A similar technique to that above is used in order to calculate the path of rays incident from the topography itself. Naively, one could determine the visibility of one facet from another if a ray sent in the direction of the second facet intersects the surface before reaching that facet. We implement this as follows. One ray is cast directly from the source to the destination. Another ray is cast in the same azimuthal direction but along the topography. If the direct ray is anywhere found *below* the topography-following ray, the source and destination are hidden from one another. In order to compute the radiation scattered by the topography we assume Lambertian (isotropic) scattering. This assumption is valid for bodies such as the Moon, in which non-Lambertian scattering accounts for only 20% of the departure of the beaming parameter from unity (Hapke, 1996). The radiation scattered from one facet to

another can be therefore calculated by the View Factor (Baehr and Stephan, 2011), which is a measure of the angular size of each facet j as seen from the point of view of facet i,

$$V_{ij} = \frac{\cos(\phi_i)\cos(\phi_j)}{\pi d_{ij}^2} S_j, \tag{3.2}$$

where d_{ij} is the distance between the facets, S_j is the surface area of the emitting facet, and $\phi_{i,j}$ are the angles between the surface normal vector of the target emitting facet and the ray connecting them.

We may now use V_{ij} to write G_i, the incident energy flux emitted on facet i,

$$G_i = \sum_{j \neq i} (J_v + J_{IR} + J_{RIR})_{ij} \cdot V_{ij} + F_{s,i} \tag{3.3}$$

where $F_{s,i}$ is the incident solar flux (Eq. 3.1), and J_v, J_{IR}, J_{RIR} are the different radiosities; the reflected visible, emitted IR radiation and reflected IR radiation fluxes (Lagerros, 1997).

3.2.2.3 Subsurface Conduction

Airless surfaces experience a periodic change in the amount of solar flux they receive during the diurnal solar cycle, with an approximate shape of a rectified sine wave when plotted against time. In the limit of no conduction, *i.e.* radiative equilibrium, the mean surface temperature also approximates a rectified sine wave centered around local noon. Heat conduction changes the diurnal temperature cycle; the temperature maximum occurs after the local noon and is a few degrees colder. On slowly rotating bodies with low thermal inertia (such as the Moon), the equilibrium temperature of an illuminated surface at high incidence will differ from its conduction temperature by only ~ 1 K. (Bandfield et al., 2015). The heat flux being diffused into the subsurface depends on three physical properties: the material density ρ, specific heat capacity c and thermal conductivity κ. Those three properties may be incorporated into two common parameters: the thermal skin depth δ, and the thermal inertia I. The skin depth for decay of a thermal wave with a period P is

$$\delta = \sqrt{\frac{\kappa}{\rho c} \frac{P}{\pi}}. \tag{3.4}$$

The lunar regolith is highly insulating, leading to small values of skin depth, as low as several cm.

The amplitude of the temperature oscillations at the surface increases with decreasing thermal inertia, defined as $I = \sqrt{\kappa \rho c}$. In SI units, thermal inertia is measured in $\mathrm{J\,m^{-2}K^{-1}\,s^{-1/2}}$, which we abbreviate as SI. Although the thermal properties vary somewhat with depth, for simplicity we assume they are constant with depth. We choose $\rho = 700$ $\mathrm{kg\,m^{-3}}$ (Schorghofer and Aharonson, 2014) and $c = 300$ $\mathrm{J\,kg^{-1}\,K^{-1}}$, appropriate for temperatures ~ 100 K (Winter and Saari, 1969). Measurements indicate the conductivity ranges with depth between $\kappa \approx 10^{-3} - 10^{-2}$ $\mathrm{W\,m^{-1}\,K^{-1}}$ (Langseth et al., 1976), *i.e.* thermal inertia of $I \approx 15 - 45$ SI. We choose a representative value of $I = 25$ SI, but also examine the results for higher values of $I = 50$ SI and 100 SI, representative of more compact regolith at depth.

Our thermal model incorporates 1D heat conduction by solving the heat diffusion equation,

$$\frac{\partial}{\partial z}\left(\kappa \frac{\partial T}{\partial z}\right) = \rho c \frac{\partial T}{\partial t} \tag{3.5}$$

combined with a radiative boundary condition at the surface,

$$F_{\mathrm{tot}} - \varepsilon \sigma T_s^4 = -\left(\kappa \frac{dT}{dz}\right)\Big|_{z=0} \tag{3.6}$$

where F_{tot} is the incoming total flux reaching the top of the domain and T_s is the surface temperature. The above equation was solved using the semi-implicit Crank-Nicolson (Crank and Nicolson, 1947) method due to its major advantage over the simpler explicit method- it is unconditionally stable. This allows us to initialize the subsurface temperature using only a few time steps and enables us to simulate long time periods. We linearize the nonlinear emission boundary term around the temperature at the surface obtained in the previous time step. Since we neglect lateral heat conduction, our results are valid only when the skin depth is much smaller than the typical scale of the facet. In order to check the validity and accuracy of our thermal conduction model, we compared its output to known analytic solutions of simple test cases, and to other numerical models with explicit and implicit time stepping.

3.2.3 Models Errors and Uncertainties

For computational feasibility we construct an illumination model with a geometric accuracy $< 0.5°$, corresponding to a domain size of order $N^2 = 100 \times 100$ pixels. Thus, in our model, the Sun may be considered as a point source, neglecting its finite size which is also of the order of $0.5°$. Similarly we choose time steps during which the Sun moves $\sim 0.5°$ (1 h), corresponding to an error of $\sim 1\%$ in solar insolation and shadow area fraction.

The point source assumption means that the Sun does not gradually disappear or emerge from behind obstacles, but rather does so abruptly. This neglects the variations over a duration which is approximately an Earth hour near the equator and longer near the poles. To mitigate this error, we smooth the solar flux with a Gaussian filter of width equal to the time duration it takes for the Sun to travel its own size in its direction of motion in the sky. In addition, remaining consistent with our 1% error in insolation, we truncate the multiple scattering calculation after three iterations.

In order to resolve the heat wave near the surface, we used a variable spatial grid with increasing thickness from ~ 5 mm in the top layer to ~ 5 cm at depth. We model subsurface heat conduction using the Crank-Nicolson algorithm which is second-order accurate in both time and space. Due to the non-linearity of the radiative boundary condition, we maintain stability by recursively subdividing time steps during which the temperature change exceeds 10 K. In order to reach thermal equilibrium efficiently, we first run the model over a long period using a large time step (total duration of six to ten lunar days, depending on the skin-depth, with $\delta t \approx 1/30$ lunar days). To accelerate the thermal wave convergence, at the end of every lunar day we set the subsurface temperature to the surface mean.

An additional error introduced by neglecting planetary curvature is of order the ratio of the domain size to the radius of the Moon, and is small compared with the geometrical errors previously discussed. Neglecting the orbital eccentricity of the Earth introduces a $\sim 3\%$ error in the instantaneous flux, corresponding to $< 1\%$ error in the equilibrium temperature. For the maximum temperature estimates we present, we assume the maximum flux which occurs

at perihelion.

Shadowing is a non-linear process. As such, the amount of shadows (and permanent shadows) strongly depends on the shape of the topography. When calculating the area fraction of permanent shadows, we achieved convergence in simulating shadows by gradually increasing N while keeping constant the power spectrum as a function of scale, as well as the maximum nonzero wavenumber. Doing so allowed us to increase the number of facets on the surface without changing the lateral scale of the surface roughness. Since the execution time of the model is squared in N^2, our modeled surfaces are of size $N = 100$ facets. Relative to surfaces with size $N = 1000$ facets, our model underestimates the permanent shadows area fraction by $\sim 7\%$.

3.3 Results

We begin by examining the relation between the temperature distribution and the slope distribution for two different topographic reliefs: a bowl-shaped crater and a surface with a Gaussian slope distribution. Next, we utilize these results to find the spatial distribution of cold-traps at and below the surface, and give estimates to the cold-trap area fraction on lunar rough surfaces. In order to isolate the effect of roughness on the temperature distribution we first neglect obliquity. Later, we include the Moon's obliquity when we estimate the cold-trap area fraction on lunar rough surfaces.

3.3.1 The Temperature Distribution of Hemispherical Craters

Following the treatment of Ingersoll et al. (1992), we consider a spherical crater as a cavity shaped as a portion of a sphere surrounded by a flat plane. As mentioned above, the geometry of the crater is defined by its depth to diameter ratio, Δ.

A well known analytic expression exists for the shadow temperature of a bowl-shaped crater (Buhl et al., 1968; Ingersoll et al., 1992). In this idealized model that excludes conduction and assumes Lambertian scattering, the walls act to disperse the incident radiation

equally over the shadowed part of the crater. Consequentially, the radiative equilibrium shadow temperature is uniform and given by

$$\sigma T^4 = F_0 \sin e_0 \frac{f(1-A)}{(1-Af)} \left[1 + \frac{A(1-f)}{\varepsilon}\right] \tag{3.7}$$

where e_0 is the solar elevation angle, $f = 1/(1+1/4\Delta^2)$, A is the albedo, ε is the IR emissivity and $\sigma = 5.67 \times 10^{-8}$ W m^{-2} K^{-4} is the Stefan-Boltzmann constant. At low latitudes this shadow is transient, but at higher latitudes, a portion of this shadow may persist throughout the lunar day. Transient shadow regions retain heat in the subsurface, leading to a doubly peaked shadow temperature distribution with cold persistent shadows and warmer transient shadows.

As a validation to our model, we simulate the temperature distribution of a spherical crater with $\Delta = 1/8$ at high latitude, assuming different values of thermal inertia I (Figure 3.3), and compare the results to those predicted by Ingersoll et al. (1992). We find, as expected, that with decreasing thermal inertia the shadow temperatures computed by our discrete model approach the analytic result that assumes radiative equilibrium. In addition, we find that the maximum shadow temperature is lower than the equilibrium value and delayed past local noon. For example, the peak shadow temperature of the $I = 50$ SI case in Figure 3.3 is $\sim$ 10 K lower than the equilibrium value and appears at a $\sim$ 1 lunar hour ($\sim 12.5^\circ$ incidence angle) delay compared to equilibrium models. As mentioned above, the shadow temperatures exhibits a bimodal distribution, ascribed to the two types of shadows found in a realistic crater: transient and persistent. At this latitude (80°), transient shadows cover a comparable area to persistent shadows and are approximately 20 K - 40 K warmer. These factors limit the total area inside the crater that can hold volatiles in stable state.

In the next section we utilize these results in order to determine how this shadow and temperature distributions affect volatile stability.

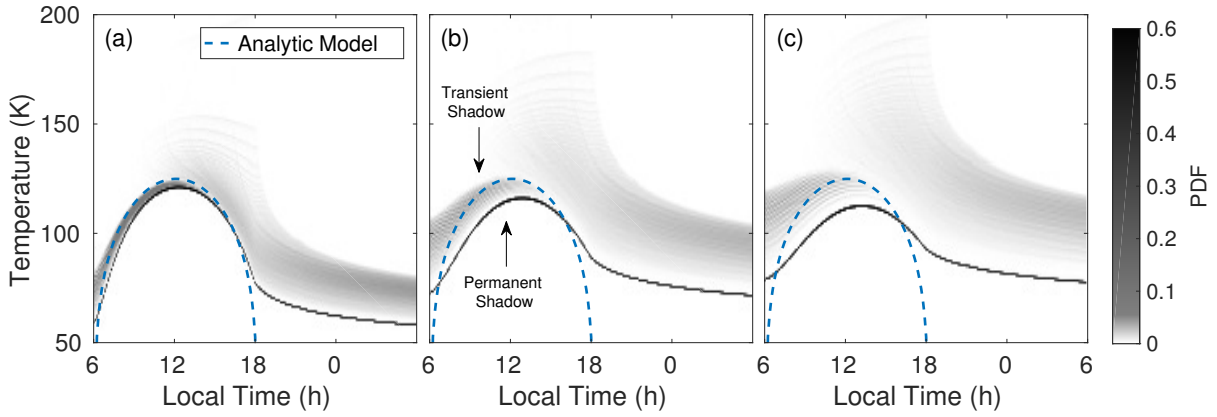

Figure 3.3: Shadow temperatures within a hemispherical crater at latitude 80° with depth to diameter $\Delta = 1/8$ and different thermal properties, plotted against local time. (a) Material with $I = 100$ SI (corresponding to $\delta \approx 40$ cm) (b) $I = 50$ SI ($\delta \approx 20$ cm), and (c) $I = 100$ SI ($\delta \approx 40$ cm). The blue line shows the analytic temperature of the shadow derived by Ingersoll et al. (1992). The gray shading presents the probability distribution function of shadow temperature, sampled in bins of width $\Delta T = 1$ K. For each local time, two types of shadows can be distinguished: a cold, permanent shadow and a warm shadow that was temporarily illuminated during the lunar day.

3.3.2 The Temperature Distribution of Rough Random Surfaces with a Gaussian Slope Distribution

We chose to quantify the lunar terrain roughness outside simple craters by assuming its slope distribution is Gaussian with an RMS slope magnitude σ_s. Smith (1967b) derived expressions relating σ_s and the solar incidence angle to the area fraction of shadows covering such a surface. Others (*e.g.* Hapke (1996); Sun (2007); Bandfield et al. (2015)) have shown scattering must be accounted for in order to accurately model the temperature distribution at high incidence angles, and did so employing different approximations. Our ray casting model allows us to simulate the temperature distribution at high incidence angles by accurately accounting for obscuration, scattering and infrared radiation. Previously, Mazarico et al. (2011) and others used measured lunar topography with similar illumination mod-

els to investigate the spatial distribution of lunar permanently shadowed regions (PSRs) at high latitudes. Our treatment of the problem is a statistical one, and as such, focuses on investigating how parameters like roughness and thermal inertia affect the temperature distribution. Therefore, while the surface slope distribution of the Moon may deviate somewhat from Gaussian (Rosenburg et al., 2011b), we focus on this idealized and thus more easily parameterized representation of the topography. All random surfaces were modeled using a power-law spectrum characteristic of lunar highlands (Rosenburg et al., 2011b).

In Figure 3.4, we plot the maximum diurnal temperature distribution for surfaces with different roughness values at different latitudes. When discussing the minimum or maximum values of a distribution, we refer to the values of the distribution at the 2nd and 98th percentile points to provide a robust estimation with respect to outliers (the results are insensitive to this choice of percentile). As expected, all distributions are bimodal; the colder mode corresponds to the shadowed part of the surface, and the warmer mode corresponds to the illuminated, radiatively equilibrated, part of the surface.

As roughness increases, the number of shadows on the surface increases due to the higher probability for obscuration (as shown by Smith (1967b)). The maximum temperature of the surface increases as well, because at high latitudes rougher surfaces have more sun-facing slopes at a higher typical incidence angle. The temperature of shadowed slopes consequently increases due to their lower sky to ground ratio as well as their exposure to warmer, illuminated slopes. As latitude increases, the typical incidence angle grows, thus increasing the abundance of shadows, but the maximum surface temperature decreases due to the higher solar zenith angle. These two factors controlling the maximum temperature of shadows are revisited below when evaluating ice stability.

3.3.3 Stability of Surface Ice

Having computed the temperature distributions of hemispheric craters and random Gaussian fields, we now turn to consider ice stability. To obtain realistic estimates, we include the

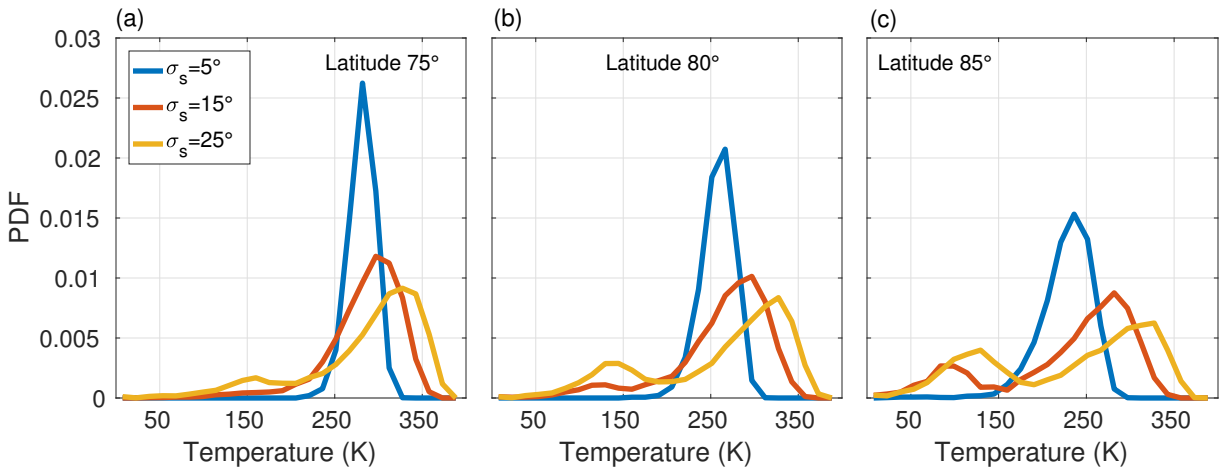

Figure 3.4: The maximum temperature distribution of nine rough surfaces with different slope RMS magnitude σ_s and latitude, above a conductive subsurface with $I = 25$ SI ($\delta \approx 10$ cm) Roughness acts to raise the maximum temperature of both illuminated facets (shifting the rightmost mode of the distribution) and shadowed facets (leftmost mode), as well as to increase the abundance of shadows on the surface (changing the relative heights of the two peaks).

effects of the Moon's obliquity, which modifies the azimuths of sunrise and sunset at a given location. This alters the cold-traps area fraction by exposing additional slopes to sunlight. To constrain the cold-trap distribution accounting for the Moon's obliquity, we set the solar declination equal to the obliquity throughout the lunar day. Keeping the solar declination constant introduces an error in the solar azimuth which is largest at sunrise and sunset. However, during one lunar day the solar declination changes only by $\sim 0.13°$, affecting the sunrise and sunset azimuths by $\lesssim 1°$, within our model accuracy. Thus, this allows us to place a lower limit on the area fraction of cold-traps.

In vacuum, the evaporation rate of a volatile material depends upon the vapor pressure and the temperature (Langmuir, 1913; Watson et al., 1961),

$$E = P_v \sqrt{\frac{\mu}{2\pi RT}} \tag{3.8}$$

where μ is the molecular weight, R is the gas constant and T is the temperature. The vapor pressure P_v can be obtained using

$$P_v = P_t \exp\left[-\frac{Q}{R}\left(\frac{1}{T} - \frac{1}{T_t}\right)\right] \tag{3.9}$$

where P_t and T_t are the triple point pressure and temperature, Q is the sublimation enthalpy, and R is the gas constant. The evaporation rate and the cold-trap stability are thus extremely sensitive to changes in temperature. For example, for a mass loss rate of water ice of 1 mm Ga^{-1} the deposit must not exceed a temperature of $\approx$ 101.8 K (Schorghofer and Taylor, 2007). We define this cold-trap stability threshold as T_{ct}. The choice of 1 mm Ga^{-1} is somewhat arbitrary but commonly used (*e.g* Paige et al. (2010b)), and corresponds to predictions for the amount of ice accumulated in craters following a cometary impact (Stewart et al., 2011).

3.3.3.1 Simple Craters

Illuminated slopes on the Moon reach radiative equilibrium quickly. For incidence angles $> 0.5°$ the incoming solar flux is > 10 W m^{-2}, enough to raise the surface temperatures above T_{ct}, limiting cold-trap formation almost entirely to PSRs. PSRs still receive radiation through self-heating, *i.e.* thermal emission and scattering from nearby slopes. As mentioned above, hemispherical craters have the property that the illuminated walls evenly distribute reflected and emitted radiation throughout the interior shadows (Buhl et al., 1968; Ingersoll et al., 1992).

In Figure 3.5a we show how the crater's depth and latitude affect its permanently shadowed area fraction (PSR area fraction) and its self-heating. The marker size represents the crater depth to diameter ratio and its color represents the latitude. The dashed black line marks the threshold flux, above which the PSR equilibrium surface temperature increases above T_{ct}. To test for stability, we first find the temporal maximum of the self-heating flux at each location, and report the median value for all permanently shadowed locations. Thus for example, half of the PSRs on surfaces plotting on the dashed line are cold-traps. The

vertical distance from the dashed line can be regarded as a gauge of the fraction of PSRs that are cold enough to trap volatiles.

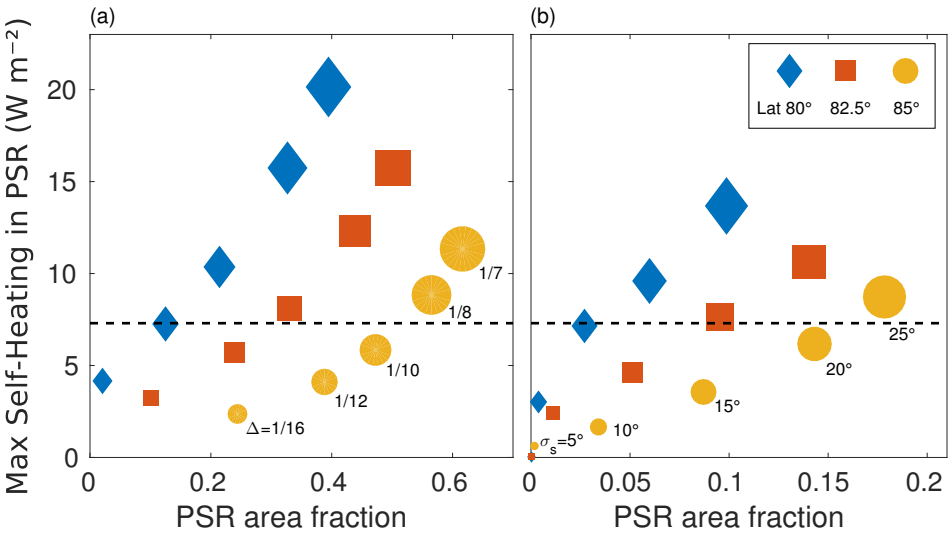

Figure 3.5: The amount of permanently shadowed regions and the maximum self-heating within them at different latitudes indicated by color and marker shape, above a conducting subsurface with $I = 25$ SI ($\delta \approx 10$ cm). (a) Hemispherical craters with marker size indicating the crater's depth to diameter ratio. (b) Rough surfaces with marker size indicating the RMS slope, where each point is obtained by averaging over five realizations of different random rough surfaces with a given σ_s. In both panels the black dashed line shows the threshold flux below which equilibrium temperatures are lower than the temperature defining surface cold-traps $T_{\rm ct}$.

While the PSR area fraction increases with the crater's depth, the crater self-heating increases as well. As a result, despite their substantial PSR fractions at low latitudes, deeper craters can trap volatiles only at high latitudes. For example, deep craters with $\Delta = 1/8$ produce roughly the same amount of self-heating at latitude 85° as shallow craters with $\Delta \sim 1/12$ at latitude 80°. The crater self-heating continues to increase with the crater depth, as the sky to ground visibility ratio of slopes within the crater decreases.

Subsurface conduction alters the temperature distribution of bowl-shaped craters compared to models assuming thermal equilibrium. In thermal disequilibrium, the crater has

a shadow temperature distribution with two peaks that correspond to two types of shadows: transient and permanent. Transient shadows typically cannot be cold-traps since their maximum diurnal temperature exceeds T_{ct}. Permanent shadows have a lower maximum diurnal temperature than predicted by equilibrium models when accounting for conduction, and hence equilibrium models are inaccurate in computing cold-trap stability. To assess the effect of conduction on ice stability, we first find the peak diurnal temperature of every location within the crater, and then find the spatial minimum of the result (Figure 3.6a). Plotting this temperature shows that for crater aspect ratios and latitudes where permanent shadow exists, analytic models may be used to estimate the temperature (with inaccuracies that depend on the thermal conductivity). The threshold latitude where permanent shadow no longer exists decreases for higher depth to diameter craters, as shown by the direction of the gray arrow in figure 3.6a. While steep craters have more stable PSR fraction than shallow craters, their geometry results in higher scattered radiation, raising the temperature of these shadows.

Considering the effect of the crater geometry and its thermal properties, we show in Figure 3.6b the lowest latitude at which cold-traps still exist in bowl-shaped craters with different geometries. The two limiting factors discussed above are demonstrated in this figure as two regimes; deeper craters are found in the scattering regime at which cold-traps are limited by the scattered and re-emitted radiation within the crater, while cold-traps in shallower craters are limited by the presence of permanent shadows. In the scattering regime, higher subsurface conductivity lowers the PSR temperatures. However, in the shadowing regime subsurface conduction has little effect as the surface reaches thermal equilibrium quickly when exposed to solar flux that dominates the heat budget. An optimal crater geometry that promotes ice stability is therefore found at $\Delta \sim 1/13 - 1/14$. Despite the stable shadows they cast, deep craters ($\Delta \sim 1/10$ and above) can only hold stable ice at polar latitudes $\gtrsim 80^\circ$ for lunar-like thermal inertia, $I \sim 25$ SI.

We test our prediction using data obtained by the Lunar Reconnaissance Orbiter (LRO) Diviner radiometer experiment (Paige et al., 2010a). During its mission, Diviner measured

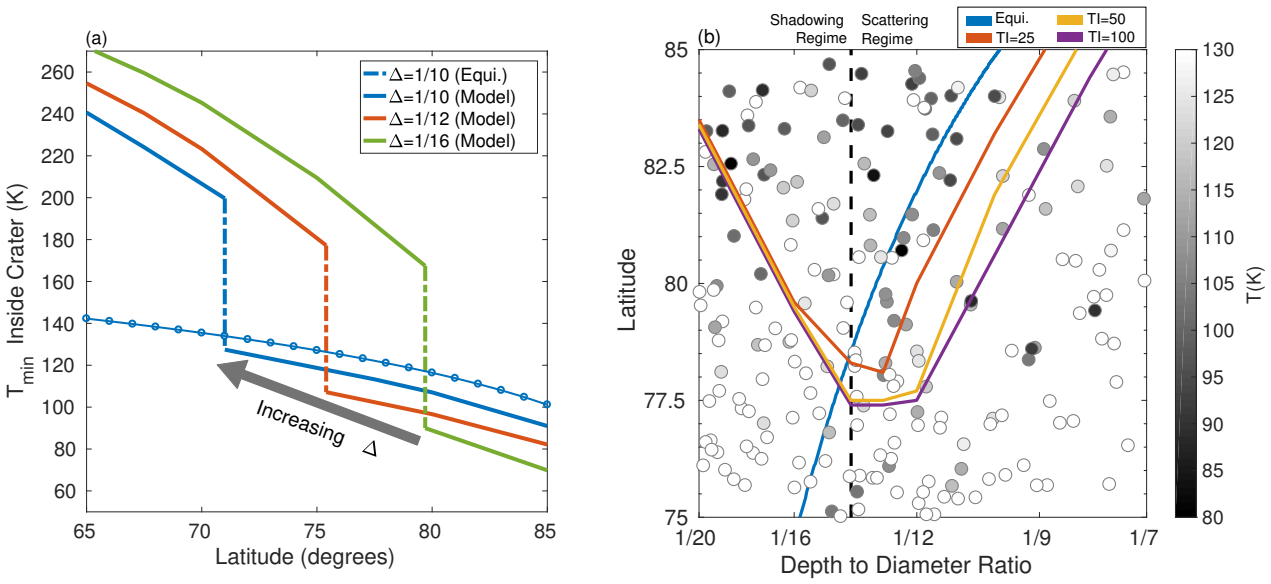

Figure 3.6: (a) The temporal maximum and spatial minimum temperature within a bowl shaped crater, plotted for several different geometries, compared to the temperatures predicted by the Ingersoll et al. (1992) analytic model (connected circles) for $\Delta = 1/10$. The numerical model is similar to the equilibrium model predictions in latitudes where the shadow is permanent. The discontinuity marks the transition at which the crater no longer casts a permanent shadow, and occurs at lower latitudes for higher depth to diameter craters (gray arrow). (b) The lowest latitude at which ice is still stable inside bowl shaped craters, considering different crater geometries and thermal properties, compared to the equilibrium temperature predicted by Ingersoll et al. (1992). Ice stability is limited by the persistence of shadows in shallow craters and by scattering and thermal emission in deep craters. An optimum occurs at $\Delta \sim 1/13 - 1/14$. The gray circles mark craters near the lunar poles; filled circles represent craters that can hold stable ice (cold-traps) according to their measured maximum temperatures. The thermal parameters are as in Figure 3.3.

the annual maximum temperatures of the lunar poles with a resolution of 240 m px^{-1}. We find the temporal maximum and spatial minimum temperatures inside small (8 – 30 km) lunar craters (Salamunićcar et al., 2014) and plot their latitudes and depth to diameter ratios in Figure 3.6b. The crater maximum temperature is indicated by its shading.

As expected, we find that the equilibrium curve (Ingersoll et al., 1992) cannot fully explain the cold-trap distribution in Figure 3.6b, as it does not account for the persistence of shadows (bottom left) or subsurface conduction (top right). Accounting for these factors allows a better match of the model to the measured boundary of ice stability in these crater geometries and latitudes. While the majority of craters measured to be cold-traps are found in the predicted ice stability region, some plot outside this region, due to local topographic variations which we do not model. These anomalies are mostly evident in the scattering regime, where craters formed within relatively warm PSR of larger, shallower craters may be cold enough to trap water ice. Similarly, craters measured to be too warm (empty circles) are found above the critical latitude and correspond to craters with non bowl-shaped topography. The modification of the topography of these craters disrupts their protective shape over all azimuths necessary for cold-trapping.

3.3.3.2 Rough Random Surfaces with a Gaussian Slope Distribution

The closed shape (in map view) and steep rims of craters promote the persistence of shadows compared to random topography as the Sun sweeps around in azimuth. While less stable, PSRs outside craters are usually colder due to their higher sky to ground visibility ratio. Here we simulate ice stability on several rough random surfaces with different σ_s above a conductive subsurface with $I = 25$ SI. The area fraction covered by cold-traps is obtained by integrating maximum temperature distribution functions similar to those appearing in Figure 3.4 (but with non-zero obliquity) up to the cold-trap stability criterion temperature $T_{\rm ct}$.

Figure 3.7a shows the ice stability area fraction for five random rough surfaces with different σ_s, for several representative latitudes. Rosenburg et al. (2011b) found that near the lunar poles, the RMS slope at a scale > 1 km is roughly $\sigma_s \sim 5°$, while the median bidirectional slope at the ~ 17 m scale is 7.5°, which corresponds to $\sigma_s \sim 10°$.

We find that on smoother surfaces ($\sigma_s < 5°$) water ice is either unstable or can only

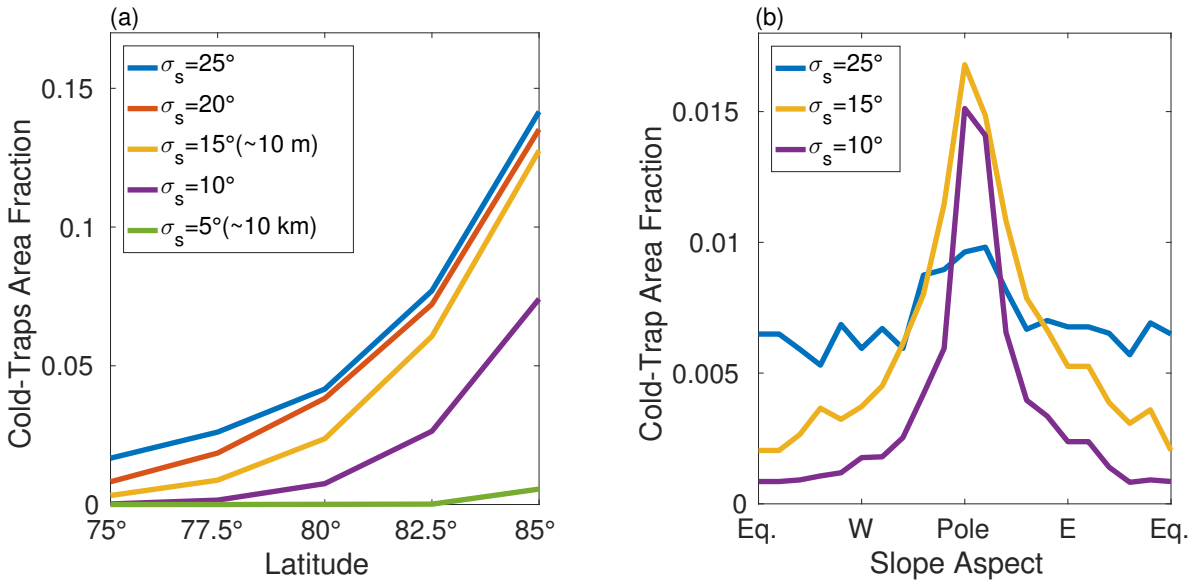

Figure 3.7: (a) Ice stability area fraction modeled on Gaussian random surfaces with varying σ_s and $I = 25$ SI ($\delta \approx 10$ cm), showing the area fraction of cold-traps increases with latitude and roughness. Surfaces with $\sigma_s = 15°$ which correspond to roughness on scales of ~ 10 m have a $10 - 15\%$ cold-trap area fraction coverage at polar latitudes. Each curve is obtained by averaging over five different realizations of a random rough surface with the same σ_s. (b) Differential histogram of cold-trap area as a function of slope aspect at latitude 85°, computed in 20° azimuth bins. On smoother surfaces ($\sigma_s = 10°, 15°$) cold-traps exist predominantly on pole-facing slopes, while on rougher surfaces ($\sigma_s = 25°$) the aspect distribution becomes more uniform.

persist in small quantities, even in high latitudes, due to the limited area fraction covered by shadows. This can also be seen in Figure 3.4, where even in zero obliquity PSRs are not abundant on the surface. For higher roughness values, a significant fraction of the area acts as cold-traps above latitude 80°. We find the $\sigma_s = 10°$, 15° curves of particular interest as they correspond to the measured value for lunar topography on scales of tens to hundreds of meters. At this roughness, Gaussian random fields exhibit $\sim 5 - 13\%$ cold-traps by area, depending on latitude. Topography with higher roughness values (higher σ_s) corresponds to either much smaller scales on the Moon, which requires modeling of lateral heat conduction,

or areas near local features such as craters rims, whose slope distributions are non-Gaussian. Topography with a lower slope RMS corresponds to larger scales of order kilometers, in which cold-traps have already been mapped in the past (Mazarico et al., 2011; McGovern et al., 2013). On those scales, ice can only be stable within protective topographic features like craters.

Although generally the cold-trap fraction increases with both roughness and latitude, at latitudes higher than $\sim 82^\circ$ we find the rougher surfaces ($\sigma_s = 15^\circ - 25^\circ$) have similar cold-trap area fraction (sometimes even decreasing with roughness, in some individual cases). We interpret this by considering the two competing factors mentioned above that influence ice stability: the area fraction and maximum temperature of PSR. Higher surface roughness creates potential cold-traps by increasing the area fraction of shadows, but at the same time also destroys cold-traps by increasing the maximum temperature of these shadows. This may also be seen by considering the diagram shown in Figure 3.6b; higher surface roughness (indicated by the marker size) increases the shadow area fraction but decreases the typical incidence angles at high latitude, thereby increasing the maximum reflected and emitted flux into the shadows. However, higher latitude (indicated by the marker color) increases the shadow area fraction as well as the typical solar incidence angles, thereby always decreasing the maximum reflected and emitted flux into the shadows.

In order to model how the slope directionality (aspect) affects ice stability we first distinguish between two types of shadows. Self-shadows are cast by a slope on itself when the Sun sets below its local horizon, while mutual shadows are cast when one slope obscures the Sun from another slope. Permanent self-shadowing can only occur for slopes that face away from the Sun throughout the solar cycle, while mutual permanent shadowing depends on non-local terrain properties.

Permanent self-shadowing is impossible on bodies with nonzero obliquity, since at summer solstice pole-facing slopes will always be exposed to sunlight during sunrise and sunset (unless obscured by another slope). However, with their lower insolation and temperatures, pole-facing slopes are still considered more stable cold-traps than equator-facing slopes. Figure

3.7b shows the cold-trap slope aspect distribution on two surfaces at latitude 85°. While cold-traps on smoother ($\sigma_s = 10°$) surfaces are more probable on pole-facing slopes, cold-traps on rough ($\sigma_s = 25°$) surfaces are more isotropically distributed. This may be understood by examining the dependence of the slope aspect on the amount of radiation it receives. Cold-traps are formed almost exclusively in permanent shadows which are cast isotropically. However, as seen above, cold-traps can also be destroyed by incoming emitted and reflected flux from nearby slopes. Pole-facing slopes receive less insolation than equator-facing slopes, regardless of roughness. However, pole-facing slopes also receive more scattered and emitted radiation from equator-facing slopes, which are typically exposed to more insolation than all the other slopes on the surface. Since higher roughness decreases the typical sky to ground ratio of slopes, cold-trapping pole-facing slopes will be more readily destroyed on rough surfaces compared to smoother surfaces. Therefore, on smoother surfaces (scale $\sim$ 10 km), cold-traps tend to form predominantly on pole-facing slopes. On rougher surfaces (scale $\sim$ 10 m and below), the cold-trap aspect distribution is nearly isotropic. Observations by the Lunar Exploration Neutron Detector (LEND) have been suggested to indicate hydrogen distribution that is asymmetric in slope directionality (McClanahan et al., 2015), but it is not clear if these observations correspond to the anisotropy predicted here for Gaussian surfaces.

3.3.4 Stability of Subsurface Ice

The maximum temperature required for ice stability greatly limits the area fraction of surface cold-traps on the Moon. However, due to the diffusion barrier created by the overlaying regolith, the subsurface may harbor ice even in places where stability is not possible on the surface. The presence of ice in the subsurface depends on delivery mechanisms such as gardening (*e.g.* Hurley et al. (2012)), diffusion under present conditions ((Schorghofer and Taylor, 2007; Schorghofer and Aharonson, 2014) or under conditions that occurred in a past orbital state (Siegler et al., 2011, 2016). Next, we consider only the potential survival of ice in the subsurface, noting that ice quantities depend on accumulation via one of the mechanisms mentioned above.

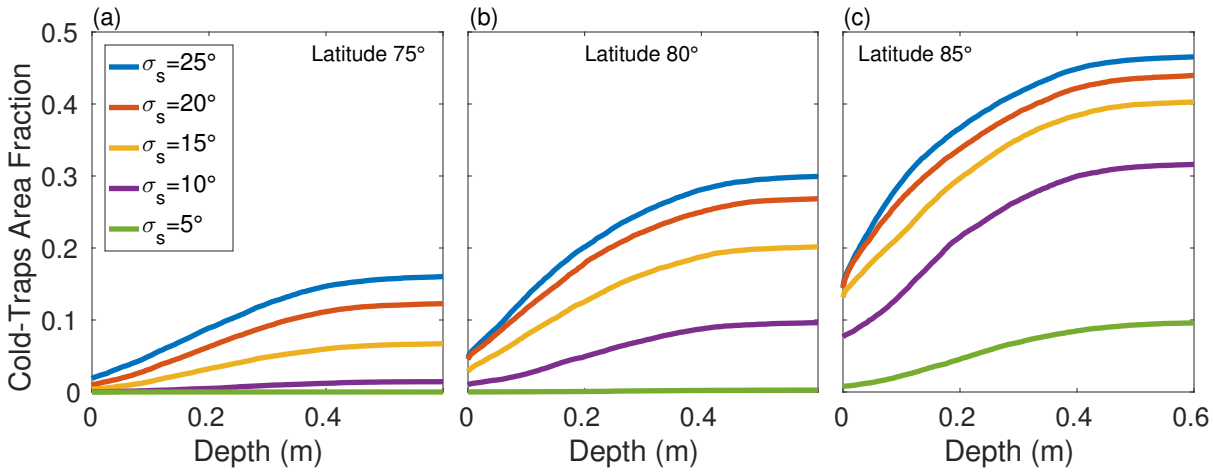

Figure 3.8: The subsurface cold-trap area fraction for different latitudes and roughness values for $I = 25$ SI ($\delta \approx 10$ cm). For smooth surfaces ($\sigma_s < 5°$) subsurface ice cannot persist below latitude 80°. Greater roughness makes it possible for subsurface cold-traps to survive even in lower latitudes. As temperature stabilizes at depths below a skin depth, the area fraction ceases to increase. Each curve is obtained by averaging five realizations of random surfaces with a given σ_s.

To simulate subsurface ice stability we use the criterion derived in Schorghofer and Taylor (2007). The mass loss rate of ice from the subsurface J depends on the evaporation rate into vacuum $E(T)$ (Eq. 3.8) and the thickness of the covering layer Δz,

$$J = \frac{\mu \ell}{2} \frac{E(T)}{\Delta z} \tag{3.10}$$

where μ is the mass of an H_2O molecule and ℓ is the pore size taken to be 75 µm, typical for lunar soil (McKay et al., 1974; Heiken et al., 1991). In order to estimate the abundance of subsurface cold-traps, we consider the maximum temperature obtained at every depth within a regolith of $I = 25$ SI and find the depth where the predicted loss rate from Eq. 3.10 exceeds 1 mm Ga^{-1}; this defines the *depth to ice stability*; the thickness of an overlaying regolith above a region where macroscopic ice quantities may survive for $\sim 10^9$ years.

As is the case for surface ice, the stability of subsurface ice increases with both latitude and roughness. Figure 3.8 shows the amount of subsurface cold-traps found beneath several

random Gaussian surfaces with different roughness values, located at different latitudes. Here again, at polar latitude (85°) rough surfaces ($\sigma_s \sim 15° - 25°$) show little dependence of the cold-trap fraction on surface roughness, compared to lower latitudes and smaller roughness values, where the cold-trap fraction increases with roughness. Additionally, we find that some ice can remain stable even under temporarily illuminated slopes, making it more readily accessible than surface ice that exists only inside PSRs. In Figure 3.9a we show a cross-section through the subsurface below one of the simulated random topographies, with $\sigma_s = 15°$ at latitude 85°. Permanently shadowed slopes (profile A in Figure 3.9b) can trap water ice both on and below the surface for periods > 1 Ga. Temporarily illuminated slopes (profile B) cannot trap volatiles on the surface, however ice may become stable deeper in the subsurface due to the diffusion barrier and the decaying thermal wave amplitude. For higher surface temperatures (profile C) ice is not stable both on and below the surface. The area fraction of cold-traps increases with depth due to the added stability.

However, deeper than a few skin depths the temperature remains relatively constant and the added stability depends on the thickness of the diffusion barrier alone. For high enough temperatures, the wave amplitude may not decay below the temperature stability criterion, and ice will become stable again only where a much thicker diffusion barrier can counteract the higher evaporation rate. For example, at a temperature of 120 K, ice will first become stable at ~ 40 cm, but at a temperature of 135 K ice will only first become stable at > 100 m. This result limits the maximum burial depth of ice to a few decimeters, with no mechanisms that can currently lead us to expect burial at greater depths than a few meters.

The amount and burial depth of cold-traps varies with the subsurface properties. Increasing the subsurface conductivity lowers the surface maximum temperatures, resulting in a slightly higher surface cold-trap area fraction. However, the skin depth of more conductive subsurfaces is also higher, destroying subsurface cold-trap and increasing the thickness of the covering layer. For example, doubling the modeled skin depth (to 20 cm instead of the modeled 10 cm) reduces the amount of subsurface cold-traps by $\sim 50\%$. Therefore, we conclude that the Moon's relatively high subsurface cold-trap area fraction (compared to the

surface) is facilitated by its low subsurface thermal inertia at low ($\sim$ 100 K) temperatures.

In Figure 3.9c we compare the area fraction of surface cold-traps to the area fraction of subsurface cold-traps at a depth of 50 cm. We find that for nearly all modeled surface roughness values, the area fraction of cold-traps more than doubles in the subsurface. In nearly polar latitudes, slopes on scales of $\sim$ 10 m (Rosenburg et al., 2011b) may harbor over 50% subsurface cold-traps by area coverage. At smaller scales, lateral heat conduction may change this result and limit the area fraction of cold-traps. In addition, while cold-traps cannot exist in significant abundance below latitude 80°, subsurface cold-traps can survive on relatively rough surfaces (scales of $\sim$ 10 m) even at latitude 75°. Burial of surface ice (e.g. Hurley et al. (2012); Schorghofer and Aharonson (2014)) may seem less probable in those latitudes due to the lack of a surface source, however recent work (Siegler et al., 2016) suggests polar wander on the Moon may resulted in the burial of ice at lower latitudes.

3.4 Conclusions

Surface topography and roughness are prominent factors in determining the temperature on airless planetary bodies. By using illumination, scattering, and thermophysical models of the lunar surface, we find that accounting for subsurface conduction lowers the shadow temperature of hemispherical craters compared to known analytic models (Buhl et al., 1968; Ingersoll et al., 1992) by $\sim 5 - 15$ K. Additionally, by accounting for subsurface conduction, we distinguish between two types of shadows that appear in a realistic topography: a warmer, temporary shadow and a cold, persistent shadow. These result in a bimodal shadow temperature distribution.

Assuming random Gaussian surfaces to simulate the temperature distribution on rough surfaces, we again observe a bimodal maximum temperature distribution in high latitudes, owing to the colder, permanently shadowed and the warmer, illuminated slopes. The size of these two modes depends on the surface roughness and latitude; surfaces at higher latitudes and with higher roughness generally have more abundant PSRs, increasing the size

of the colder mode of the distribution. However, higher roughness also increases the surface scattered and emitted radiation, increasing the temperature of these shadows. Therefore, in high latitudes, the cold-trap area fraction of rough surfaces is comparable.

The resulting temperature distributions may be used to determine surface and subsurface ice stability. We find the cold-trap area fraction in craters is limited by their geometry and, to a lesser extent, by the subsurface thermal properties. Deeper craters have more persistent but warmer shadows due to scattering and thermal emissions from the illuminated parts of the walls. Deep craters are more likely to have permanent shadows compared to shallower craters at the same latitude, but these shadows are often too warm to trap volatiles for geologic time periods. We find that the geometry of craters with $\Delta \sim 1/12 - 1/14$ promotes ice stability optimally, allowing cold-trap stability at latitudes as low as $\sim 77^{\circ}$. When comparing our results with the maximum temperature map obtained by LRO Diviner, we find some agreement, although for realistic craters the theoretical ice stability prediction is sometimes disturbed by local topography.

For random surfaces, as roughness increases, the colder mode of the bimodal distribution grows in size (due to added shadows) and shifts towards warmer temperatures (due to the lower sky to ground ratio of sloped surfaces). Near the poles, higher roughness increases the area fraction of permanent shadows, potentially adding cold-traps. However, it also increases the maximum temperature of those shadows, destroying potential cold-traps. The result of the competition between these two factors is that at high latitudes rough surfaces have cold-trap area fractions that only weakly depend on roughness. However, we find that the cold-trap slope aspect (directionality) depends on the surface roughness. On smoother surfaces (scales > 100 m), cold-traps are predominantly pole facing. However, we find that as roughness grows the cold-trap slope aspect distribution becomes more isotropic, due to increased reflected and emitted radiation pole-facing slopes receive. We further find that the abundance of subsurface cold-traps increases with growing roughness and latitude, so that at polar latitudes, rough surfaces (corresponding to scales < 10 m), have a $\sim 30\%$ cold-trap area fraction at a depth of 50 cm, compared to $\sim 5 - 15\%$ on the surface. Additionally,

even where unstable on surface due to lack of permanent shadow, we find that on scales > 1 km subsurface ice may persist in non-negligible (10%) quantities below random topography at decimeters depths. At temperatures above 130 K, the maximum subsurface temperature only falls below the cold-trapping criterion beneath a thick diffusion barrier, of depth > 10 m. Since the supply of ice available to accumulate below depths of a few meters is limited, we constrain the maximum possible burial depth of ice below rough surface to a few decimeters. The stability of subsurface ice in transiently illuminated regions could prove important to future missions to the lunar poles, as such areas are more readily accessible than the usually proposed permanently shadowed regions.

Acknowledgments

This project was supported by the Lunar Reconnaissance Orbiter project, the Helen Kimmel Center for Planetary Science, the Minerva Center for Life Under Extreme Planetary Conditions and by the I-CORE Program of the PBC and ISF (Center No. 1829/12). LR would like to thank Norbert Schörghofer for helpful advice.

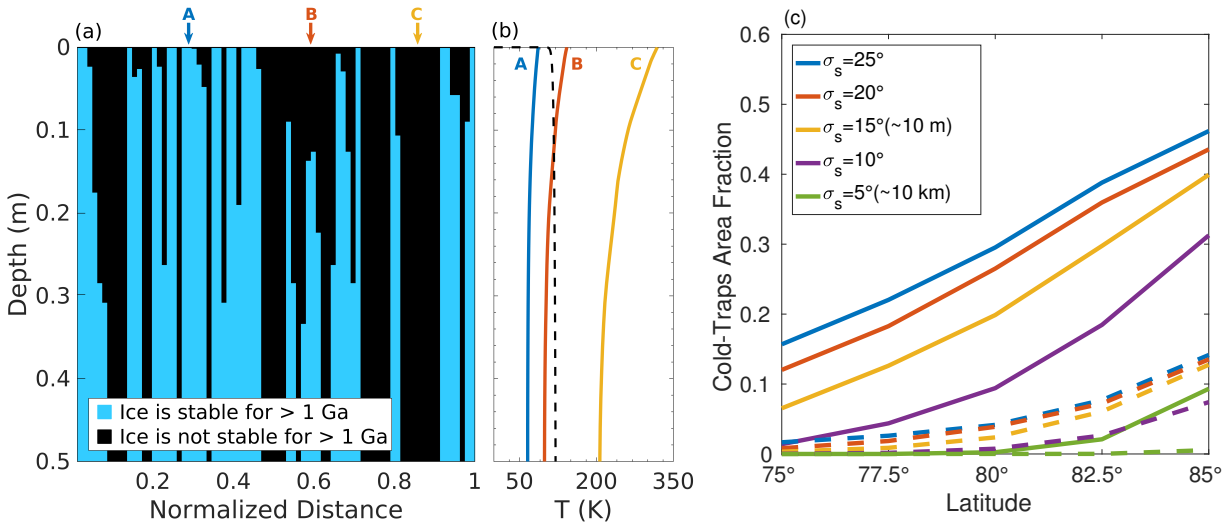

Figure 3.9: (a) A cross-section through a subsurface with $\sigma_s = 15°$ at latitude 85° showing the amount of subsurface cold-traps. Profile A shows the amount of subsurface cold-traps below a PSR, where ice is stable both on and below the surface. Profile B shows the subsurface below a temporarily shadowed area, where ice is not stable on the surface but becomes stable at depth due to the diffusion barrier and the decaying thermal wave amplitude. Profile C shows an area in which cold-trap are not stable both on and below the surface. (b) The maximum subsurface temperature for the three profiles, along with the criterion for subsurface ice stability (dashed line) given by Schorghofer and Taylor (2007). (c) A comparison between the amount of surface cold-traps (dashed) and subsurface cold-traps at a depth of 50 cm (solid) plotted for different latitudes and surface slope RMS, σ_s. In nearly all latitudes, the area of cold-traps more than doubles in the subsurface. The thermal parameters are as in figure 3.8.

CHAPTER 4

Ice In Micro Cold-Traps on Mercury: Implications for Age and Origin

This chapter was originally published in: Rubanenko, L., Mazarico, E., Neumann, G.A. and Paige, D.A., 2018. Ice in micro cold traps on Mercury: implications for age and origin. *Journal of Geophysical Research: Planets*, 123(8), pp.2178-2191.

Abstract

Evidence in radar, reflectance, and visible imagery indicates surface and subsurface water ice is present inside permanently shadowed regions (PSRs) in the north polar region of Mercury. The origin of this ice and the time at which it was delivered to the planet are both unknown. Finding the smallest, most easily eroded, ice deposits on Mercury can help answer these questions. Here we present evidence for volatiles trapped in cold-traps of scales $\sim 1 - 10$ m. We consider two possible delivery methods for these deposits: a gradual, slow accumulation by micrometeorites or solar wind implantation and an episodic deposition, either primordial or by a recent comet impact. We conclude the mechanism that best explains the presence of volatiles in these micro cold-traps is a comet impact that most likely occurred in a last ~ 100 Ma.

4.1 Introduction

It has long been known that high latitude topographic depressions on low obliquity, airless planetary bodies cast shadows that may persist for geologic time periods (Urey, 1952). If

sufficiently cold, these permanently shadowed regions (PSRs) may trap and preserve volatiles for billions of years inside cold-traps (Watson et al., 1961; Arnold, 1979).

On Mercury, thermal models of the surface and subsurface showed water ice may persist inside polar craters (Paige et al., 1992; Ingersoll et al., 1992; Vasavada et al., 1999; Paige et al., 2013). More recently, evidence for the presence of thick ice deposits near the north pole of Mercury was bolstered by several independent measurements. Earth-based radar observations have found anomalously bright regions suggestive of ice deposits which are at least a few meters thick (Slade et al., 1992; Harmon and Slade, 1992; Butler et al., 1993; Harmon et al., 2001, 2011). Near infrared (IR) surface reflectance measurements obtained by the Mercury Laser Altimeter (MLA) on board the MErcury Surface, Space ENvironment, GEochemistry, and Ranging (MESSENGER) spacecraft detected bright and dark deposits in areas that are sufficiently cold to trap ice according to thermal models (Paige et al., 2013; Neumann et al., 2013). The bright deposits were identified as exposed surface ice, while the darker deposits were suggested to be ice buried under a space weathered thermal lag (Paige et al., 2013; Chabot et al., 2014; Delitsky et al., 2017). PSRs within craters were imaged by the Mercury Dual Imaging System (MDIS) and were found to contain similar features with distinctive reflectance properties and sharp boundaries (Chabot et al., 2014). If these features are ice deposits, they could only outlast erosion if they were relatively young or continuously renewed at a rate that dominates the gardening rate (Chabot et al., 2016).

Lately, it was hypothesized that ice may persist in micro cold-traps that form in PSRs cast by craters and random small scale topographic features (Hayne and Aharonson, 2015). In this case, the term "micro" does not mean "of microscopic size"; instead, it refers to the Greek word "$\mu\iota\kappa\rho\acute{o}\varsigma$" (mikrós), "small". More recently, Deutsch et al. (2017b) found evidence for small ice deposits inside cold-traps on scales $\sim$ 1 km. Here we show evidence for ice trapped inside much smaller micro cold-traps on scales 1-10 m. We use MLA data to find the surface darkening occurs not only inside the larger, resolved features, but also in the inter-crater terrain. We interpret this as evidence for water ice micro cold-traps buried under a darkened thermal lag. We fit a model to the reflectance data in order to constrain the

lateral size of these cold-traps and their maximum possible thickness. Finally, we compare our findings with recent estimates for the volatiles erosion rate in order to constrain the origin and age of the ice trapped within them.

4.2 Evidence for Ice Inside Micro Cold-Traps

4.2.1 Measuring Mercury's Surface Darkening

The surface darkening observed on Mercury's pole by Neumann et al. (2013) and Paige et al. (2013) is not unique to large impact craters. Inspection of the stretched MLA reflectance map (Figure 4.1a) shows that the inter-crater terrain darkens in high latitudes as well (Neumann et al., 2017; Rubanenko et al., 2017a). Similar inspection of the radar brightness map (Harmon et al., 2011) (Figure 4.1b) shows small scale radar-bright features in between the larger resolved cold-traps, indicative of small discontinuous ice deposits. However, the radar map does not show a latitudinal brightening that matches the latitudinal darkening observed in the reflectance map. While most the signal was found to spatially correlate with the locations of small craters (Chabot et al., 2012; Deutsch et al., 2016), some of it may still be associated with unresolved features in the inter-crater terrain.

Due to the lack of MLA data in the south pole, our analysis is restricted to the north pole of Mercury. To measure the decrease in surface reflectance due to the sub-pixel darkening (below the resolution of the binned MLA dataset), we first collect MLA reflectance data gathered between 2011-2015 in bins of 250 m. Then, we discard data below latitude 70°, anomalous measurements (greater than unity) and those obtained at emission angles $> 10°$. The obtained reflectance distribution, shown in Figure 4.2, is bimodal with an extended tail. The right and left modes correspond to the mean reflectance of the bare regolith and the mean reflectance of slopes covered by a darkened deposit, respectively. The extended tail was suggested to be exposed surface ice (Paige et al., 2013).

Next, we remove all the larger dark features, such as those inside craters: we begin by

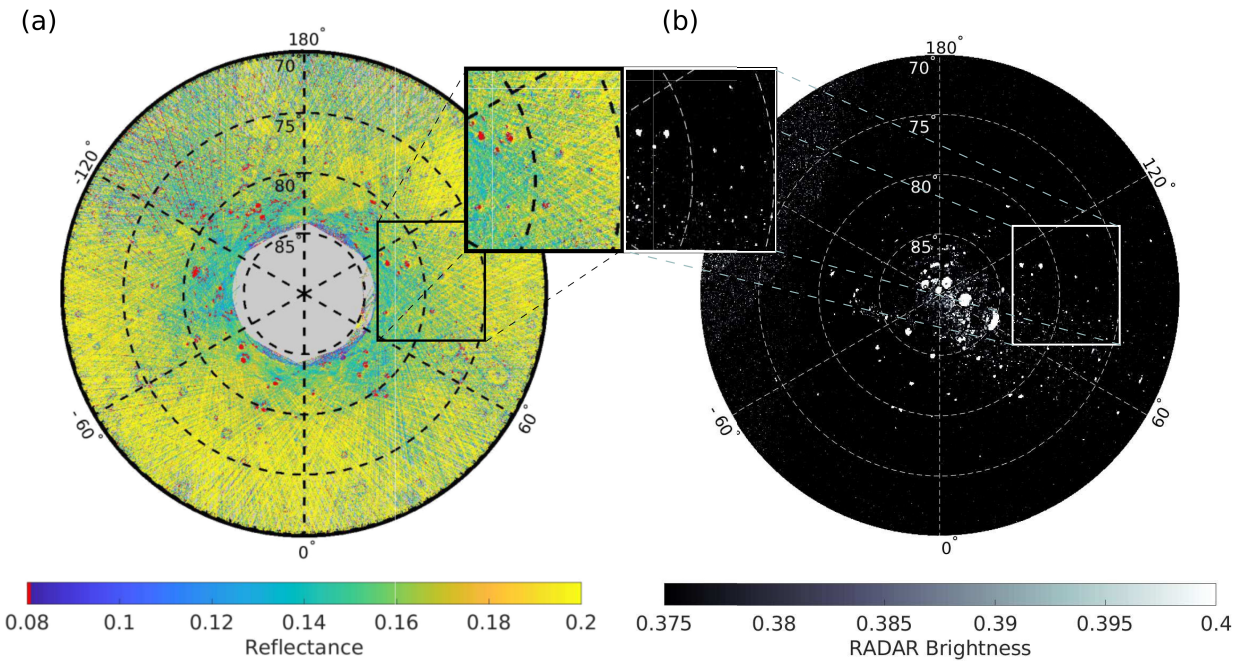

Figure 4.1: a. The north pole MLA reflectance map in polar stereographic projection, binned at 250 m px^{-1}. Dark deposits, which are postulated to contain ice trapped under a space weathered thermal lag, appear both inside craters and in the inter-crater terrain. In order to measure the sub-pixel darkening, we remove spots with reflectance < 0.08 and size > 1 pixels (marked in red). Gray pixels indicate missing or discarded data. b. The north pole stretched radar brightness map in polar stereographic projection, adapted from Figure 5 in Harmon et al. (2011) and rebinned at 1 km^2. Radar bright regions, which are indicative of pure, thick ice, are apparent both in resolved cold-traps within larger craters but also in smaller craters (Harmon et al., 2011; Deutsch et al., 2016).

reducing the reflectance map into a binary image with threshold 0.08, and remove binary spots larger than 1 pixel. The choice of 0.08 is reasonable considering it separates the two modes of the reflectance distribution shown in Figure 4.2.

Mercury is found at a 3/2 spin-orbit resonance that causes roughly half of its polar region to receive more insolation than the other half (Soter and Ulrichs, 1967). These two distinct longitude ranges are sometimes termed the "cold pole" ($\sim 60°\text{W} - 120°\text{W}$ and $\sim 240°\text{W} -$

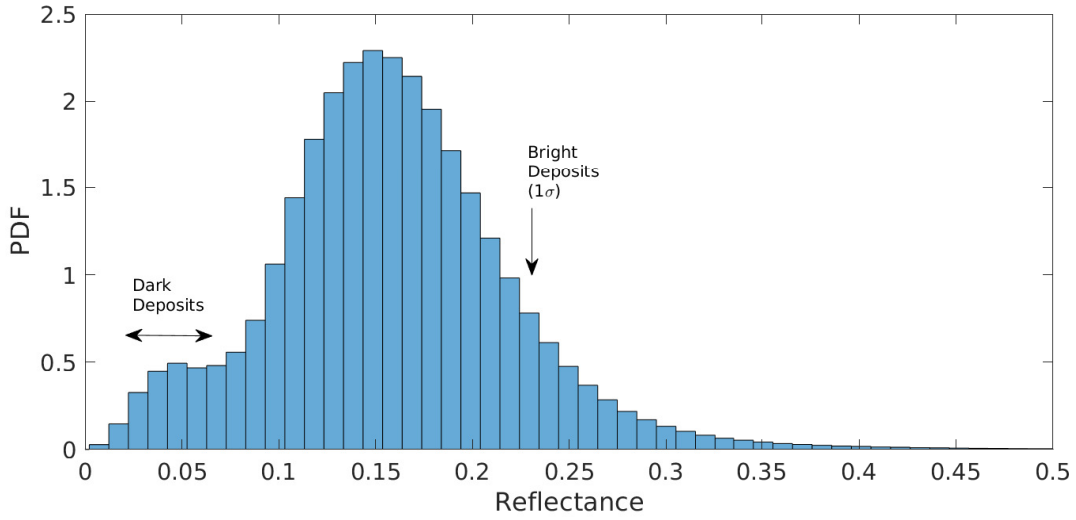

Figure 4.2: The MLA reflectance distribution of the north pole of Mercury (above latitude 70°) binned at 250 m^2. The distribution is bimodal with an extended tail; the left mode corresponds to the mean reflectance of the dark surface deposits. The right mode approximately corresponds to the mean reflectance of the surface. The extended tail is thought to represent exposed, and therefore bright, water ice deposits. We use these two representative values (marked by arrows) to model the surface reflectance. The uncertainty we consider when choosing the reflectance of the dark deposits is shown by the two-sided arrow on the left.

300°W) and the "warm pole" ($\sim 120°\text{W} - 240°\text{W}$ and $\sim 300°\text{W} - 60°\text{W}$), respectively (Paige et al., 1992). We calculate the zonal mean of the reflectance data in these two longitude ranges (yellow-black and green-black dots, Figure 4.3). Due to MESSENGER's non-polar orbit, the most reliable MLA measurements were gathered between latitudes $75° - 85°$. This region is marked in the figure by the dashed vertical lines and filled circles.

We find the zonally averaged reflectance decreases from ~ 0.18 in lower latitudes (75°) to ~ 0.15 near the edge of the most reliable data region (85°). The reflectance in the cold pole decreases more rapidly than the reflectance in the warm pole. Near the pole (above latitude 85°) the surface reflectance sharply increases, possibly due to the presence of large impact craters such as Prokofiev, which were found to contain many high reflectance deposits

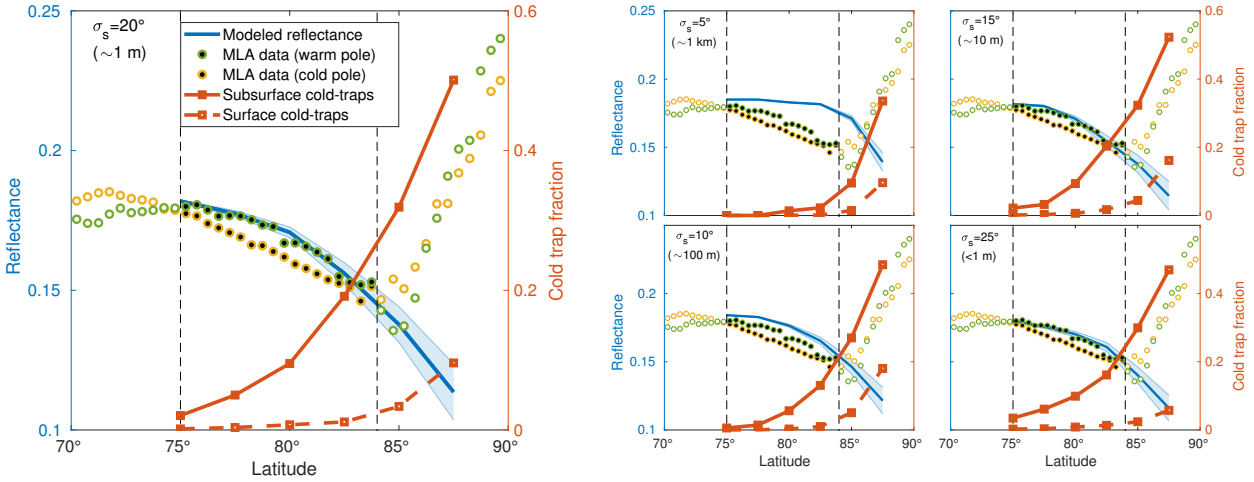

Figure 4.3: The zonally averaged reflectance (black circles) binned at 250 m px^{-1}, large craters removed, along with the modeled reflectance of random surfaces with different σ_s (blue), and the corresponding modeled surface and subsurface cold-trap area fractions (red). The green and yellow circles indicate Mercury's "warm pole" and "cold pole", respectively. The reflectance of the cold pole is lower than that of the warm pole, possibly indicating a greater fraction of ice buried under a thermal lag. The measured decrease in reflectance matches that of a random rough surface with $\sigma_s = 15 - 20°$, corresponding to cold-traps on lateral scales < 10 m. The shaded envelope indicates the uncertainty in the value we chose to represent the reflectance of the dark slopes. The dashed vertical lines mark the region of most reliable data, also emphasized by the filled circles. We highlight the $\sigma_s = 20°$ panel as it described the surface that best fits the observed darkening.

(Neumann et al., 2013).

4.2.2 Possible Reasons for Mercury's Surface Darkening

Paige et al. (2013) postulated the MLA dark deposit found in many polar craters is a weathered carbonaceous thermal lag covering a thick layer of ice. Using a thermal model, they showed a spatial correlation between areas in which ice is stable in the subsurface and areas that are MLA dark. Additional analysis conducted by Neumann et al. (2013) and

Chabot et al. (2014) showed a similar spatial correlation between these dark deposits and the boundaries of permanent shadows.

Chemical and physical models explain how these polar deposits accumulate and grow dark (Paige et al., 2013; Delitsky et al., 2017). At first, comets or other impactors deposit volatile raw materials such as water, methane, carbon dioxide and ammonia on the surface. These volatiles travel to the pole and become cold-trapped inside PSRs (Schorghofer, 2015). Then, magnetic cusps in Mercury's magnetic field focus energetic particles onto these ices along with galactic cosmic rays and Lyα radiation. This radiation can initiate chemical processes that would eventually create heavier less volatile complex organic C-H-N-O-S molecules that would cover the ices and protect them from sublimation or destruction (Delitsky et al., 2017).

Here we suggest the surface darkening we measure between latitudes $75° - 85°$ is evidence for ice in micro cold-traps: ice deposits trapped in PSRs cast by sub-pixel topography and buried under the same darkened thermal lag that covers the larger cold-traps. This idea is supported by the difference in reflectance between the cold and warm poles. The cold pole has a greater cold-trap area fraction than the warm pole as it receives less insolation and has a higher PSR fraction due to the smaller angular size of the Sun in the sky. The higher PSR fraction increases the area fraction of cold-traps that are buried under a thermal lag, which leads to a lower surface reflectance. Thermal models show bright surface ice is not prevalent on Mercury below latitude 85° due to the high amount of scattered and emitted radiation, and thus has little effect on the overall surface reflectance (Paige et al., 2014).

Other possible explanations for this surface darkening could be Mercury's higher surface carbon content (Syal et al., 2015), geologic features related to Mercury's north polar smooth planes (Neumann et al., 2017) or the low reflectance materials (LRM) found in lower latitudes (Robinson et al., 2008). However, these alternative explanations do not account for the excellent spatial correlation with PSRs and areas in which water ice is cold-trapped under the surface (Paige et al., 2013; Chabot et al., 2014).

Next, we constrain the lateral scale of these cold-traps by modeling their reflectance using artificial random topography.

4.2.3 Modeling the Micro Cold-Trap Area Fraction

A common way to model rough topography on airless bodies is to use random Gaussian surfaces (e.g. Hagfors, 1964; Smith, 1967a; Jamsa et al., 1993; Davidsson and Rickman, 2014; Bandfield et al., 2015; Rubanenko and Aharonson, 2017). This artificial realization has a Gaussian slope distribution and a power-law power spectrum. The 1-D slope distribution of realistic airless topography sometimes deviates from this idealized model due to the presence of craters. However, the calculated shadow and temperature distributions and the resulting cold-trap fractions of rough surface resemble those observed on the Moon (Smith, 1967a; Bandfield et al., 2015; Rubanenko and Aharonson, 2017). To verify this is also true for Mercury, we compared the modeled north pole cold-trap fraction using real topography to that of a rough random surface with the same RMS slope $\sigma_s \sim 7°$. The cold-trap area fraction modeled by Paige et al. (2013) is 0.068, in good agreement with the one calculated by our model, 0.07.

The exponent of the surface power spectrum describes the dependence of the roughness on the lateral scale. The value of this exponent was recently measured on Mercury to be $\beta \sim 2.9$ for lateral scales ~ 0.5 km, larger than some of the scales we model here (Susorney et al., 2017). However, with no better measurement, we choose to adopt this value. We verified our calculated shadow and cold-trap fractions are largely insensitive to that choice by modeling surfaces with $\beta = 1.9$ and $\beta = 3.9$. The surfaces we generate are composed of $N = 100 \times 100$ facets. This choice of the surface size is a compromise between the model running time, which is squared in N, and the error in the calculated PSR area fraction, which is $\sim 3\%$ (compared to a surface with $N = 1000 \times 1000$ pixels). A more detailed description of the model and the generation of rough random surfaces is provided in Rubanenko and Aharonson (2017).

Accurate measurements of the surface roughness are limited to the instrument resolution which on Mercury is $\sim$ 250 m - much larger than our scale of interest. In the absence of better data for Mercury, we adopt measurements conducted on the Moon by the lunar

reconnaissance orbiter laser altimeter (LRO LOLA), noting Mercury's surface roughness was found to be slightly lower at lateral scales > 500 m (Fa et al., 2016). However, as will be explained later, this does not significantly affect our conclusions.

On the Moon, higher σ_s corresponds to smaller lateral scales; the distribution of slopes on scales $\sim 1-10$ km has $\sigma_s \sim 5°$, while the distribution of slopes on scales $\sim 1-100$ m has a higher $\sigma_s \sim 20° - 10°$ (Rosenburg et al., 2011b, 2015; Bandfield et al., 2015, and references therein). We show this dependence in Figure 4.4 based on measurements obtained by LOLA and previous analyses (Helfenstein and Shepard, 1999; Bandfield et al., 2015). To measure the slope distribution at lateral scales 10 m, 120 m and 240 m we calculate the 2-D gradient of the LOLA polar (above latitude $\pm 75°$) map at the appropriate baseline. To measure σ_s at higher lateral scales we fit a least-squares plane to square groups of pixels on the 120 m map. We use groups of sizes 8×8 and 80×80 pixels for lateral scales 960 m and 9600 m, respectively. Finally, we calculate the RMS of the slope distribution of all planes.

Higher σ_s affects the cold-trap area fraction by simultaneously increasing the PSR area fraction and the amount of reflected and thermally emitted radiation from nearby illuminated, warm slopes. Therefore, higher surface roughness does not necessarily translate into a higher cold-trap area fraction (Rubanenko and Aharonson, 2017). On Mercury this effect is amplified compared to the Moon due to the higher temperature of illuminated slopes and the consequent higher reflected visible and emitted IR flux. Next, we use this link between the surface roughness and the cold-trap area fraction to constrain the lateral scale of micro cold-traps on Mercury.

We calculate the surface and subsurface temperatures accounting for insolation, scattering, thermal emission and subsurface conduction. We employ the same model used by Rubanenko and Aharonson (2017), but introduce two improvements: a finite Sun instead of a point-source Sun and temperature dependent thermal parameters. We assume a bolometric albedo of 0.08 (Domingue et al., 2011) and an emissivity of 0.95. Previous works considered slightly lower or higher values (Soter and Ulrichs, 1967; Veverka et al., 1988; Paige et al., 1992; Emery et al., 1998) but those do not significantly affect our results.

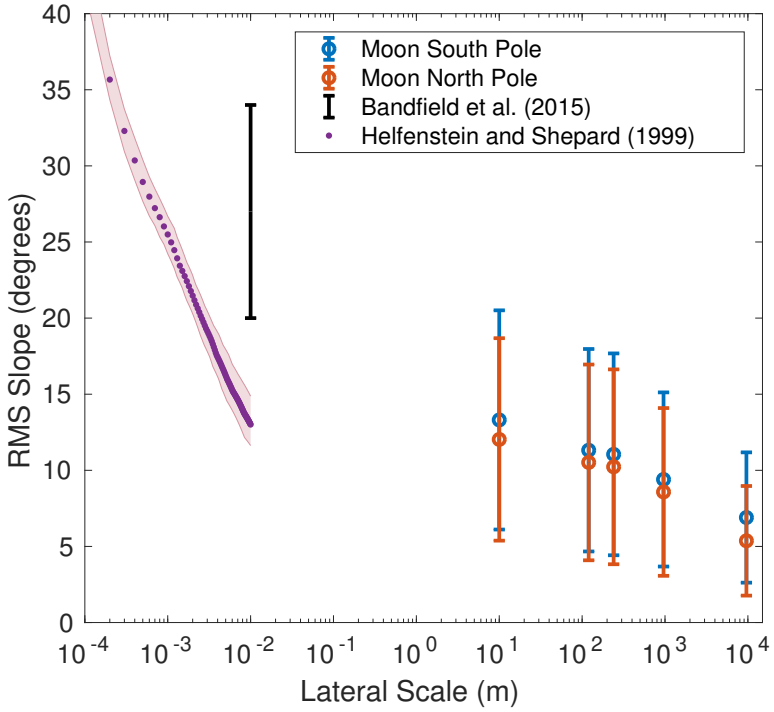

Figure 4.4: The surface roughness (indicated by the RMS slope) increases with decreasing scale on the Moon. The red and blue dots, which show LOLA data on scales ¿ 10 m, are provided along with the standard deviation. Roughness measurements at smaller scales were obtained by Helfenstein and Shepard (1999) and Bandfield et al. (2015).

To calculate the subsurface temperatures up to a depth of 1 m we use a modified version of the 1-D heat diffusion model described in Rubanenko and Aharonson (2017); we use a temperature dependent thermal conductivity (of order $k \sim 10^{-2}$ W m^{-1}K^{-1}) and specific heat capacity (of order $c \sim 300$ J kg^{-1} K^{-1}), as prescribed in the appendix of Hayne et al. (2017). For temperatures > 400 K we linearly extrapolate c and k. The error introduced by this extrapolation should not significantly affect our results as only illuminated facets, which are anyway found in radiative equilibrium, reach these temperatures (Bandfield et al., 2015). Finally, we assume a lunar-like power law subsurface density profile that increases from a value of 1100 kg m^{-3} at the surface to a value of 1800 kg m^{-3} at depth (Hayne et al., 2017). The resulting thermal skin depth is of the order of a few decimeters.

As explained in Rubanenko and Aharonson (2017), we find the surface cold-trap area fraction using the well-known relation between the maximum sublimation rate of ice into vacuum $\dot{E}_{max}$ and the maximum surface temperature T_{max},

$$\dot{E}_{max} = \frac{P_v}{\sqrt{2\pi k_B \mu T_{max}}} \tag{4.1}$$

where P_v is the equilibrium vapor pressure, $k_B \approx 1.38 \times 10^{-23}$ m^2 kg s^{-2} K^{-1} is the Boltzmann constant, μ is the mass of a water molecule (Watson et al., 1961; Schorghofer and Taylor, 2007). Exposed water ice sublimates from cold-traps at any temperature greater than the absolute zero, but for temperatures < 120 K the ice loss rate is likely dominated by impact gardening and space weathering and is ~ 1 m Ga^{-1} (Gault et al., 1974; Lanzerotti et al., 1981; Morgan and Shemansky, 1991; Schorghofer and Taylor, 2007). To find the subsurface cold-traps area fraction we use a similar model that relates $\dot{E}$, the surface sublimation rate, ζ, the burial depth and J, the ice loss rate in kg m^{-2}s^{-1} (Schorghofer and Taylor, 2007),

$$J = \frac{\mu \ell \dot{E}}{2\zeta} \tag{4.2}$$

where $\ell = 75 \times 10^{-6}$ m is the typical regolith grain size (McKay et al., 1974; Heiken et al., 1991). We find the surface (subsurface) cold-trap area fraction by calculating the fraction of facets whose surface (subsurface) sublimation rates < 1 m Ga^{-1}. Finally, to obtain a statistically significant result, we average five different random surfaces for every σ_s and latitude.

The maximum annual temperature distribution of an airless surface is affected by the planet's obliquity and eccentricity. Here we neglect Mercury's obliquity which is of order a few arcminutes (Yseboodt and Margot, 2006), and model the thermal conditions at its warm pole by fixing the planet's solar distance at perihelion, 0.307 AU. In Figure 4.3 we show the surface and subsurface cold-trap area fractions for surfaces with different σ_s (red lines).

4.2.4 Modeling the Surface Reflectance

To model the latitudinal change in reflectance we use values derived from the distribution shown in Figure 4.2 and the cold-trap area fractions calculated above. As demonstrated in Figure 4.5, we assign subsurface and surface cold-traps with a reflectance of 0.04 (the left mode) and 0.23 (1σ above the mean) and non-cold-traps with a reflectance of 0.18 (the mean between latitudes $70° - 75°$). The total reflectance of the surface is obtained by calculating the weighted average of the reflectance of the slopes composing it. Results are shown Figure 4.3. Our choice for the reflectance value of the dark slopes is based on the distribution appearing in Figure 4.2. For robustness, we consider an uncertainty that is equal to the width of the left mode of this distribution, indicated by the blue envelope.

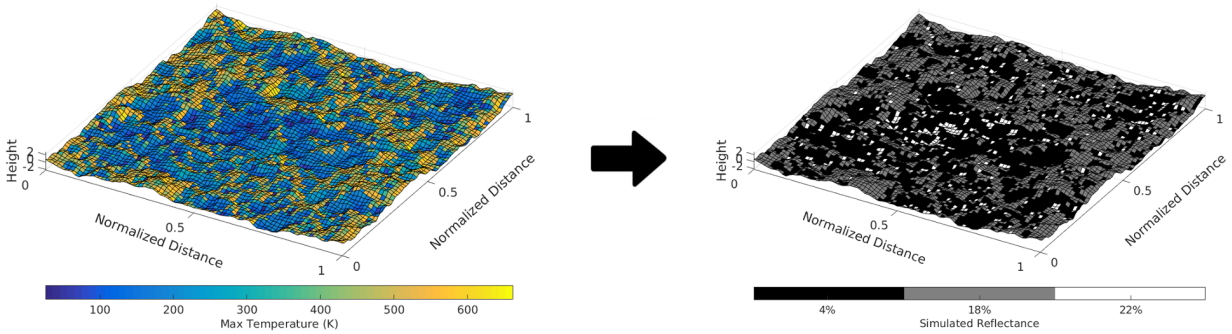

Figure 4.5: A demonstration of our reflectance model. First, we calculate the maximum diurnal temperature distribution of the rough surface (left). Then, subsurface cold-traps are assigned with a reflectance of 0.04, corresponding to the left mode in the distribution shown in Figure 4.2. Surface cold-traps are assigned with a value of 0.23, corresponding to 1 σ above the right mode of the distribution. Non-cold-traps are assigned with a value of 0.18, the mean reflectance between latitudes $70° - 75°$. The total reflectance of the surface is a weighted average of the reflectance of the facets composing it. To obtain a statistically significant result, we average five different random surfaces for each latitude and each roughness.

The modeled reflectance of random surfaces with $\sigma_s = 20°$ (slope-scale $\lesssim$ 1 m) best

fits the zonally averaged MLA reflectance in the warm pole (green-black circles). Surfaces with $\sigma_s < 15^\circ$ (slope-scale > 100 m) do not fit the observed reflectance due to their lower subsurface cold-trap area fraction. Above we noted measurements at larger lateral scales indicate the surface roughness on Mercury may be slightly lower than that of the Moon (Fa et al., 2016). As roughness increases with decreasing lateral scale, this would only act to decrease the scale of the cold-traps we find here and thus should not affect our conclusions.

The fraction of the surface that can cold-trap a volatile species depends not only on its temperature, but also on the thermochemical properties of the molecule (Watson et al., 1961). Above we found water ice cold-traps can explain the surface darkening observed on Mercury. We repeat this calculation for other prevalent volatiles found in comets; we derive their cold-trap area fraction and use it to model the surface reflectance, as we did above. As an example, we show in Figure 4.6 results for a rough random surface with $\sigma_s = 20^\circ$ (lateral scale ~ 1 m). We find that volatile species other than water (see Table 4.1) cannot reproduce the observed darkening. While some complex molecules such as methanol nearly fit the measurements, they are much less abundant in comets compared to water ice (Zhang and Paige, 2009).

We estimate the total area fraction occupied by micro cold-traps in the north polar region by linearly extrapolating and integrating the red lines in Figure 4.3 from latitude 75° to the pole. Assuming the scale of all micro cold-traps is ~ 10 m ($\sigma_s = 15^\circ$), the total area of surface cold-traps is 2.98×10^4 km^2, $\sim 2.33\%$ of the polar region. Similarly, if the scale of all micro cold-traps was ~ 1 m ($\sigma_s = 20^\circ$), their total area would be 2.13×10^4 km^2, $\sim 1.66\%$ of the polar region. This is about 20% of the area fraction occupied by the larger, resolved cold-traps (Paige et al., 2013).

Since we do not model lateral heat conduction, our results are only valid for lateral scales larger than the thermal skin depth (Bandfield et al., 2015). Therefore, although we found cold-traps on scales $1 - 10$ m can best explain the observed reflectance, we cannot rule out the existence of smaller cold-traps. Additionally, we note it is possible these micro cold-traps do not contain ice at all as it may have already sublimated, leaving behind the thermal lag

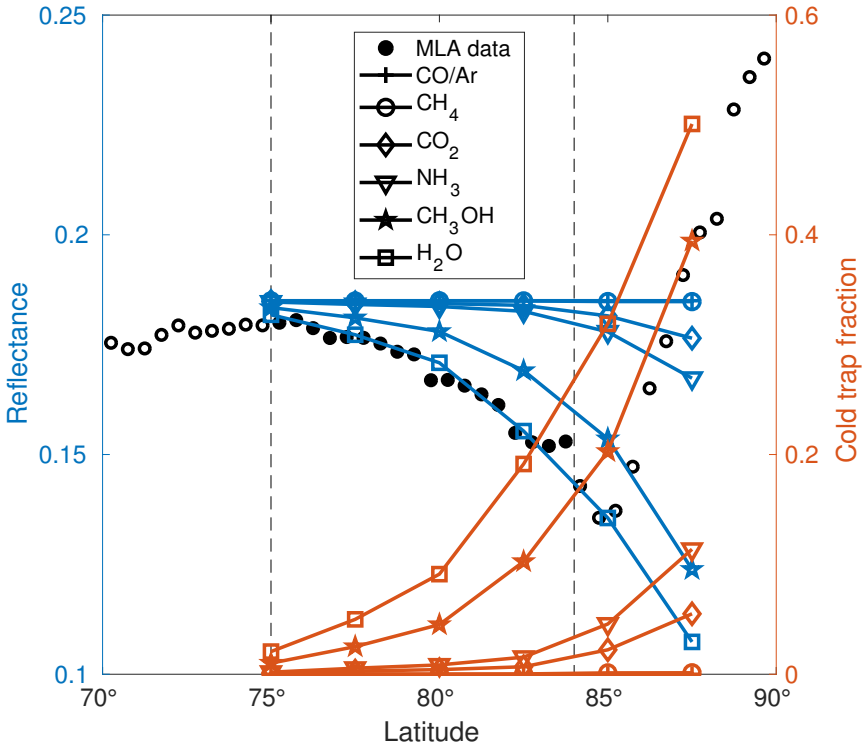

Figure 4.6: The MLA reflectance data for the warm pole along with the subsurface cold-trap area fractions and the modeled decrease in reflectance for the most abundant volatiles found in comets (Zhang and Paige, 2009). We find the presence of water ice cold-traps best explains the zonally mean surface darkening. The dashed vertical lines mark the region of most reliable data, as before. Argon and CO are represented by the same line, as their cold-trap area fractions are zero.

that once covered it.

4.3 Accumulation and Dissipation of Ice in Micro Cold-Traps

After being delivered to the surface, water molecules on airless bodies travel in ballistic hops whose length depends on their thermal energy (Watson et al., 1961). For Mercury, the mean hop length is $\sim 100 - 200$ km (Schorghofer, 2015) - comparable to the scale of the largest

Compound	Q (kJ mol^{-1})	P_t (kPa)	T_t (K)
CH_4	$9.7^{(1)}$	$11.69^{(1)}$	$90.67^{(1)}$
NH_3	$30.96^{(2)}$	$6.08^{(3)}$	$195.48^{(3)}$
H_2O	$51.06^{(2)}$	$0.61^{(4)}$	$273.16^{(4)}$
CO	$7.6^{(1)}$	$15.30^{(3)}$	$68.09^{(3)}$
CH_3OH	$44.2^{(5)}$	$1.08 \times 10^{-4(6)}$	$175.6^{(6)}$
Ar	$7.78^{(7)}$	$68.9^{(7)}$	$83.80^{(7)}$
CO_2	$27.2^{(8)}$	$518^{(9)}$	$216.58^{(9)}$

Table 4.1: The enthalpy of sublimation Q along with the triple point pressure P_t and temperature T_t used to calculate the cold-trap area fractions for the volatiles shown in Figure 4.6. References: (1) Stephenson (2012), (2) Dell and Beebe (1955), (3) Staveley et al. (1981), (4) Sato et al. (1991), (5) Lucas et al. (2005), (6) Cheng (1994), (7) Ferreira and Lobo (2008), (8) Bryson III et al. (1974), (9) Chickos and Jr. (2002).

cold-traps (*e.g* in Prokofiev Crater). Since the residence time of trapped molecules is much longer than the duration of the hops, ice precipitation into cold-traps can be thought of as rain falling into buckets; the probability that a molecule would become trapped in a cold-trap depends on its surface area alone. Additionally, due to the extremely low sublimation rates, volatile redistribution is minimal and all cold-traps should be filled approximately to the same height. Consequently, the accumulation and dissipation of ice inside cold-traps can be thought of as a source-sink problem (per unit area). Constraining the ice thickness inside the smallest cold-traps on Mercury and comparing it to the modeled erosion rate could help us estimate its deposition time and delivery method.

4.3.1 Constraining the Depth of Ice in Micro Cold-Traps

The potential ice thickness inside a cold-trap is limited by the depth of the permanent shadow it occupies. If the temperature of the cold-trap is sufficiently low, ice may accumulate

inside it until it exceeds the *permanent shadow volume* (PSV) and becomes exposed to solar illumination. However, ice accumulation may cease even before that stage. Significant ice deposits may alter the topography and change the amount of scattered and emitted radiation the cold-trap receives. Consequently, the temperature of the ice may increase, inhibiting growth, or decrease, encouraging it. Next, we constrain the maximum thickness of ice trapped in surface micro cold-traps using the depth of the PSVs they cast.

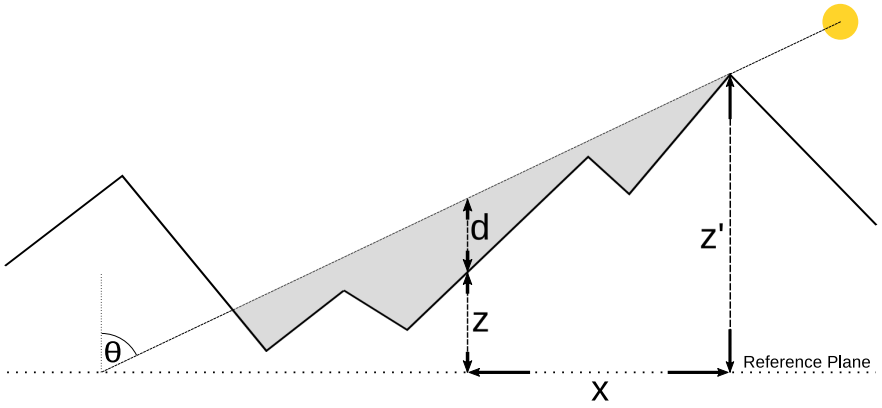

Figure 4.7: Our shadow depth model which we use to constrain the ice depth cast by the random topography. In this figure, θ is the solar incidence angle, d is the transient shadow depth, z is the height of the shadowed point and z' is the height of the point casting the shadow above the reference plane.

To calculate the depth of the PSV cast by the sub-resolution topography we employ our 3-D illumination model used above. First, we find the instantaneous shadow depth: the vertical distance between the surface and the shadow that covers it. The instantaneous shadow depth d at a distance x from the point casting the shadow is,

$$d = z' - z - x \cot \theta \tag{4.3}$$

where θ is the incidence angle, z' is the height of the point casting the shadow (relative to the reference plane) and z is the point of interest (Figure 4.7). If more than one point in the way to the Sun casts a shadow on the point of interest, we use the deepest shadow. To calculate the depth of the permanent shadow, we find the temporal minimum of the instantaneous

shadow depth at every point on the surface. As this calculation is less computationally intensive than the full temperature calculation, we are able to increase the model accuracy by using topographies of size 250×250 facets. Relative to surfaces with size $N = 1000 \times 1000$ facets, our model underestimates the permanent shadow area fraction by $\sim 1.5\%$. As before, we obtain a statistically significant result by averaging the PSV fractions of five different surfaces.

The cumulative distribution of the PSV depth is shown in Figure 4.8 for the two roughness values that match Mercury's surface darkening, $\sigma_s = 15^\circ, 20^\circ$, and latitudes 80° and 85°. We find that for surfaces with $\sigma_s = 15^\circ$ and $\sigma_s = 20^\circ$ (lateral scales $\sim 1 - 10$ m) the median PSV depth is ~ 1 m and ~ 25 cm, respectively. This result explains the absence of a strong radar reflectance signal in between craters, that requires the deposit to be at least a few meters thick (Harmon et al., 2001). Next we discuss several ways in which erosion can affect accumulated surface ice.

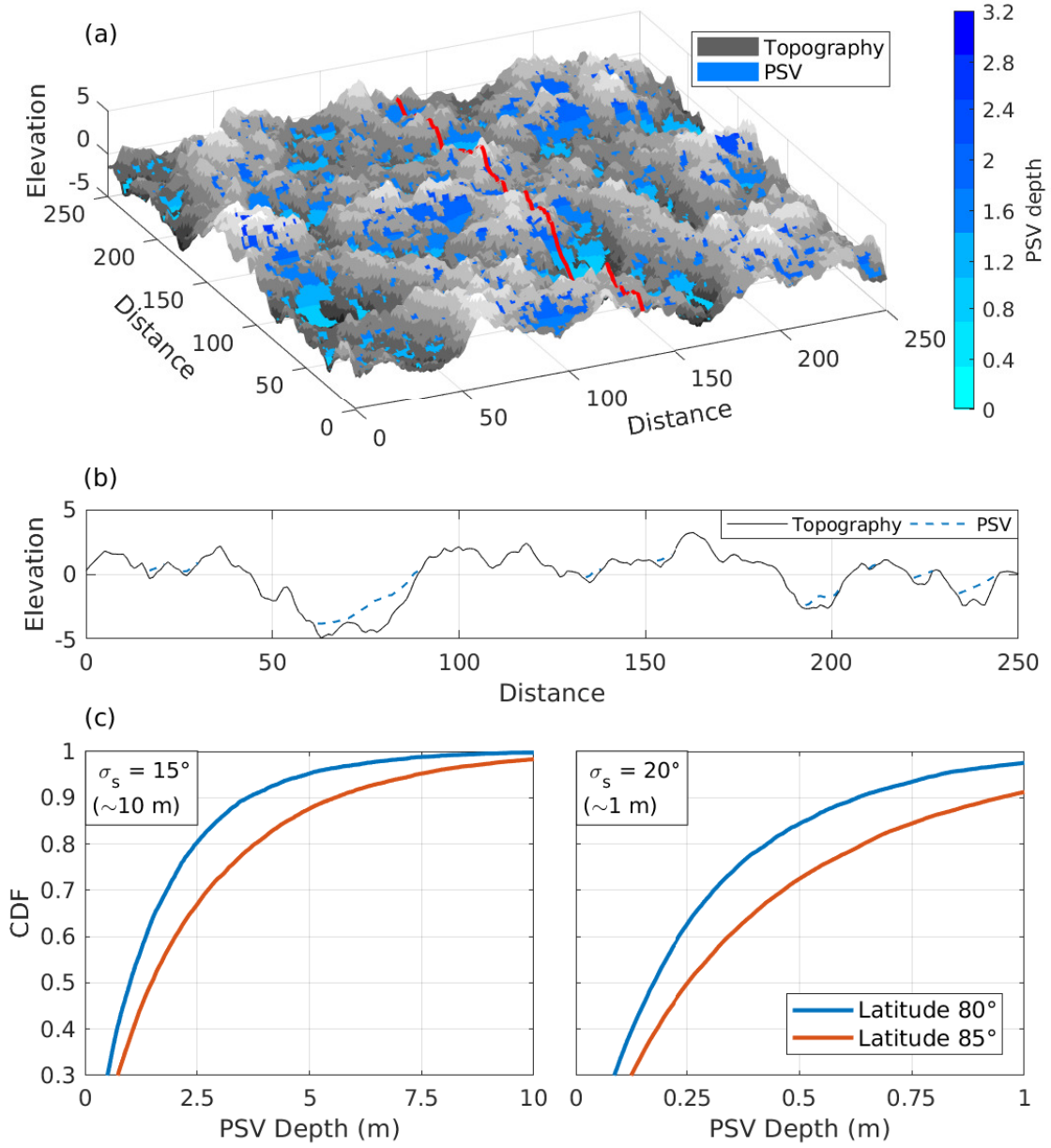

Figure 4.8: (a) The permanently shadowed volume (PSV) depth superimposed on a random topography with $\sigma_s = 20°$ at latitude 85°. The color bar on the right indicates the depth of the PSV above the surface, which is an upper limit for the thickness of the ice trapped within it. (b) A cross section (shown in red) of the topography. The PSV depth above the topography is plotted as the dashed blue line. (c) The cumulative distribution function of the PSV depth, showing most of the ice must be trapped in a layer < 1 m for surfaces with $\sigma_s = 15°$ (scale ~ 10 m) or < 25 cm for surfaces with $\sigma_s = 20°$ (scale ~ 1 m).

4.3.2 Sublimation due to Heat Delivered by Impacts

An impact can destroy cold-trapped ice in two ways: it may sublimate it by heating the surface or it may mechanically disperse it into a region in which it will become unstable. Next we show the former is less important than the latter for ice trapped inside micro cold-traps.

Impacts create a shock wave that compresses the regolith and heats it (Melosh, 1989). The mass loss rate J_i due to surface heating by impactors can be estimated using the simple relation,

$$J_i = \frac{E(D)\alpha}{L_{sub}} \tag{4.4}$$

where $E(D)$ is the cumulative energy delivered to the surface by meteorites of size $< D$, L_{sub} is the latent heat for sublimation, α is the heat transfer coefficient taken here to be unity.

Brown et al. (2002) used satellite records to measure $E(D)$ for Earth using observations on detonating bollides in the atmosphere. They found the cumulative number N of bollides colliding with Earth with energy E or greater is,

$$\log N = a_0 + b_0 \log E \tag{4.5}$$

where $a_0 = 0.5677 \pm 0.015$ and $b_0 = 0.90 \pm 0.03$. For a given bollide size, the energy delivered to Earth per unit area is,

$$E(D) = \frac{N(E)dE}{4\pi R_E^2} \tag{4.6}$$

where R_E is Earth's radius. To obtain a rough estimate of the cumulative energy delivered to Mercury by meteorite impacts, we use the $E(D)$ measured for Earth, correcting for Mercury's higher mean impact velocity, ~ 40 km s^{-1} (Le Feuvre and Wieczorek, 2011). We find the energy delivered by bodies with diameters < 1 m will sublimate ice at a rate of ~ 1 mm Ga^{-1} - much lower than the mechanical gardening rate or the sublimation rate at 120 K, which is ~ 1 m Ga^{-1} (Watson et al., 1961; Schorghofer and Taylor, 2007).

4.3.3 Erosion due to Mechanical Impact Gardening

Compared to sublimation due to impact delivered heat, mechanical gardening is a more significant erosive process. Recently, Speyerer et al. (2016) found that the impact turnover rate of the lunar surface may be much higher than previously thought due to the contribution of secondaries. Observations of rayed craters on Mercury have suggested secondaries may play an even greater role compared to the Moon (Neish et al., 2013). While previous models have shown the time in which the top few decimeters are overturned due to gardening is at least ~ 1 Ga (Gault et al., 1974; Hurley et al., 2012), more recent models for both the Moon and Mercury (Costello et al., 2017a,b) find a much higher rate of a few decimeters in 10 Ma.

While impact gardening does not necessarily accelerate sublimation, it causes lateral and vertical regolith turnover. With time this turnover may erode the ice, if it is exposed, or the thermal lag that covers it. Above we showed the modeled surface darkening matches the MLA observations, indicating this thermal lag, which is most likely about a decimeter thick (Paige et al., 2013), is more or less intact. If we take into account the overturn models mentioned above, we see a significant fraction of this thermal lag should have been eroded in less than 100 Ma (according to the more conservative, traditional models) or in < 10 Ma (according to the more recent models). Other models that include lateral mixing predict an even shorter erosion time scale (Hurley et al., 2012). This indicates the ice on Mercury was either recently deposited or that its accumulation rate is much greater than its dissipation rate. This observation agrees with previously obtained images that showed the dark deposits have sharp, unperturbed boundaries (Chabot et al., 2014, 2016).

4.3.4 Sublimation Due to Space Weathering

The loss rate of exposed ice consists of temperature-dependent sublimation and temperature-independent space weathering (Schorghofer and Taylor, 2007). The latter occurs mainly due to gardening, solar-wind sputtering and Lyα radiation from the local interstellar medium (LISM), estimated to be a few decimeters per Ga (Lanzerotti et al., 1981; Morgan and She-

mansky, 1991; Westley et al., 1995). While ice deposits in deep craters (depth/diameter ratio ~ 0.2) might be less affected by sputtering (Feldman et al., 2001), micro cold-traps in the random topography have a generally higher sky visibility (Rubanenko and Aharonson, 2017). Additionally, while solar sputtering may be a net hydrogen source, significant quantities of surface ice, like on Mercury, should be more affected by sputtering compared to an admixture of ice and soil Crider and Vondrak (2003).

4.4 Discussion

Ice persists inside cold-traps formed within permanent shadows on the north pole of Mercury (Harmon et al., 2001; Neumann et al., 2013; Chabot et al., 2014; Deutsch et al., 2017b). Many of these cold-traps were found to be covered by a dark deposit thought to be a space weathered carbonaceous thermal lag (Paige et al., 2013). Here we show this surface darkening occurs also outside of the larger, resolved features, and find it can be explained by water ice trapped under a thermal lag in micro cold-traps of lateral scales $\sim 1 - 10$ m. This result is consistent with the model developed by Delitsky et al. (2017), that found both water and simple organics are necessary in order to form the darkened thermal lag. By describing the sub-pixel topography using random Gaussian surfaces, we find the median depth of the permanent shadows harboring these micro cold-traps, which limits the amount of ice accumulated in them, to be < 1 m. This explains the latitudinal sub-pixel darkening, which does not require thick ice (Paige et al., 2013), and the absence of a matching continuous sub-pixel radar reflectance signal, which requires an ice layer at least few meters thick (Figure 4.1).

To first order, four factors affect the purity of an ice deposit and the darkened thermal lag covering it: volatile accumulation, volatile destruction, vertical regolith turnover and lateral regolith mixing. By considering these factors we can put further constraints on the origin and age of the ice inside micro cold-traps. We discuss two possible scenarios that may explain the presence of ice in these shallow micro cold-traps: a steady gain which is greater

than the steady loss or an episodic deposition (primordial or recent) followed by a steady loss (Table 4.2).

Mechanism	Pristine Boundaries (Chabot et al., 2014)	Micro Cold-Traps (this work)	Radar signal (Harmon et al., 2001)	Dark Thermal Lag (Paige et al., 2013)
Primordial origin	x	x	✓	✓
Steady accumulation	✓	x	x	Only micrometeorites
Recent comet impact	✓	✓	✓	✓

Table 4.2: Three ice accumulation mechanisms explaining the origin of ice in micro cold-traps on Mercury, and the evidence bolstering/refuting them.

In the first scenario, the volatiles influx is greater than the outflux and Mercury's ice budget is dominated by slow, continuous delivery. Among the possible sources we consider solar wind implantation, which was shown to be an important source on the Moon (Crider and Vondrak, 2000; Liu et al., 2012), and a constant flux of micrometeorites (Moses et al., 1999; Syal et al., 2015). While we cannot completely rule out the contribution of solar wind to Mercury's ice budget, we find it unlikely it is a significant source; to explain Mercury's surface darkening, the accumulated volatiles must contain organic compounds that only exist in comets or meteorites and not in pure hydroxyl.

Due to their thinness, micro cold-traps can only remain visible on the surface if the delivery rate is much greater than the overturn rate (Zhang and Paige, 2009). However, Moses et al. (1999) and Syal et al. (2015) found the average ice delivery rate from micrometeorites is at most a few m Ga^{-1} (using recent estimates for the cold-trap area fraction, (Paige et al., 2013; Chabot et al., 2018)), same order of magnitude as the lateral regolith mixing rate (Hurley et al., 2012) and lower than the mixing rate in the upper few centimeters (Gault et al., 1974; Speyerer et al., 2016; Costello et al., 2017b). Monte-Carlo simulations conducted

on the Moon (Hurley et al., 2012) and Mercury (Crider and Vondrak, 2003) show only 50% of an initially 10 cm thick ice deposit will survive after 10 Ma, preventing it from developing a thermal lag or stay pure enough to be radar bright. Exposed volatiles on Mercury were found to be covered by regolith at a rate of ~ 0.5 cm Ma^{-1}, further reducing the purity of the precipitating volatile (Crider and Vondrak, 2003). Therefore, it is unlikely volatiles delivered by micrometeorites alone are sufficient to explain the presence of a darkened thermal lag covering ice trapped in micro cold-traps, or the presence of a pure, radar bright ice layer in the larger cold-traps.

Over long time periods, the amount of ice delivered episodically, *e.g* in a volcanic eruption or a comet impact (Butler, 1997; Moses et al., 1999; Kerber et al., 2009), is not significantly different from the amount of ice delivered by micrometeorites over long time periods. However, over short time periods, episodic events deliver large quantities of volatiles. Of the two episodic mechanisms listed above, comets contain all the carbonaceous materials that may potentially form a thermal lag over volatiles deposits (Zhang and Paige, 2009; Delitsky et al., 2017). Recent hydrocode simulations (Ong et al., 2010; Stewart et al., 2011) showed that the volatile retention rate following a comet impact on the Moon is $\sim 0.1\%$. Previous models (Butler, 1997; Moses et al., 1999) found higher retention rates for Mercury, $5\% - 15\%$. Adopting lunar models for Mercury may be inaccurate due to the higher gravity, that helps preserve the volatile molecules, and the higher surface temperatures, that encourage loss through sublimation. However, we can use these retention rates to obtain an order of magnitude estimation for the amount of ice trapped in cold-traps following a comet impact.

For example, a 5 km comet will deposit a layer of ice that is a few cm (0.1% retention) up to a few decimeters (5% retention) thick - enough to fill a significant portion of the micro cold-traps. This amount of ice should better outlast space weathering (Morgan and Shemansky, 1991) and impact erosion and eventually develop a thermal lag that will further protect the ice. Therefore, we conclude an episodic deposition, such as a comet impact, is more likely to dominate ice accumulation on Mercury. This observation agrees with the

recently measured uneven distribution of ice inside PSRs (Chabot et al., 2018).

Finally, the relative shallowness of these micro cold-traps shows this emplacement could not have been primordial, as gardening would have eroded the thermal lag covering the trapped ices. We can constrain the age of the ice trapped in these cold-traps, assuming its origin is a comet impact. As mentioned above, the median permanent shadow depth of micro cold-traps of lateral scales 1 m is lower than a few decimeters. In that case, and considering traditional overturn rates for the Moon as a first order estimate (Gault et al., 1974; Hurley et al., 2012), the most recent deposition must have occurred within the last 10^8 years. Evidence shows (Neish et al., 2013) the gardening rate on Mercury may be faster than on the Moon, possibly indicating a more recent deposition. Recently acquired observations and models that account for secondary impacts predict a much higher erosion rate on both the Moon and Mercury (Speyerer et al., 2016; Costello et al., 2017b). In this case, micro cold-traps could only outlast if the deposition occurred within the last $10^6 - 10^7$ years. For cold-traps of lateral scales 10 m, the maximum permanent shadow thickness is < 1 m, changing the time of deposition to 10^9 years and 10^8 years, respectively. Lateral mixing should further decrease these timescales.

4.5 Acknowledgements

The MLA reflectance and topography data used in this manuscript are available from the Planetary Data System (`http://pds-geosciences.wustl.edu/missions/messenger/mla.htm`) and the Arecibo radar images are publicly available on `http://www.naic.edu/~radarusr/Mercpole/`. The north pole maximum temperature binary files used to determine ice stability are available on `http://luna1.diviner.ucla.edu/~dap/tmp/merc75nf.tavmax.grd`. The modeled cold-trap fractions and permanent shadow depth distributions used to produce Figures 3 and 6 and 8 may be downloaded from the author's personal website, `http://liorruba.com/micro_ct_ref_data`.

CHAPTER 5

Thick ice deposits in shallow simple craters on the Moon and Mercury

This chapter was originally published in: Rubanenko, L., Venkatraman, J. and Paige, D.A., 2019. Thick ice deposits in shallow simple craters on the Moon and Mercury. *Nature Geoscience*, 12(8), pp.597-601.

Abstract

Permanently shadowed regions near the poles of Mercury and the Moon may cold-trap water ice for geologic time periods. In past studies, thick ice deposits have been detected on Mercury, but not on the Moon, despite their similar thermal environments. Here we report evidence for thick ice deposits inside permanently shadowed simple craters on both Mercury and the Moon. We measure the depth/diameter ratio of approximately $2,000$ simple craters near the north pole of Mercury using Mercury Laser Altimeter data. We find that these craters become distinctly shallower at higher latitudes, where ice is known to have accumulated on their floors. This shallowing corresponds to a maximum infill of around 50 m, consistent with previous estimates. A parallel investigation of approximately $12,000$ lunar craters using Lunar Reconnaissance Orbiter data reveals a similar morphological trend near the south pole of the Moon, which we conclude is also due to the presence of thick ice deposits. We find that previously detected surface ice deposits in the south polar region of the Moon are spatially correlated with shallow craters, indicating that the surface ice may be exhumed or linked to the subsurface via diffusion. The family of lunar craters that we

identify are promising targets for future missions, and may also help resolve the apparent discrepancy between the abundance of frozen volatiles on Mercury and the Moon.

5.1 Main

The origins and distribution of cold-trapped ices near the poles of Mercury and the Moon are poorly constrained. The low obliquity of these planetary bodies causes polar topographic depressions to cast highly persistent shadows (Urey, 1952). If sufficiently cold, these permanently shadowed regions (PSRs) are able to trap and preserve volatiles, such as water ice, for billions of years (Watson et al., 1961). Evidence gathered by the Arecibo radio telescope and later by the Mercury Surface, Space Environment, Geochemistry and Ranging (MESSENGER) spacecraft indicates that cold-traps on Mercury harbour pure ice deposits more than a few metres thick (Harmon and Slade, 1992; Slade et al., 1992; Paige et al., 2013; Deutsch et al., 2017a). Similar radar investigations conducted on the Moon have thus far found little evidence for widespread thick ice deposits (Stacy et al., 1997; Campbell et al., 2006). The Lunar Crater Observation and Sensing Satellite (LCROSS) mission detected 5%10% water by mass (Colaprete et al., 2010) in the uppermost few metres of the floor of Cabeus Crater. Thus far, only scattered surface and near-surface deposits have been detected in polar cold-traps by the Lunar Reconnaissance Orbiter (LRO) (Hayne and Aharonson, 2015; Fisher et al., 2017; Li et al., 2018). This difference is particularly surprising as the polar thermal environments and the net volatile accumulation rates on Mercury and the Moon are not believed to be vastly different (Paige et al., 2013, 2010b; Lawrence, 2017). Adding to the puzzle, neutron spectrometers have detected enhanced hydrogen concentrations in the near subsurface of both Mercury and the Moon that are probably due to the presence of water ice (Mitrofanov et al., 2010; Feldman et al., 1998; Lawrence et al., 2013).

Here we analyse the morphology of 2.515 km craters near the north pole of Mercury and find that they contain thick ice deposits, congruous with earlier observations of thick ice in larger craters. By performing a similar analysis on the Moon, we infer the existence of

analogous thick ice deposits in shallow craters near the lunar south pole.

5.2 Evidence for ice in craters on Mercury and the Moon

We identify 2,069 simple craters (diameter 2.515 km) on the Mercury Dual Imaging System (MDIS, Hawkins et al. (2007)) basemap and measure their depth/diameter (d/D) ratios using the Mercury Laser Altimeter (MLA, Cavanaugh et al. (2007)) polar topographic basemap gridded at a resolution of 250 $m\ px^1$ (Figure 5.1a; see Methods). We restrict our measurements to latitudes $> 75°88°$ N, where the highest quality MLA and MDIS data were gathered due to MESSENGER's orbit. Figure 1b shows that the mean d/D ratio of all craters decreases by $\sim 10\%$ from latitude 75° to 86°. Extrapolating this trend to the pole yields a maximal shallowing of $\sim 20\%$ (roughly 50 ± 5 m), considering our crater size range (see Supplementary Information for error estimation). In lower latitudes, the smaller permanently shadowed volume cast by craters restricts the amount of ice they may potentially trap. The average infill, therefore, is lower: $\sim 15 \pm 1$ m. Results are shown in Figure 5.1. The grey dots in the lower panels represent craters that cast permanent shadows, as calculated using an analytic shadowing model. The blue dots are craters that both cast permanent shadows and are also sufficiently cold to trap water ice according to an analytic radiation scattering model (Ingersoll et al., 1992). The black dashed lines show the extent to which these craters are filled relative to their potential ice filling capacity that is, to first order, given by the volume of the PSR they cast (Rubanenko et al., 2018) (see Methods).

The poleward shallowing we observe on Mercury is consistent with the presence of previously detected thick water ice deposits in larger craters. We support this claim by several lines of evidence. First, the mean d/D decreases at the same latitudes in which craters are modelled to cold-trap significant amounts of water ice (Fig. 5.1a, see Methods). We note the shallowing does not fit the presence of other prevalent volatile species, as those are cold-trapped at different temperatures (Paige et al., 2013; Rubanenko et al., 2018). Second, as ice accumulates in cold-traps, it should have a greater effect on the depth of smaller

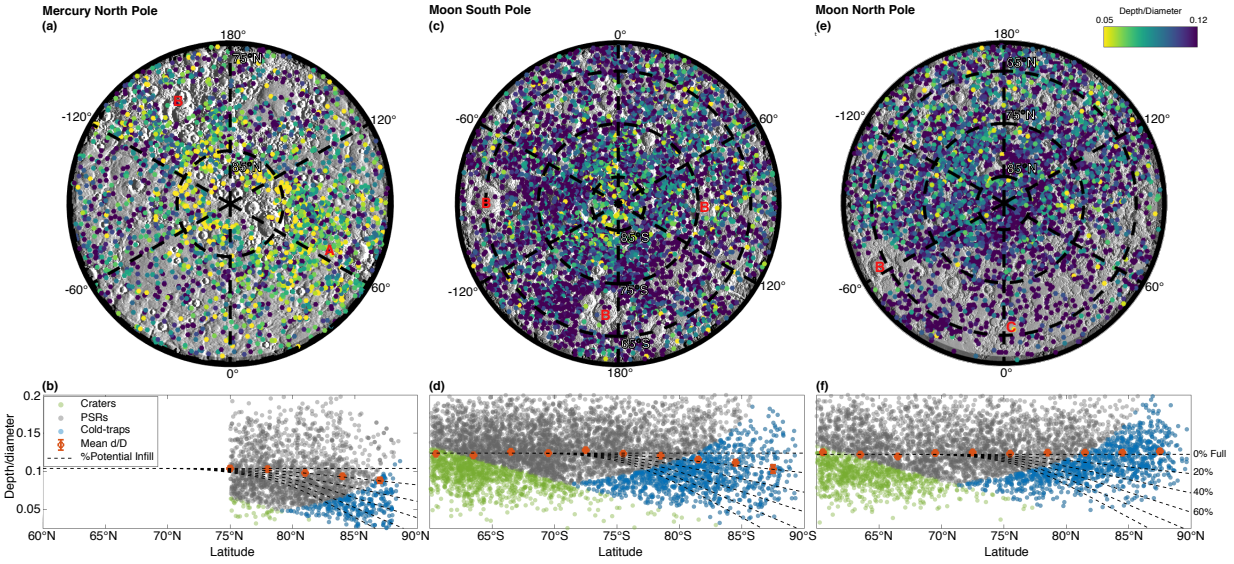

Figure 5.1: (a,c,e) Maps showing the catalogued craters with their corresponding d/D ratios for Mercury's north pole (a) (latitude $> 75°$ N), and the Moon's south (c) and north poles (e) (latitude $> 60°$ N/S). The red uppercase letters indicate areas of interest. A: large population of shallow, elliptical craters that are possibly secondary craters of Prokofiev Crater. B: the lower crater density near larger craters (for example, lunar Antoniadi, Hausen and Pythagoras Craters, all Upper Imbrian (Haruyama et al., 2009; McEwen et al., 1993)) indicates that our sampled smaller craters are typically a few billion years old. C: the crater density is much lower in and around the lunar Maria. b,d,f, Plots showing the d/D ratios of all the craters sampled for Mercury's north pole (b), and the Moon's south (d) and north (f) poles. The green and grey markers are non-permanently and permanently shadowed craters, respectively. The blue markers indicate craters that are sufficiently cold to trap water ice according to a thermal model (Ingersoll et al., 1992). The red markers show the mean d/D ratio of all the catalogued craters in bins of 3°, after removing craters suspected as secondaries (see Methods). The black dashed lines show the extent to which craters are filled relative to their potential ice filling capacity based on PSV. The error bars indicate one standard error to the mean.

craters compared to larger craters. We find that the shallowing trend in larger craters, 7.515 km, is significantly diminished compared to smaller craters, 2.55 km (Supplementary Fig. 1). Third, the colder pole-facing slopes of atypically shallow craters are shallower than the warmer, equator-facing slopes (Supplementary Fig. 2). On Mercury, the median of the pole-facing slopes distribution is $\sim$ 10% shallower than that of the equator-facing slopes distribution. Fourth, the average shallowing we measure corresponds to approximately 20% of the permanent shadow volume (PSV), or roughly 10 m, in accord with previous theoretical22 and observational6 estimates for the thickness of polar ice deposits detected in individual craters (Harmon and Slade, 1992; Slade et al., 1992; Paige et al., 2013; Chabot et al., 2014). Our statistical approach allows us to better constrain the average thickness of polar ice deposits than has been possible in previous studies. Fifth, Mercury's eccentric orbit and its 3:2 spinorbit resonance causes roughly half its polar region (termed 'the warm pole' longitudes) to be exposed to more insolation than the other half (termed 'the cold pole' longitudes), (Paige et al., 1992). We find that craters in the cold pole longitudes of Mercury are shallower than craters in its warm pole longitudes (Supplementary Fig. 3).

We have conducted a parallel investigation of the morphology of simple craters in the polar regions on the Moon. The polar orbit of LRO allows us to extend our survey to latitudes 60°90° (N/S) and measure $11,228$ craters in the same size range as on Mercury (Fig. 5.1cf; see Methods). We refine the data as explained above and in the Methods. Figure 5.1d,f shows that the d/D ratio of lunar craters decreases with latitude near the south pole but not the north pole of the Moon. We note that in both polar regions, the average d/D equatorward of latitude 75° N/S is nearly equal and matches previous surveys25, 0.1242 and 0.1262 for the northern and southern hemispheres, respectively. In the southern hemisphere, the shallowing starts near latitude 75° S, where craters become cold-traps according to thermal models (Ingersoll et al., 1992; Rubanenko and Aharonson, 2017), and extends to the pole. Near the south pole, craters become $\sim$ 15% shallower, corresponding to a maximal shallowing of $\sim 50 \pm 4$ m. The average infill is $\sim 10 \pm 1$ m. A previous study (Kokhanov et al., 2015) documented similar crater shallowing at both lunar poles for a smaller sample

size and smaller crater size range, finding south polar craters to be shallower than north polar craters.

The morphological trend we observe near the south pole of the Moon resembles the one on Mercury; the poleward shallowing is of the same order (Fig. 5.1b), and pole-facing slopes are slightly shallower than the equator-facing slopes (Supplementary Fig. 2b). This resemblance, along with the correlation we find between cold-trapping craters and their d/D, leads us to conclude that craters become shallower due to the presence of thick ice deposits (Fig. 5.1). The absence of an analogous morphological trend near the north pole does not necessarily imply a null result; ice deposits may still be present in north polar craters, but the deposits may not be sufficiently thick to cause statistically significant shallowing.

5.3 Nature of Trapped Ice Deposits

Next we examine the relationship between the thick ice deposits we infer in this study and previously detected surface ice on the Moon, obtained by correlating near-infrared spectroscopy acquired by the Moon Mineralogy Mapper (M^3) on Chandrayaan-1 with data acquired by LRO (Li et al., 2018). We divide each polar region (latitudes 8090 N/S) into areal bins of 60 km^2, and calculate the mean d/D and surface ice area fraction in every bin (see Methods). Figure 5.2 shows that the mean d/D is negatively correlated with the surface ice area fraction in the south pole, suggesting that some of these surface ice deposits may be exhumed or replenished by water molecules diffusing from depth, a process that has been demonstrated theoretically to be possible on geologic timescales (Schorghofer and Taylor, 2007; Schorghofer and Aharonson, 2014). However, this correlation does not rule out other mechanisms for the present-day accumulation of surface ice, such as the cold-trapping of exospheric volatiles (Watson et al., 1961; Schorghofer, 2015).

In the north polar region of the Moon we find that shallow craters are not spatially correlated with the locations of surface ice deposits. The lack of this correlation in the north, along with the absence of a morphological trend mirroring the one in the south,

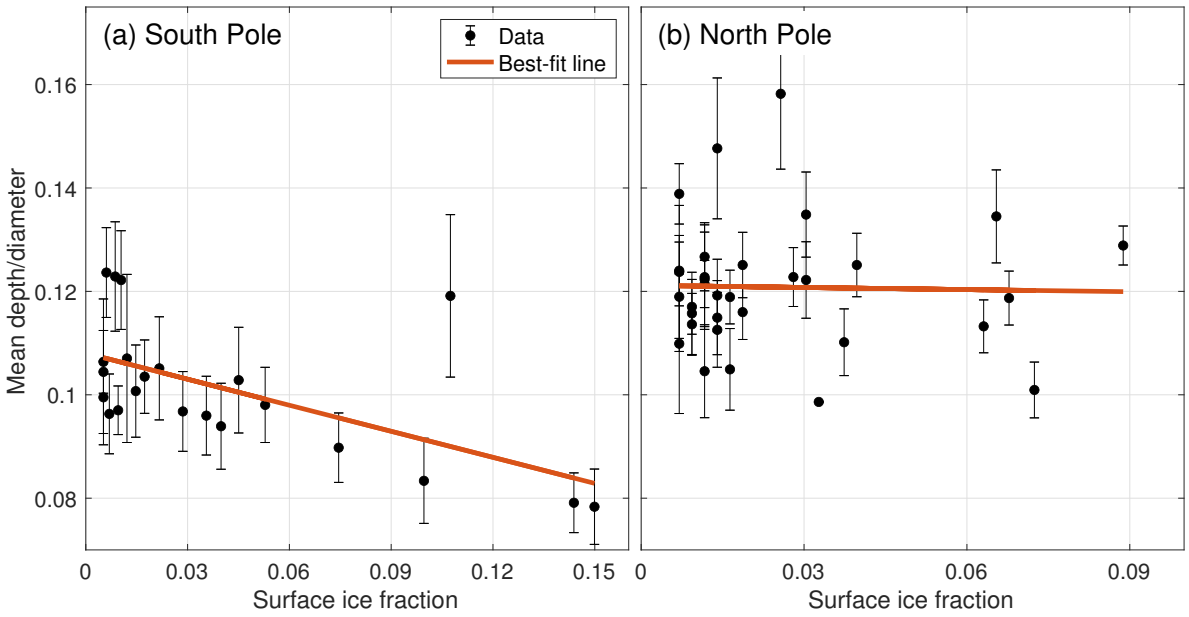

Figure 5.2: Surface ice data were composed by correlating near-infrared spectra obtained by M^3 aboard the Chandrayaan-1 with data acquired by LRO (Li et al., 2018). a,b, We find a negative spatial correlation between the family of shallow craters we identified near the south pole (a) but not near the north pole (b) of the Moon. For clarity, we show only bins with surface ice fraction $> 0.5\%$. Craters under that threshold do not significantly affect our result, emphasized by the least-squares best-fit line. The error bars represent one standard error to the mean. Some of the error bars are smaller than the data points they support.

is puzzling and poorly understood. A possible explanation may lie in the relative ease of volatile destruction compared to volatile accumulation. It is possible that craters in the north contained thick ice deposits in the past that were later destroyed by, for example, the heat produced by the Imbrium-forming impact (see Supplementary Information). This is consistent with the previously observed sparsity of surface ice in the north relative to the south (Fisher et al., 2017; Li et al., 2018).

Considering the $\sim$ 10 m average shallowing we infer for lunar south polar craters and assuming a typical ice-free lunar highlands regolith thickness of $\sim$ 1020 m Fa and Wieczorek (2012), we estimate that lunar subsurface deposits may be typically composed of $\sim$ 3050% ice by mass. Water ice in these concentrations would not be expected to produce strong radar backscattering, which is in general agreement with available lunar radar observations (Stacy et al., 1997; Campbell et al., 2006; Spudis et al., 2013). These ice concentrations are also in rough agreement with the results of the LCROSS impact in Cabeus Crater, which have been interpreted to indicate the presence of up to 10% ice by mass in the uppermost metres (Colaprete et al., 2010).

5.4 Ice accumulation history on Mercury and the Moon

The areal density of craters in our survey is depressed in the areas surrounding larger Upper Imbrian craters such as Antoniadi, Hausen and Pythagoras (Fig. 5.1, regions marked B). This indicates that the smaller craters in our sample predate these Upper Imbrian cratersand thus are typically a few billion years old (Haruyama et al., 2009; McEwen et al., 1993). Although the age of the craters puts an upper limit on the age of the deposits, it does not preclude the possibility that they may be due to a recent asteroid or comet impact. However, we find it more likely that these deposits are primordial due to their thickness, which implies that they were delivered over long timescales, and the absence of a clear radar signal, which implies that they are buried or mixed into the regolith.

A potential mechanism for the accumulation of buried, eroded water ice deposits in

craters is shown in Fig. 5.3. Surface ice accumulates equally in all permanently shadowed craters due to, for example, a large comet impact. After ice is deposited into cold-traps, it is buried under regolith ejected by mass wasting or from nearby impact craters (Fig. 5.3a,b). Finally, the regolith is gardened and the ice is exposed, producing a deposit with a low ice fraction at the surface. This process may repeat itself. In this model, polar ice deposits have a distinct topographic signature that is more readily detected in smaller craters because of their relative larger infill. However, these physical mechanisms we propose to be responsible for the accumulation and burial of ice should operate equally well in larger cold-traps to create $\sim$ 10 m-thick ice-rich layers.

5.5 Future investigations of polar deposits

The statistical methodology employed in our study prevents us from identifying specific craters that contain ice, as individual craters may appear shallower or deeper than average due to their impact formation energy or the local geology (Pike, 1977). We find it unlikely that phenomena unrelated to volatiles such as contamination by secondary craters, a local geologic deposit with different material strength, or crater degradation cause the shallowing we observe. Removing highly elliptical craters, suspected as secondaries, does not significantly affect our results. Furthermore, we find no correlation between craters' d/D and the presence of large geologic deposits or the age of the surface (see full discussion in Supplementary Information).

We may use our results to re-estimate the total mass of the ice trapped in the lunar poles. Lunar cold-traps have been previously estimated to occupy $\sim 10^4$ km^2 (Paige et al., 2010a). If all cold-traps hide a $\sim$ 10 m-thick pure subsurface ice deposit, the total mass of water ice on the Moon could be estimated to be up to $\sim$ 100 billion metric tons. This is approximately two orders of magnitude greater than previous estimates that are based on surface detections and the LCROSS impact results (Colaprete et al., 2010; Hayne and Aharonson, 2015; Fisher et al., 2017; Li et al., 2018). Our results combined with previous radar data imply that the

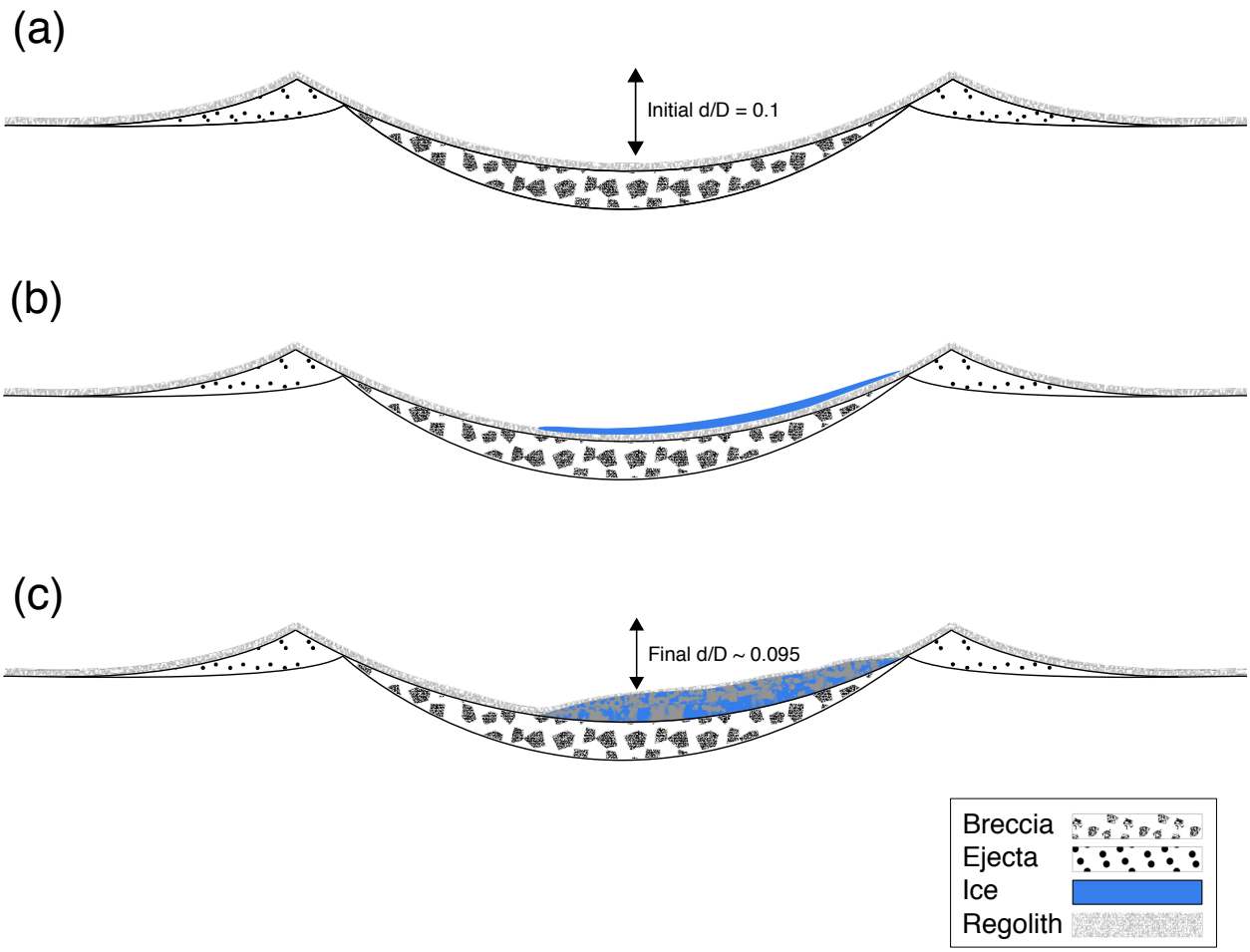

Figure 5.3: (a) A crater is formed, and then covered by regolith. (b) A $\sim$ 10 m-thick ice deposit accumulates in the crater over a short time period. (c) Ejecta from nearby craters or mass wasting buries the ice, slowing sublimation. With time, impact gardening exposes some of the ice, or it may reach the surface by way of diffusion. This process may repeat itself after each deposition. The vertical dimension is exaggerated for emphasis.

most concentrated lunar ice deposits are likely to be buried a few meters under permanently shadowed south polar cold-traps. The possibility that thick ice-rich deposits exist on the Moon may not only help resolve the outstanding question regarding its low ice abundance relative to Mercury, but may also have practical applications in preparation for a future permanent lunar settlement.

5.6 Methods

5.6.1 Identifying and measuring craters

We begin by manually identifying simple impact craters on the MDIS and LRO Camera (LROC) visible imagery polar mosaics using the JMARS crater counting tool. We record the crater coordinates and diameter, omitting craters that overlap other craters as those might not have a symmetric profile. In lower latitudes, the lighting conditions might make it more difficult to identify shallower craters. To mitigate this observation bias, we use the shaded relief polar mosaics calculated by the Lunar Orbiter Laser Altimeter (LOLA), LROC and MLA as an additional reference. For MLA and LOLA, we have used data obtained from Planetary Data System 3, v.2. After identifying the craters, we extract three topographic profiles from the MLA and LOLA elevation maps gridded at a resolution of 250 m px^1 and 120 m px^1, respectively. One profile in the equatorialpolar direction, and two additional profiles along the long and short axes of the crater. We choose the craters' long and short axes from 50 topographic profiles passing through the center of the crater and rotated at a fixed angular increment. To measure the crater's depth, diameter and mean slope we find the crater's rims and centre using an algorithm we developed: we begin by subtracting a linear least-squares best fit from the profile to remove large-scale slope effects. Then, we smooth the topography using a Gaussian filter to remove small-scale topographic noise. We calculate the second derivative of the profile to find the deepest point in the crater. Using this point as a reference, we divide the crater into two parts. For each part, we calculate the first derivative and set the rim as the location in which it decreases to 10% of the steepest

slope. The horizontal coordinate of the centre of the crater is defined as the median of the line segment bounded between the two rims. The depth of the crater is calculated as the difference between the average height of the rims and the height of its centre averaged over the three profiles. The diameter of the crater is set as the distance between the two rims. The median profile slope used to derive Supplementary Fig. 3 is calculated as the median of the first derivative of the polarequatorial profile of the craters in our sample. The data are further processed by manually reviewing the topographic profiles and discarding false positives. We remove outliers ($d/D < 0.025$ and $d/D > 0.25$), and those suspected as secondaries that may skew our results (see later). The contours in Supplementary Fig. 8 outline the full extent of the data range in depthdiameter space. Our catalogue is complete to a d/D of ~ 0.07 relative to a recently acquired lunar crater catalogue (Salamunićcar et al., 2014).

5.6.2 Removing secondary craters

Secondary craters tend to be shallower and more elliptical than primary craters (Bierhaus et al., 2018). Consequently, a recent prominent polar impact (such as the one that formed Prokofiev Crater) might skew our result by contaminating the polar region with secondaries, lowering its mean crater depth. We deal with this possible contamination by discarding highly elliptic craters (circularity < 0.85, characteristic limit for secondaries (Schultz and Singer, 1980)) and those found along crater rays. In this process, we have removed $\sim 1015\%$ of the overall crater population. For example, and although this is not in the scope of this work, we identify and map craters suspected as Prokofiev Crater's secondaries (group A in Fig. 5.1a). These craters are anomalously shallow and elliptic, and follow distinct crater rays that stretch from Prokofiev Crater towards the equator.

5.6.3 Maximum potential ice infill and cold-trapping ability

To first order, the thickness of a cold-trapped ice deposit is limited by the depth of the PSV harbouring it (Rubanenko et al., 2018). We use this limit to estimate to what extent the depth of a simple crater would change due to the presence of a thick ice deposit. Simple craters < 15 km are well approximated by hemispherical (bowl-shaped) cavities (Ingersoll et al., 1992; Pike, 1977; Buhl et al., 1968). This approximation allows calculating the PSV and cold-trapping ability of craters as a function of latitude and d/D ratio. To prepare Fig. 5.1df we determine which craters in our sample would cast permanent shadows (grey dots) and which will not (green dots). The deepest instantaneous shadow ds cast by a crater with depth d at incidence angle θ_i is,

$$\frac{d_s}{d} = \beta - \sin\theta_i(\beta - 1 + \cot\theta_i\sqrt{2\beta - 1}) \tag{5.1}$$

where $\beta \equiv \frac{1+4\Delta^2}{8\Delta^2}$ and Δ is the crater d/D ratio. Craters will cease casting a permanent shadow for $ds = 0$, which occurs when,

$$\beta = \frac{1}{1 - \beta\sin\theta_i} \tag{5.2}$$

Assuming the obliquity is very small, at noon the incidence angle equals the local latitude, $\varphi = \theta_i$, and the above equation can be reduced to,

$$\sin\varphi = \frac{1 - 4\Delta^2}{1 + 4\Delta^2} \tag{5.3}$$

The shallowest instantaneous shadow cast at the centre of the crater during the day sets the depth of the permanent shadow at the same point. For hemispherical craters, this shallowest instantaneous shadow is cast at noon, when the solar incidence angle equals the local latitude. The maximum potential ice infill is the extent to which an ice deposit would decrease the depth of a simple crater. As explained above, the PSV depth is an upper limit

for this maximum potential ice infill. We can calculate the depth of the PSV at the centre of the crater using simple trigonometry

$$\frac{d_s}{d} = 1 - \frac{1}{2\Delta} \cot \theta_i \tag{5.4}$$

We use this equation to plot the black contours shown in Fig. 5.1df.

Our simplified permanent shadow model assumes that regional slopes do not tilt the crater and that the obliquity, and thus the solar declination angle, is zero. In addition, it assumes an idealized hemispherical shape for the crater and ignores small-scale topographic imperfections such as impact craters and mass wasting. The former are factors that may potentially impair the ability of the crater to cast a permanent shadow: tilted surfaces may expose the floor of the crater to solar illumination at angles not predicted by our model, and the obliquity to the ecliptic causes the Sun to be slightly higher at noon and rise and set at different solar azimuths throughout the year. The latter is a more important effect that may be analytically quantified. The azimuth of sunrise/sunset is given by,

$$\cos a_s = \frac{\sin \delta}{\cos \phi} \tag{5.5}$$

where δ is the solar declination angle and φ is the latitude. Taking the largest solar declination δ =obliquity, as is the case at summer solstice, we see that the effect of obliquity on the permanent shadow is greatest in high latitudes. For example, the lunar obliquity is $\sim 1.5°$; in latitude 80°, the largest deviation in azimuth of the sunrise from east is $\sim 9°$ towards the pole. However, this effect is compensated for by the low maximum possible solar elevation angle that leaves most of the crater's floor shadowed.

5.6.4 Determining ice stability in craters

Ice stability on airless surfaces is proportional to the equilibrium vapour pressure. Consequently, it is highly sensitive to temperature variations (Watson et al., 1961; Schorghofer and Taylor, 2007). For example, the sublimation rate of exposed ice at 115 K is $\sim$ 1 m per billion

years, three orders of magnitude greater than the sublimation rate 100 K. Consequently, it is common to define a 'cold-trap temperature', above which volatiles cannot remain stable for geologic time periods. This definition varies as it depends on the mass of the sublimating ice deposit and the timescales. Here we choose this temperature to be $T_{ct} = 115$ K, corresponding to a sublimation rate of ~ 1 m per billion years appropriate for our problem. The temperature distribution of a hemispherical (bowl-shaped) crater depends on the regolith optical properties, the crater latitude and the d/D ratio Δ. To estimate which craters are cold-traps, we calculate their PSR equilibrium temperature T using an analytic scattering model (Ingersoll et al., 1992; Buhl et al., 1968),

$$\sigma T^4 = F_0 \sin e_0 \frac{f - Af}{1 - Af} \left[1 + \frac{A(1-f)}{\varepsilon}\right] \tag{5.6}$$

where F_0 is the solar constant, e_0 is the solar elevation angle, A is the surface albedo, $\varepsilon = 0.95$ (Rubanenko and Aharonson, 2017) is the infrared emissivity and $f = 1/(1 + 1/4\Delta^2)$. For Mercury, we use $A = 0.08$ and for the Moon $A = 0.13$ (Rubanenko et al., 2018; Domingue et al., 2011). The highest PSR temperature during the day, which serves as the criterion for ice stability, is obtained at noon, when the solar elevation angle equals the co-latitude. To find which craters are cold-traps, we first determine which craters cast a permanent shadow using equation 5.3, and then verify that this shadow temperature is lower than T_{ct} using equation 5.5.

5.6.5 Correlation between surface ice and crater morphology

Recently (Hayne and Aharonson, 2015; Fisher et al., 2017; Li et al., 2018), positive detections of surface ice deposits were mapped by constraining near-infrared spectra obtained by the M^3 instrument onboard the Chandrayaan 1 spacecraft with previously gathered LRO data (Hayne and Aharonson, 2015; Fisher et al., 2017; Li et al., 2018). To test whether these detected surface ice deposits are spatially correlated with the family of shallow craters we identify here, we divide the polar region (between 80° N/S and the pole) into areal bins of

60 km^2. For each bin, we calculate the normalized area-weighted frequency of positive ice detections and the mean d/D of craters, to find that they are negatively correlated (Fig. 5.2). We further check and find that this correlation is statistically significant at the 5% significance level (see Supplementary Information).

CHAPTER 6

Conclusions and Prospect

The work presented here concludes four years of research I conducted in UCLA, studying the thermal stability of ice on the Moon and Mercury. The last chapter of this work both serves as a summary and lays the foundations for a future investigation of how mechanical processes affect the stability of ice trapped on airless surfaces.

Throughout this work, I set to investigate the difference in the amount of volatiles trapped on Mercury and the Moon only to find it is potentially smaller than previously thought (Chapter 4). This surprising discovery uncovered another question left to be answered: if meters-thick ice deposits are trapped near the poles of both planetary bodies, why on Mercury they are so much purer (radar bright, see Chapter 4) compared to the Moon?

The general hypothesis is that the basic physical properties of Mercury and the Moon affect the turnover rates on the floors on craters. In the lower gravitational environment of the Moon, downslope diffusion caused by seismic shaking and impact ejecta are significantly more effective in redistributing regolith that protects trapped ice deposits. As a result, most cold-trapped ice is quickly covered and mixed into the regolith. Mercury's stronger gravity makes this redistribution and mixing less effective. In addition, the presence of the heavier carbonaceous volatiles on Mercury but not on the Moon (chapter 4) further halts sublimation shortly after accumulation. These factors may make ice deposits on Mercury accumulate faster and be more pure than ice deposits on the Moon.

To investigate how these processes affect ice stability I employ a probabilistic, Monte-Carlo impact gardening model, following fundamental works that modeled impact gardening on airless surfaces (Gault et al., 1974; Arnold, 1975; Richardson, 2009; Rosenburg et al.,

2015). The stochastic mechanical features of the model are incorporated with volatile stability thermophysical simulations similar to those described in Chapter 3.

6.1 Impact Gardening Model

Due to its collisional history, the size distribution of bodies in the asteroid belt assumes the shape of a steep power law (Dohnanyi, 1969). Dynamical models (Williams and Wetherill, 1994; Bottke Jr et al., 2005) and observations (Brown et al., 2002; Mainzer et al., 2014) have found that Near Earth Asteroids (NEAs) and bollides penetrating Earth's atmosphere also follow a power laws with slightly different slopes. If we assume these two populations are the main source for lunar impactors, their joint cumulative size distribution may be described by a broken (piecewise) power law,

$$N(>D) = \begin{cases} a_1 D^{-b_1}, & D \leq D_i \\ a_2 D^{-b_2}, & D > D_i \end{cases}, \tag{6.1}$$

where $N(>D)$ is the number of bodies with diameter $> D$ impacting the surface per unit area. The distribution parameters $a_{1,2}$ and $b_{1,2}$ are the power-law coefficients and exponents. In this formulation, a also represents the number of bodies > 1 m impacting the surface per unit area per Ma.

We estimate $a_{1,2}$ and $b_{1,2}$ for the Moon by fitting a line to the log transformed known impactor cumulative flux distribution (Figure 6.1). For impactors < 10 m we use the global bolide energy distribution database. We estimate the kinetic energy of the bolide from the energy its fireball emits as it penetrates the atmosphere (Brown et al., 2002) and derive its size assuming an impact velocity of 20 km s^{-1} and a density of 3000 kg m^{-3}. Due to the high variability of the impact flux before the year 2000, we only consider fireballs identified between the years $2000-2019$. For impactors > 1 km we use the most recently updated Near Earth Ateroids (NEA) data normalized to 1 km and converted to impact flux using previous estimates for the impact probability, $P(>1 \text{ km}) = 3.11 \times 10^{-15}$ $\text{Ma}^{-1}\text{m}^{-2}$ (Le Feuvre and Wieczorek, 2011). To estimates NEA sizes, we convert their magnitude to effective spherical

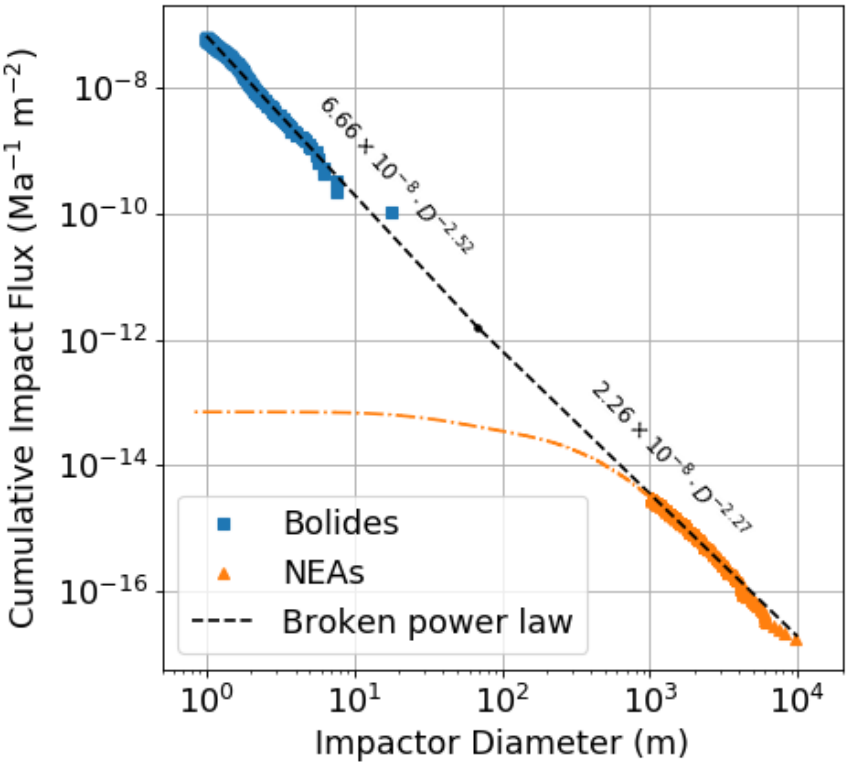

Figure 6.1: The impactors production function we use to simulate craters. For scales $<$ 10 m (blue squares) we use the global fireball energy cumulative distribution converted to impactor diameter (Brown et al., 2002). For scales $>$ 1 km (orange triangles), we use recently updated NEA size distribution converted to impact flux using dynamical models (Le Feuvre and Wieczorek, 2011). The data gap between 10 m and 1 km is due to an observation bias, also emphasized by the dashed orange line. Black dashed line shows the best fit power law.

diameter D_{eff}, assuming an albedo of $p_v = 0.14$ (Mainzer et al., 2012, 2014),

$$D_{eff} = \frac{1329 \cdot 10^{-0.2H}}{\sqrt{p_v}}. \tag{6.2}$$

6.1.1 Crater Size Scaling

We model the evolution of airless topographies by populating an initially flat rectangular surface with impact craters using the Monte-Carlo method (also see Oberbeck et al., 1973; Arnold, 1975; Richardson, 2009). In every model time step, an impactor diameter D is randomly drawn from the cumulative piecewise power law flux distribution shown above (Eq. 6.1). For other bodies in the solar system whose parameters are not as well constrained this broken power law may be replaced with a single power law.

For every randomly drawn impactor, we also draw an impact location from a uniform distribution. Impactors are assumed to come into contact with the surface at angle of 45° and form a symmetrical transient crater, employing previously derived scaling laws (Holsapple, 1993). The equations governing crater formation and ejecta placement in our model are based on the Cratered Terrain Evolution Model (CTEM) developed in Richardson (2009). Here we only discuss some of these equations and refer the reader to Richardson et al. (2007) and Richardson (2009) for the full derivation.

In the heart of cratering models lies the basic assumption that the size of the final crater is much smaller than the size of the projectile. This assumption, which is true in most cases, allows expanding the power laws observed in experimental impacts as point-source solutions to solve for the mass, velocity and acceleration of the impacted material employing scaling the well-known Buckingham π theroem of dimensional analysis (Buckingham, 1914; Melosh, 1989).

Upon contacting the surface, the impactor compresses the target material and excavates material in the form of jets of impact ejecta. An initial transient cavity is formed whose

volume is,

$$V_t = K_1 \left(\frac{m_i}{\rho_t}\right) \left[\left(\frac{g a_i}{v_i^2}\right) \left(\frac{\rho_t}{\rho_i}\right)^{-\frac{1}{3}} + \left(\frac{\bar{Y}}{\rho_t v_i^2}\right)^{\frac{2+\mu}{2}} \right]^{-\frac{3\mu}{2+\mu}} \tag{6.3}$$

where v_i is the impact velocity and m_i is the mass of the impactor, assumed to be spherical with radius a_i and density ρ_i. We account for the impact angle by multiplying the v_i by an additional cosine term, whose argument is drawn from a uniform distribution between 0 and 2π. g is the acceleration due to gravity, K_1 is a material dependent proportionality constant and $\bar{Y}$ is the effective yield strength of the target material. $1/3 < \mu < 2/3$ is a parameter that affects the physical dimensions of the coupling parameter (see Holsapple and Schmidt, 1987), and determines if the impact is governed by the impactor momentum ($\mu = 1/3$) or kinetic energy ($\mu = 2/3$). The transient crater radius R can be then trivially calculated from the transient volume using $R = (3V/\pi)^{1/3}$. In the last stage of crater formation the transient cavity is modified by gravity, collapsing into the final crater whose radius is larger in comparison. For simple craters (< 20 km on the Moon), the diameter of the final crater is given by $D_f = 1.18 D_t$. In Figure 6.2 we show an example run of our model.

6.1.2 Ejecta Emplacement Distance and Thickness

The ejection velocity of excavated material decreases with the distance from the impact location r. To model the thickness of the ejecta layer as a function of r we employ Maxwell's Z-model of crater excavation (Maxwell, 1977; Richardson et al., 2007). The ejecta thickness as some distance away from the impact site is simply the ratio between the volume of ejecta at this distance and the surface area occupied by landed ejecta,

$$t(r) = \frac{V_e(r)}{A_e(r)} \tag{6.4}$$

the volume of ejecta at some distance is (Richardson, 2009),

$$V_e(r) = \frac{5}{4} \frac{\pi K_g \rho_t}{\rho_i} \left({r_{n+1}}^3 - {r_n}^3 \right) \tag{6.5}$$

where n is the index of the nth Z-shell.

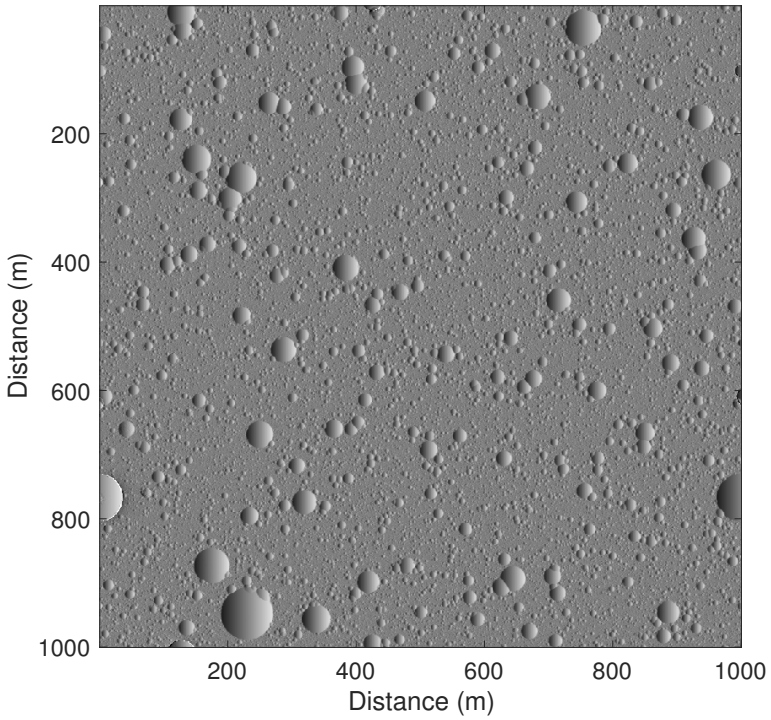

Figure 6.2: A model run simulating 1 Ga old surface on the Moon, without accounting for ejecta. Crater scaling laws Eq. 6.3 are used to link the impactor energy and the size of the final crater.

Similarly, the surface area is,

$$A(r) = \pi \left(l_n^2 - l_{n+1}^2 \right) \tag{6.6}$$

where l_n is the landing distance of the ejecta launched from the nth Z-shell. We refer the reader to Richardson (2009) for the full derivation of l, which itself depends on the ejecta velocity.

6.1.3 Mass Wasting and Seismic Slope Diffusion

Mass wasting is the process in which regolith fines and bedrock fragments slide down crater walls due to natural downslope diffusion encouraged by impacts and seismic activity. It has long been suspected mass wasting may protect ice trapped in polar craters by covering it quickly after impact (Arnold, 1979; Moses et al., 1999). However, in order to preserve ice, the downslope mass diffusion rate must be greater or at least comparable to the sublimation rate.

On smaller planetary bodies, seismic shaking was shown to be highly effective in generating mass wasting. In the case of asteroids and comets, impact induced seismicity was even shown to cause crater erasure over short time periods (Richardson Jr et al., 2005; Thomas et al., 2006). Since the efficiency of these processes is determined by the ratio of the seismic acceleration to the gravitational acceleration, their effect on the topography of the Moon is much more limited.

However, as shown in Chapter 1, even a thin layer of regolith may be sufficient to significantly increase the stability of cold-trapped ice. To verify whether downslope diffusion could potentially be a significant source of protective regolith, we couple observations conducted on the Moon with model simulations after Richardson (2009).

6.2 Preliminary Results

6.2.1 The Role of Ejecta and Mass Wasting in Protecting Cold-Trapped Ice

In order to estimate the rate of downslope regolith diffusion on the Moon, we measure the thickness of the lunar regolith inside large simple craters building upon previous studies. As the floors of polar craters are obscured by the permanent shadow they case, we conduct our analysis on equatorial craters assuming the mechanical behavior of illuminated regolith should be similar in both regions.

Stopar et al. (2017) found fresh craters $< 100-150$ m do not penetrate the upper layer of the fluffy highlands regolith and are consequently shallower compared to larger simple craters. Here we adopt this method and measure the depth to diameter (d/D) distribution of 1004 craters $50 - 1000$ m found on the floors of large (7 km $-$ 15 km) highlands simple craters, comparing them to the d/D distribution of craters of similar sizes that are found in the intercrater terrain. We measure craters' dimensions on digital elevation models derived using stereo images obtained by the Lunar Reconnaissance Orbiter Camera (LROC, Robinson et al. (2010)). We sample two perpendicular transect profiles passing through the crater center, and determine the crater diameter by measuring the rim-to-rim distance and the crater depth by measuring the difference between the average height of the rims and the lowest point on the crater floor. Stopar et al. (2017) demonstrated the d/D of small craters classified in images as fresh decreases with crater diameter. Building upon their methodology, we bin craters by diameter and calculate the representative maximum crater depth in each bin, abbreviated here as d_{95}. d_{95} is determined by averaging the depth of craters found above the 95_{th} percentile depth in each bin, and is a more statistically robust alternative to the maximum crater depth in the bin.

The results of this exploratory analysis are shown in Figure 6.3. The red and blue lines show d_{95} for small craters in the intercrater terrain and on the floor of impact craters, respectively. The red line shows a turning point at $\sim$ 100 m, similar to the one demonstrated by Stopar et al. (2017), while the blue line shows a turning point at $\sim$ 300 m. Adopting

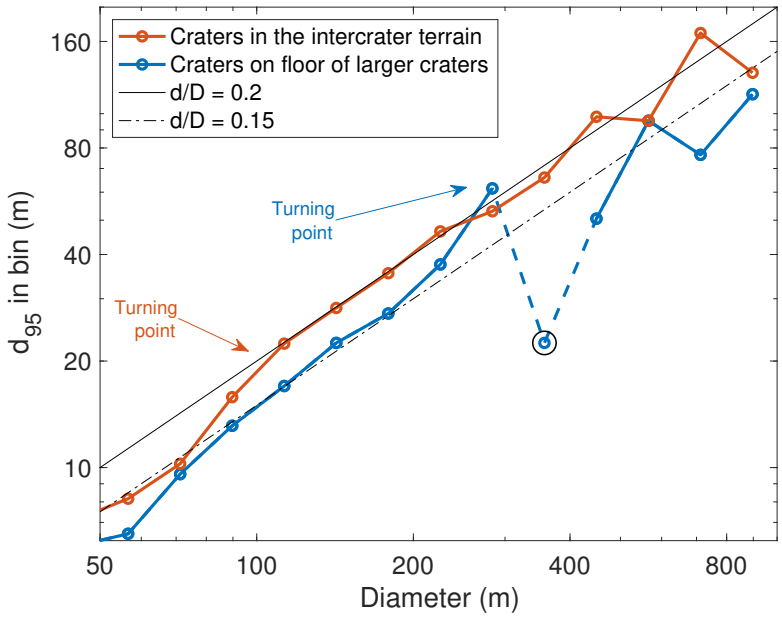

Figure 6.3: The depth of simple craters outside (red) and inside (blue) larger craters. Deep fresh craters in the intercrater terrain become shallower with diameter below $\sim$ 100 m, while craters located on the floors of larger craters become shallower at $\sim$ 300 m. This implies the regolith inside large impact craters is about three times thicker than the average regolith in the lunar highlands. The blue data point surrounded by a black circle indicates a significantly shallow crater bin, possibly due to the lower density of craters at this size range inside larger craters. The statistical scatter is expected to decrease as more data is obtained in the future.

Stopar et al. (2017) interpretation, this potentially implies regolith found on the floor of large simple craters is about three times thicker than the average regolith in the lunar highlands. These results qualitatively agree with model prediction, who found regolith in craters is a few time thicker compared to regolith in the intercrater terrain (Shoemaker et al., 1969; Fassett and Thomson, 2014). It should be emphasized the statistical scatter is expected to decrease as more data is obtained in the future.

This preliminary survey demonstrates regolith production in craters may accelerate ice burial trapped within polar cold-traps. Using our model, we may now compare the rate of ice sublimation to the rate of ice burial.

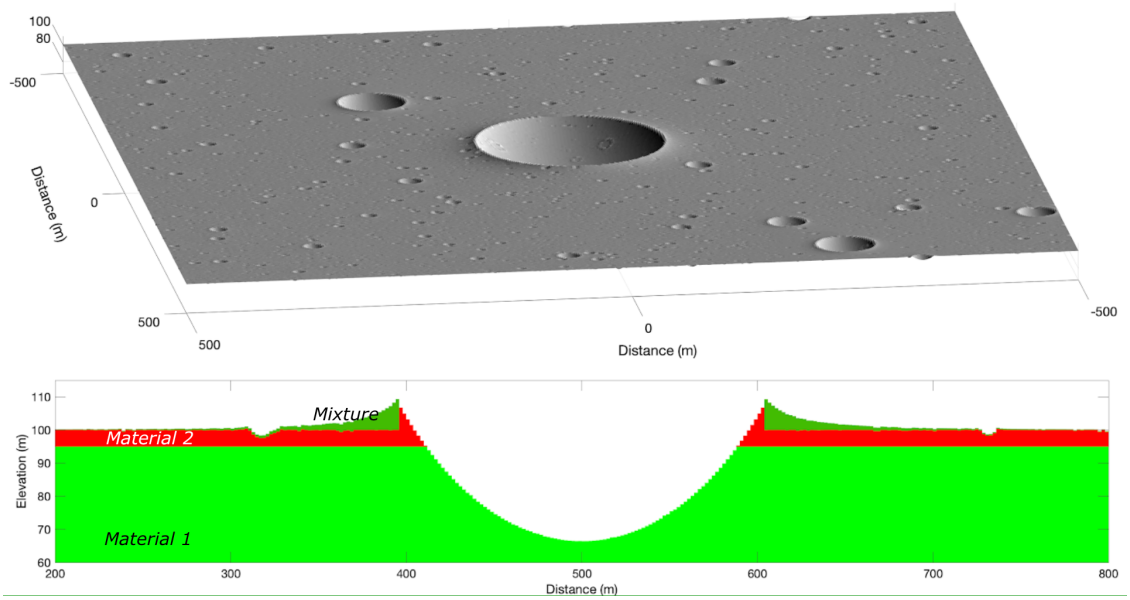

Figure 6.4: We simulate ice burial by regolith following slope diffusion and ejecta. A layer of ice (red) is initially placed on the surface, and a large crater excavates regolith from the subsurface (green), burying the ice. Subsequent seismic shaking diffuse regolith downslope occurs between crater emplacements, increasing the thickness of the regolith diffusion barrier.

In Figure 6.4 we show an example simulation for such ice burial scenario. A thick layer of ice (red) is emplaced on the surface and allowed to sublimate at a rate of 1 m Ga^{-1}. After some time has passed, a large crater forms, excavating regolith which buries the ice. The sublimation rate of the ice that is now buried under more than a few centimeters of regolith decreases significantly to $\sim 10^{-2}$ mm Ga^{-1}, rendering it much more thermally stable. Closer to the crater we see the protective sublimation lag also acts as a physical barrier, preventing small impactors from re-exposing the ice to the harms of space.

6.3 Conclusions and Future Work

Over the course of this work my colleagues and I have attempted to explain the observed difference in the amount of water ice trapped near the poles of Mercury and the Moon. By relating surface roughness, temperatures and ice stability we have estimated the area fraction of stable water ice on the Moon and proposed a method to explore ice trapped in sub-resolution topography. Later, we employed our model to conclude the presence of micro cold-traps on Mercury, whose volume helped constrain the age of cold-trapped volatiles on the planet.

Finally, as sometimes occurs in scientific exploration, our attempt to further constrain the thickness of ice deposits on Mercury and the Moon has led us to revisit our original hypothesis of the difference between them. The results of the study described in Chapter 5 suggests the difference in the amount of volatiles may not be as significant as previously thought. Instead, we postulate ice deposits on the Moon should be less pure compared to ice deposits on Mercury. This question, along with the preliminary results discussed above, will serve as a basis for two future investigations.

The first will deal with comparing the burial and sublimation rates of ices on the Moon and Mercury in an attempt to resolve the apparent differences between them. The goal of me and my colleagues is to use the model presented in this chapter to resolve some of the questions raised in Chapter 4 and 5. To resolve how pristine ice deposits can survive on

Mercury but not on the Moon, we intend to explore the role of the darkened sublimation lag in protecting it from mechanical and thermal erosion. Exploiting the unique capabilities of our $3-D$ impact gardening model, we hope to provide a mechanism that would explain the formation of thick layers of radar-invisible, icy-regolith deposits in small craters on the Moon, postulating the accelerated mass wasting within smaller craters may aid the process relative to larger, complex craters.

The second study will focus on evaluating the role of mass wasting in driving ice burial and other geologic processes on the Moon. In order to investigate the efficiency of this highly complex process in sub-g accelerations, we are in the process of conducting a series of experiments employing a seismic shaker and simulant powder which mimics the physical properties of the lunar regolith.

There is a famous saying in Hebrew, *"Tam Velo Nishlam"*, which may be translated as "over, but not done". As I write these final words it feels this proverb most appropriately concludes my work, which will always - much like many other scientific investigations - be a work in progress.

Bibliography

Robert J Adler. *The Geometry of Random Fields*. SIAM, 2010.

Oded Aharonson and Norbert Schorghofer. Subsurface ice on Mars with rough topography. *J. Geophys. Res.: Planets*, 111(E11):E11007, 2006.

James R Arnold. Ice in the lunar polar regions. *Journal of Geophysical Research: Solid Earth*, 84(B10):5659–5668, 1979.

JR Arnold. Monte carlo simulation of turnover processes in the lunar regolith. In *Lunar and Planetary Science Conference Proceedings*, volume 6, pages 2375–2395, 1975.

HD Baehr and K Stephan. *Heat and Mass Transfer*. Springer-Verlag Berlin Heidelberg, 3rd edition, 2011.

Joshua L Bandfield, Paul O Hayne, Jean-Pierre Williams, Benjamin T Greenhagen, and David A Paige. Lunar surface roughness derived from lro diviner radiometer observations. *Icarus*, 248:357–372, 2015.

Carl M. Bender and Steven A. Orszag. *Advanced Mathematical Methods for Scientists and Engineers I: Asymptotic Methods and Perturbation Theory*. Springer Science & Business Media, 2013.

EB Bierhaus, Alfred S McEwen, SJ Robbins, KN Singer, L Dones, MR Kirchoff, and J-P Williams. Secondary craters and ejecta across the solar system: Populations and effects on impact-crater–based chronologies. *Meteoritics & Planetary Science*, 53(4):638–671, 2018.

William F Bottke Jr, Daniel D Durda, David Nesvornỳ, Robert Jedicke, Alessandro Morbidelli, David Vokrouhlickỳ, and Hal Levison. The fossilized size distribution of the main asteroid belt. *Icarus*, 175(1):111–140, 2005.

Christophe Bourlier, Gérard Berginc, and Joseph Saillard. One-and two-dimensional shadowing functions for any height and slope stationary uncorrelated surface in the monostatic

and bistatic configurations. *IEEE Transactions on Antennas and Propagation*, 50(3):312–324, 2002.

Peter Brown, RE Spalding, Douglas O ReVelle, E Tagliaferri, and SP Worden. The flux of small near-earth objects colliding with the earth. *Nature*, 420(6913):294, 2002.

Charles E Bryson III, Victor Cazcarra, and Leonard L Levenson. Sublimation rates and vapor pressures of water, carbon dioxide, nitrous oxide, and xenon. *Journal of Chemical and Engineering Data*, 19(2):107–110, 1974.

Edgar Buckingham. On physically similar systems; illustrations of the use of dimensional equations. *Physical review*, 4(4):345, 1914.

David Buhl, William J Welch, and Donald G Rea. Reradiation and thermal emission from illuminated craters on the lunar surface. *Journal of Geophysical Research*, 73(16):5281–5295, 1968.

Bonnie J Buratti, John K Hillier, and Michael Wang. The lunar opposition surge: Observations by clementine. *Icarus*, 124(2):490–499, 1996.

Bryan J Butler. The migration of volatiles on the surfaces of mercury and the moon. *Journal of Geophysical Research: Planets*, 102(E8):19283–19291, 1997.

Bryan J Butler, Duane O Muhleman, and Martin A Slade. Mercury: full-disk radar images and the detection and stability of ice at the north pole. *Journal of Geophysical Research: Planets*, 98(E8):15003–15023, 1993.

Donald B Campbell, Bruce A Campbell, Lynn M Carter, Jean-Luc Margot, and Nicholas JS Stacy. No evidence for thick deposits of ice at the lunar south pole. *Nature*, 443(7113): 835–837, 2006.

John F Cavanaugh, James C Smith, Xiaoli Sun, Arlin E Bartels, Luis Ramos-Izquierdo, Danny J Krebs, Jan F McGarry, Raymond Trunzo, Anne Marie Novo-Gradac, Jamie L

Britt, et al. The mercury laser altimeter instrument for the messenger mission. *Space Science Reviews*, 131(1-4):451–479, 2007.

Nancy L Chabot, Carolyn M Ernst, Brett W Denevi, et al. Areas of permanent shadow in mercury's south polar region ascertained by messenger orbital imaging. *Geophysical Research Letters*, 39(9), 2012.

Nancy L Chabot, Carolyn M Ernst, Brett W Denevi, et al. Images of surface volatiles in mercurys polar craters acquired by the messenger spacecraft. *Geology*, 42(12):1051–1054, 2014.

Nancy L Chabot, Carolyn M Ernst, David A Paige, et al. Imaging mercury's polar deposits during messenger's low-altitude campaign. *Geophysical Research Letters*, 43(18):9461–9468, 2016.

Nancy L Chabot, Evangela E Shread, and John K Harmon. Investigating mercury's south polar deposits: Arecibo radar observations and high-resolution determination of illumination conditions. *Journal of Geophysical Research: Planets*, 123(2):666–681, 2018.

Wh-Hsun Cheng. *Methanol production and use*. CRC Press, 1994.

James S. Chickos and William E. Acree Jr. Enthalpies of sublimation of organic and organometallic compounds. *Journal of Physical and Chemical Reference Data*, 31(2): 537–698, 2002.

Gordon Chin, Scott Brylow, Marc Foote, James Garvin, Justin Kasper, John Keller, Maxim Litvak, Igor Mitrofanov, David Paige, Keith Raney, et al. Lunar reconnaissance orbiter overview: Theáinstrument suite and mission. *Space Science Reviews*, 129(4):391–419, 2007.

Anthony Colaprete, Peter Schultz, Jennifer Heldmann, Diane Wooden, Mark Shirley, Kimberly Ennico, Brendan Hermalyn, William Marshall, Antonio Ricco, Richard C Elphic, et al. Detection of water in the lcross ejecta plume. *science*, 330(6003):463–468, 2010.

E Costello, Rebecca R Ghent, and Paul G Lucey. The mixing of regolith on the moon and beyond; a model refreshed. *AGU Fall Meeting*, 2017a.

ES Costello, RR Ghent, and PG Lucey. A refreshed model for the mixing rate of lunar regolith. In *Lunar and Planetary Science Conference*, volume 48, 2017b.

J Crank and P Nicolson. A practical method for numerical evaluation of solutions of partial differential equations of the heat-conduction type. In *Mathematical Proceedings of the Cambridge Philosophical Society*, volume 43, pages 50–67. Cambridge Univ. Press, 1947.

Dana Hurley Crider and Richard R Vondrak. The solar wind as a possible source of lunar polar hydrogen deposits. *Journal of Geophysical Research: Planets*, 105(E11):26773–26782, 2000.

Dana Hurley Crider and Richard R Vondrak. Space weathering effects on lunar cold trap deposits. *Journal of Geophysical Research: Planets*, 108(E7), 2003.

BJR Davidsson and H Rickman. Surface roughness and three-dimensional heat conduction in thermophysical models. *Icarus*, 243:58–77, 2014.

BJR Davidsson, H Rickman, JL Bandfield, et al. Interpretation of thermal emission. i. the effect of roughness for spatially resolved atmosphereless bodies. *Icarus*, 252:1–21, 2015.

Morris H DeGroot and Mark J Schervish. *Probability and Statistics*. Pearson Education, 2012.

Marco Delbo, Michael Mueller, Joshua P Emery, Ben Rozitis, and Maria Teresa Capria. Asteroid thermophysical modeling. *Asteroids IV*, pages 107–128, 2015.

ML Delitsky, DA Paige, MA Siegler, et al. Ices on mercury: Chemistry of volatiles in permanently cold areas of mercury's north polar region. *Icarus*, 281:19–31, 2017.

RM Dell and RA Beebe. Heats of adsorption of polar molecules on carbon surfaces. ii. ammonia and methyl-amine. *The Journal of Physical Chemistry*, 59(8):754–762, 1955.

AN Deutsch, JW Head, GA Neumann, et al. Constraining the depth of polar ice deposits and evolution of cold traps on mercury with small craters in permanently shadowed regions. In *Lunar and Planetary Science Conference*, volume 48, 2017a.

Ariel N Deutsch, Nancy L Chabot, Erwan Mazarico, Carolyn M Ernst, James W Head, Gregory A Neumann, and Sean C Solomon. Comparison of areas in shadow from imaging and altimetry in the north polar region of mercury and implications for polar ice deposits. *Icarus*, 280:158–171, 2016.

Ariel N Deutsch, Gregory A Neumann, and James W Head. New evidence for surface water ice in small-scale cold traps and in three large craters at the north polar region of mercury from the mercury laser altimeter. *Geophysical Research Letters*, 44(18):9233–9241, 2017b.

JS Dohnanyi. Collisional model of asteroids and their debris. *Journal of Geophysical Research*, 74(10):2531–2554, 1969.

Deborah L Domingue, Scott L Murchie, Nancy L Chabot, et al. Mercury's spectrophotometric properties: Update from the mercury dual imaging system observations during the third messenger flyby. *Planetary and Space Science*, 59(15):1853–1872, 2011.

JP Emery, AL Sprague, FC Witteborn, et al. Mercury: Thermal modeling and mid-infrared (5-12 μm) observations. *Icarus*, 136(1):104–123, 1998.

Wenzhe Fa and Mark A Wieczorek. Regolith thickness over the lunar nearside: Results from earth-based 70-cm arecibo radar observations. *Icarus*, 218(2):771–787, 2012.

Wenzhe Fa, Yuzhen Cai, Zhiyong Xiao, et al. Topographic roughness of the northern high latitudes of mercury from messenger laser altimeter data. *Geophysical Research Letters*, 43(7):3078–3087, 2016.

Caleb I Fassett and Bradley J Thomson. Crater degradation on the lunar maria: Topographic diffusion and the rate of erosion on the moon. *Journal of Geophysical Research: Planets*, 119(10):2255–2271, 2014.

W C Feldman, S Maurice, AB Binder, BL Barraclough, RC Elphic, and DJ Lawrence. Fluxes of fast and epithermal neutrons from lunar prospector: Evidence for water ice at the lunar poles. *Science*, 281(5382):1496–1500, 1998.

William C Feldman, Sylvestre Maurice, David Jeffery Lawrence, Robert C Little, SL Lawson, O Gasnault, Roger C Wiens, Bruce L Barraclough, Richard C Elphic, Thomas H Prettyman, et al. Evidence for water ice near the lunar poles. *Journal of Geophysical Research: Planets*, 106(E10):23231–23251, 2001.

AGM Ferreira and LQ Lobo. The sublimation of argon, krypton, and xenon. *The Journal of Chemical Thermodynamics*, 40(12):1621–1626, 2008.

Elizabeth A Fisher, Paul G Lucey, Myriam Lemelin, Benjamin T Greenhagen, Matthew A Siegler, Erwan Mazarico, Oded Aharonson, Jean-Pierre Williams, Paul O Hayne, Gregory A Neumann, et al. Evidence for surface water ice in the lunar polar regions using reflectance measurements from the lunar orbiter laser altimeter and temperature measurements from the diviner lunar radiometer experiment. *Icarus*, 292:74–85, 2017.

DE Gault, F Horz, DE Brownlee, and JB Hartung. Mixing of the lunar regolith. In *Lunar and Planetary Science Conference Proceedings*, volume 5, pages 2365–2386, 1974.

T. Hagfors. Backscattering from an undulating surface with applications to radar returns from the moon. *J. Geophys. Res.*, 69(18):3779–3784, 1964.

T Hagfors. Remote probing of the moon by infrared and microwave emissions and by radar. *Radio Science*, 5(2):189–227, 1970.

B Hapke. Applications of an energy transfer model to three problems in planetary regoliths: The solid-state greenhouse, thermal beaming, and emittance spectra. *Journal of Geophysical Research: Planets (1991-2012)*, 101(E7):16833–16840, 1996.

Bruce Hapke. Bidirectional reflectance spectroscopy: 1. theory. *J. Geophys. Res.: Solid Earth*, 86(B4):3039–3054, 1981.

Bruce Hapke. Bidirectional reflectance spectroscopy: 4. the extinction coefficient and the opposition effect. *Icarus*, 67(2):264–280, 1986.

JK Harmon and MA Slade. Radar mapping of mercury: Full-disk images and polar anomalies. *Science*, 258(5082):640–643, 1992.

John K Harmon, Phil J Perillat, and Martin A Slade. High-resolution radar imaging of mercury's north pole. *Icarus*, 149(1):1–15, 2001.

John K Harmon, Martin A Slade, et al. Radar imagery of mercurys putative polar ice: 1999–2005 arecibo results. *Icarus*, 211(1):37–50, 2011.

Junichi Haruyama, Makiko Ohtake, Tsuneo Matsunaga, Tomokatsu Morota, Chikatoshi Honda, Yasuhiro Yokota, Masanao Abe, Yoshiko Ogawa, Hideaki Miyamoto, Akira Iwasaki, et al. Long-lived volcanism on the lunar farside revealed by selene terrain camera. *Science*, 323(5916):905–908, 2009.

S Edward Hawkins, John D Boldt, Edward H Darlington, Raymond Espiritu, Robert E Gold, Bruce Gotwols, Matthew P Grey, Christopher D Hash, John R Hayes, Steven E Jaskulek, et al. The mercury dual imaging system on the messenger spacecraft. *Space Science Reviews*, 131(1-4):247–338, 2007.

Paul O Hayne, Joshua L Bandfield, Matthew A Siegler, et al. Global regolith thermophysical properties of the moon from the diviner lunar radiometer experiment. *Journal of Geophysical Research (Planets)*, 122:2371–2400, 2017.

PO Hayne and O Aharonson. Thermal stability of ice on ceres with rough topography. *Journal of Geophysical Research: Planets*, 120(9):1567–1584, 2015.

G Heiken, D Vaniman, and BM French. *Lunar sourcebook: A user's guide to the Moon*. CUP Archive, 1991.

Paul Helfenstein and Michael K Shepard. Submillimeter-scale topography of the lunar regolith. *Icarus*, 141(1):107–131, 1999.

MR Henriksen, MR Manheim, KN Burns, P Seymour, EJ Speyerer, A Deran, AK Boyd, E Howington-Kraus, MR Rosiek, BA Archinal, et al. Extracting accurate and precise topography from lroc narrow angle camera stereo observations. *Icarus*, 283:122–137, 2017.

KA Holsapple. The scaling of impact processes in planetary sciences. *Annual review of earth and planetary sciences*, 21(1):333–373, 1993.

KA Holsapple and RM Schmidt. Point source solutions and coupling parameters in cratering mechanics. *Journal of Geophysical Research: Solid Earth*, 92(B7):6350–6376, 1987.

John R Howell, M Pinar Menguc, and Robert Siegel. *Thermal Radiation Heat Transfer*. CRC Press, sixth edition, 2015.

DM Hurley, DJ Lawrence, DB J Bussey, et al. Two-dimensional distribution of volatiles in the lunar regolith from space weathering simulations. *Geophysical Research Letters*, 39(9), 2012.

Harold Edwin Hurst. Long-term storage capacity of reservoirs. *Trans. Amer. Soc. Civil Eng.*, 116:770–799, 1951.

Andrew P Ingersoll, Tomas Svitek, and Bruce C Murray. Stability of polar frosts in spherical bowl-shaped craters on the moon, mercury, and mars. *Icarus*, 100(1):40–47, 1992.

S Jamsa, JI Peltoniemi, and K Lumme. Thermal emission from a rough surface: Ray optics approach. *Astronomy and Astrophysics*, 271:319, 1993.

SJ Keihm and MG Langseth Jr. Surface brightness temperatures at the apollo 17 heat flow site: Thermal conductivity of the upper 15 cm of regolith. In *Lunar and Planetary Science Conference Proceedings*, volume 4, page 2503, 1973.

Laura Kerber, James W Head, Sean C Solomon, et al. Explosive volcanic eruptions on mercury: Eruption conditions, magma volatile content, and implications for interior volatile abundances. *Earth and Planetary Science Letters*, 285(3):263–271, 2009.

AA Kokhanov, MA Kreslavsky, and IP Karachevtseva. Small impact craters in the polar regions of the moon: peculiarities of morphometric characteristics. *Solar System Research*, 49(5):295–302, 2015.

Mikhail A Kreslavsky, James W Head, Gregory A Neumann, Margaret A Rosenburg, Oded Aharonson, David E Smith, and Maria T Zuber. Lunar topographic roughness maps from lunar orbiter laser altimeter (lola) data: Scale dependence and correlation with geologic features and units. *Icarus*, 226(1):52–66, 2013.

David Kushner. The wizardry of id. *IEEE Spectrum*, 39(8):42–47, 2002.

JSV Lagerros. Thermal physics of asteroids. iii. irregular shapes and albedo variegations. *Astronomy and Astrophysics*, 325:1226–1236, 1997.

I Langmuir. The vapor pressure of metallic tungsten. *Physical Review*, 2(5):329, 1913.

MG Langseth, SJ Keihm, and K Peters. Revised lunar heat-flow values. In *Lunar and Planetary Science Conference Proceedings*, pages 3143–3171, 1976.

LJ Lanzerotti, WL Brown, and RE Johnson. Ice in the polar regions of the moon. *Journal of Geophysical Research: Solid Earth*, 86(B5):3949–3950, 1981.

David J Lawrence. A tale of two poles: Toward understanding the presence, distribution, and origin of volatiles at the polar regions of the moon and mercury. *Journal of Geophysical Research: Planets*, 122(1):21–52, 2017.

David J Lawrence, William C Feldman, John O Goldsten, Sylvestre Maurice, Patrick N Peplowski, Brian J Anderson, David Bazell, Ralph L McNutt, Larry R Nittler, Thomas H Prettyman, et al. Evidence for water ice near mercurys north pole from messenger neutron spectrometer measurements. *Science*, 339(6117):292–296, 2013.

Mathieu Le Feuvre and Mark A Wieczorek. Nonuniform cratering of the moon and a revised crater chronology of the inner solar system. *Icarus*, 214(1):1–20, 2011.

Shuai Li, Paul G Lucey, Ralph E Milliken, Paul O Hayne, Elizabeth Fisher, Jean-Pierre Williams, Dana M Hurley, and Richard C Elphic. Direct evidence of surface exposed water ice in the lunar polar regions. *Proceedings of the National Academy of Sciences*, 115 (36):8907–8912, 2018.

Xiaowen Li, Alan H Strahler, and Mark A Friedl. A conceptual model for effective directional emissivity from nonisothermal surfaces. *IEEE Transactions on Geoscience and Remote Sensing*, 37(5):2508–2517, 1999.

Yang Liu, Yunbin Guan, Youxue Zhang, George R Rossman, John M Eiler, and Lawrence A Taylor. Direct measurement of hydroxyl in the lunar regolith and the origin of lunar surface water. *Nature Geoscience*, 5(11):779–782, 2012.

Stéphanie Lucas, Daniel Ferry, Benjamin Demirdjian, and Jean Suzanne. Vapor pressure and solid phases of methanol below its triple point temperature. *The Journal of Physical Chemistry B*, 109(38):18103–18106, 2005.

A Mainzer, T Grav, J Masiero, J Bauer, RM Cutri, RS McMillan, CR Nugent, D Tholen, R Walker, and EL Wright. Physical parameters of asteroids estimated from the wise 3-band data and neowise post-cryogenic survey. *The Astrophysical Journal Letters*, 760(1): L12, 2012.

A Mainzer, J Bauer, T Grav, J Masiero, RM Cutri, E Wright, CR Nugent, R Stevenson, E Clyne, G Cukrov, et al. The population of tiny near-earth objects observed by neowise. *The Astrophysical Journal*, 784(2):110, 2014.

D. E. Maxwell. Simple Z model for cratering, ejection, and the overturned flap. In D. J. Roddy, R. O. Pepin, and R. B. Merrill, editors, *Impact and Explosion Cratering: Planetary and Terrestrial Implications*, pages 1003–1008, Jan 1977.

E Mazarico, GA Neumann, DE Smith, et al. Illumination conditions of the lunar polar regions using lola topography. *Icarus*, 211(2):1066–1081, 2011.

TP McClanahan, IG Mitrofanov, William V Boynton, et al. Evidence for the sequestration of hydrogen-bearing volatiles towards the moons southern pole-facing slopes. *Icarus*, 255: 88–99, 2015.

Alfred S McEwen, Lisa R Gaddis, Gerhard Neukum, Harald Hoffman, Carle M Pieters, and James W Head. Galileo observations of post-imbrium lunar craters during the first eearth-moon flyby. *Journal of Geophysical Research: Planets*, 98(E9):17207–17231, 1993.

AJ McGovern, BD Bussey, BT Greenhagen, et al. Mapping and characterization of non-polar permanent shadows on the lunar surface. *Icarus*, 223(1):566–581, 2013.

DS McKay, RM Fruland, and GH Heiken. Grain size and the evolution of lunar soils. In *Lunar and Planetary Science Conference Proceedings*, volume 5, pages 887–906, 1974.

H Jay Melosh. Impact cratering: A geologic process. *Research supported by NASA. New York, Oxford University Press (Oxford Monographs on Geology and Geophysics, No. 11), 1989, 253 p.*, 11, 1989.

MA Melvin. Blackbody radiation and lambert's law. *American Journal of Physics*, 23(8): 508–510, 1955.

Michael I Mishchenko. Asymmetry parameters of the phase function for densely packed scattering grains. *Journal of Quantitative Spectroscopy and Radiative Transfer*, 52(1): 95–110, 1994.

I G Mitrofanov, A B Sanin, William V Boynton, G Chin, JB Garvin, D Golovin, LG Evans, K Harshman, AS Kozyrev, ML Litvak, et al. Hydrogen mapping of the lunar south pole using the lro neutron detector experiment lend. *science*, 330(6003):483–486, 2010.

TH Morgan and DE Shemansky. Limits to the lunar atmosphere. *Journal of Geophysical Research: Space Physics*, 96(A2):1351–1367, 1991.

Julianne I Moses, Katherine Rawlins, Kevin Zahnle, and Luke Dones. External sources of water for mercury's putative ice deposits. *Icarus*, 137(2):197–221, 1999.

CD Neish, DT Blewett, JK Harmon, et al. A comparison of rayed craters on the moon and mercury. *Journal of Geophysical Research: Planets*, 118(10):2247–2261, 2013.

GA Neumann, X Sun, E Mazarico, et al. Latitudinal variations in mercury's reflectance from the mercury laser altimeter. In *Lunar and Planetary Science Conference*, volume 48, 2017.

Gregory A Neumann, John F Cavanaugh, Xiaoli Sun, et al. Bright and dark polar deposits on mercury: Evidence for surface volatiles. *Science*, 339(6117):296–300, 2013.

Stewart Nozette, Paul Spudis, Ben Bussey, Robert Jensen, Keith Raney, Helene Winters, Christopher L Lichtenberg, William Marinelli, Jason Crusan, Michele Gates, et al. The lunar reconnaissance orbiter miniature radio frequency (mini-rf) technology demonstration. *Space Science Reviews*, 150(1-4):285–302, 2010.

VR Oberbeck, WL Quaide, M Mahan, and J Paulson. Monte carlo calculations of lunar regolith thickness distributions. *Icarus*, 19(1):87–107, 1973.

Lissa Ong, Erik I Asphaug, and Donald others Korycansky. Volatile retention from cometary impacts on the moon. *Icarus*, 207(2):578–589, 2010.

DA Paige, MC Foote, BT Greenhagen, JT Schofield, S Calcutt, AR Vasavada, DJ Preston, FW Taylor, CC Allen, KJ Snook, et al. The lunar reconnaissance orbiter diviner lunar radiometer experiment. *Space Science Reviews*, 150(1-4):125–160, 2010a.

DA Paige, PO Hayne, MA Siegler, et al. Dark surface deposits in the north polar region of mercury: Evidence for widespread small-scale volatile cold traps. In *Lunar and Planetary Science Conference*, volume 45, page 2501, 2014.

David A Paige, Stephen E Wood, and Ashwin R Vasavada. The thermal stability of water ice at the poles of mercury. *Science*, 258(5082):643–646, 1992.

David A Paige, Matthew A Siegler, Jo Ann Zhang, Paul O Hayne, Emily J Foote, Kristen A Bennett, Ashwin R Vasavada, Benjamin T Greenhagen, John T Schofield, Daniel J Mc-

Cleese, et al. Diviner lunar radiometer observations of cold traps in the moons south polar region. *science*, 330(6003):479–482, 2010b.

David A Paige, Matthew A Siegler, John K Harmon, et al. Thermal stability of volatiles in the north polar region of mercury. *Science*, 339(6117):300–303, 2013.

Edison Pettit and Seth B Nicholson. Lunar radiation and temperatures. *Astrophys. J.*, 71: 102–135, 1930.

RJ Pike. Apparent depth/apparent diameter relation for lunar craters. In *Lunar and Planetary Science Conference Proceedings*, volume 8, pages 3427–3436, 1977.

James E Richardson. Cratering saturation and equilibrium: A new model looks at an old problem. *Icarus*, 204(2):697–715, 2009.

James E Richardson, H Jay Melosh, Carey M Lisse, and Brian Carcich. A ballistics analysis of the deep impact ejecta plume: Determining comet tempel 1's gravity, mass, and density. *Icarus*, 191(2):176–209, 2007.

James E Richardson Jr, H Jay Melosh, Richard J Greenberg, and David P O'Brien. The global effects of impact-induced seismic activity on fractured asteroid surface morphology. *Icarus*, 179(2):325–349, 2005.

Mark S Robinson, Scott L Murchie, and David T others Blewett. Reflectance and color variations on mercury: Regolith processes and compositional heterogeneity. *Science*, 321 (5885):66–69, 2008.

MS Robinson, SM Brylow, M Tschimmel, D Humm, SJ Lawrence, PC Thomas, BW Denevi, E Bowman-Cisneros, J Zerr, MA Ravine, et al. Lunar reconnaissance orbiter camera (lroc) instrument overview. *Space science reviews*, 150(1-4):81–124, 2010.

M. A. Rosenburg, O. Aharonson, J. W. Head, M. A. Kreslavsky, E. Mazarico, G. A. Neumann, D. E. Smith, M. H. Torrence, and M. T. Zuber. Global surface slopes and roughness

of the moon from the lunar orbiter laser altimeter. *J. Geophys. Res.: Planets*, 116(E2): E02001, 2011a. doi: 10.1029/2010JE003716.

MA Rosenburg, Oded Aharonson, JW Head, MA Kreslavsky, E Mazarico, Gregory A Neumann, David E Smith, Mark H Torrence, and Maria T Zuber. Global surface slopes and roughness of the moon from the lunar orbiter laser altimeter. *Journal of Geophysical Research: Planets*, 116(E2), 2011b.

Margaret A Rosenburg, Oded Aharonson, and Re'em Sari. Topographic power spectra of cratered terrains: theory and application to the moon. *Journal of Geophysical Research: Planets*, 120(2):177–194, 2015.

Scott D Roth. Ray casting for modeling solids. *Computer graphics and image processing*, 18 (2):109–144, 1982.

Ben Rozitis and Simon F Green. Directional characteristics of thermal–infrared beaming from atmosphereless planetary surfaces–a new thermophysical model. *Monthly Notices of the Royal Astronomical Society*, 415(3):2042–2062, 2011.

L Rubanenko, E Mazarico, GA Neumann, and DA Paige. Evidence for surface and subsurface ice inside micro cold-traps on mercury's north pole. In *Lunar and Planetary Science Conference*, volume 48, 2017a.

L Rubanenko, E Mazarico, GA Neumann, and DA Paige. Ice in micro cold traps on mercury: Implications for age and origin. *Journal of Geophysical Research: Planets*, 123(8):2178–2191, 2018.

Lior Rubanenko and Oded Aharonson. Stability of ice on the moon with rough topography. *Icarus*, 296:99–109, 2017.

Lior Rubanenko, Paul O Hayne, and David A Paige. The effects of surface roughness on the apparent thermal and optical properties of the moon. *AGU Fall Meeting*, 2017b.

J M Saari, R W Shorthill, and D F Winter. The sunlit lunar surface. *The Moon*, 5(1–2): 179–199, 1972.

John M Saari, RW Shorthill, and TK Deaton. Infrared and visible images of the eclipsed moon of december 19, 1964. *Icarus*, 5(1-6):635–659, 1966.

Goran Salamunićcar, Sven Lončarić, Arne Grumpe, et al. Hybrid method for crater detection based on topography reconstruction from optical images and the new lu78287gt catalogue of lunar impact craters. *Advances in Space Research*, 53(12):1783–1797, 2014.

JR Salvail and FP Fanale. Near-surface ice on mercury and the moon: A topographic thermal model. *Icarus*, 111(2):441–455, 1994.

H Sato, Koichi Watanabe, JMH Levelt Sengers, John S Gallagher, Philip G Hill, Johannes Straub, and Wolfgang Wagner. Sixteen thousand evaluated experimental thermodynamic property data for water and steam. *Journal of physical and chemical reference data*, 20 (5):1023–1044, 1991.

N Schorghofer and O Aharonson. Stability and exchange of subsurface ice on mars. *Journal of Geophysical Research: Planets*, 110(E5), 2005.

N Schorghofer and O Aharonson. The lunar thermal ice pump. *The Astrophysical Journal*, 788(2):169, 2014.

Norbert Schorghofer. Two-dimensional description of surface-bounded exospheres with application to the migration of water molecules on the moon. *Physical Review E*, 91(5): 052154, 2015.

Norbert Schorghofer and G Jeffrey Taylor. Subsurface migration of h2o at lunar cold traps. *Journal of Geophysical Research: Planets*, 112(E2), 2007.

Manfred Schroeder. *Fractals, Chaos, Power Laws: Minutes from an Infinite Paradise*. Courier Corporation, 2009.

MR Schroeder. *Fractals, chaos, power laws: Minutes from an infinite paradise*. Courier Corporation, 2012.

Peter H Schultz and Jill Singer. A comparison of secondary craters on the moon, mercury, and mars. In *Lunar and Planetary Science Conference Proceedings*, volume 11, pages 2243–2259, 1980.

Michael K Shepard. *Introduction to planetary photometry*. Cambridge University Press, 2017.

Michael K Shepard, Bruce A Campbell, Mark H Bulmer, Tom G Farr, Lisa R Gaddis, and Jeffrey J Plaut. The roughness of natural terrain: A planetary and remote sensing perspective. *J. Geophys. Res.: Planets*, 106(E12):32777–32795, 2001.

E. M. Shoemaker, R. M. Batson, H. E. Holt, E. C. Morris, J. J. Rennilson, and E. A. Whitaker. Observations of the lunar regolith and the earth from the television camera on surveyor 7. *JGR*, 74(25):6081–6119, 1969. doi: 10.1029/JB074i025p06081.

MA Siegler, BG Bills, and DA Paige. Effects of orbital evolution on lunar ice stability. *Journal of Geophysical Research: Planets*, 116(E3), 2011.

MA Siegler, RS Miller, JT Keane, et al. Lunar true polar wander inferred from polar hydrogen. *Nature*, 531(7595):480–484, 2016.

William M Sinton. Temperatures on the lunar surface. In *Physics and Astronomy of the Moon*, pages 407–428. Academic Press New York, 1962.

Martin A Slade, Bryan J Butler, and Duane O Muhleman. Mercury radar imaging: Evidence for polar ice. *Science*, 258(5082):635–640, 1992.

B Smith. Geometrical shadowing of a random rough surface. *IEEE transactions on antennas and propagation*, 15(5):668–671, 1967a.

B.G. Smith. Lunar surface roughness: Shadowing and thermal emission. *J. Geophys. Res.*, 72(16):4059–4067, 1967b.

David E Smith, Maria T Zuber, Glenn B Jackson, John F Cavanaugh, Gregory A Neumann, Haris Riris, Xiaoli Sun, Ronald S Zellar, Craig Coltharp, Joseph Connelly, et al. The lunar orbiter laser altimeter investigation on the lunar reconnaissance orbiter mission. *Space science reviews*, 150(1-4):209–241, 2010.

Jose A Sobrino and Juan Cuenca. Angular variation of thermal infrared emissivity for some natural surfaces from experimental measurements. *Applied Optics*, 38(18):3931–3936, 1999.

Sean C Solomon, Ralph L McNutt Jr, Robert E Gold, Mario H Acuña, Daniel N Baker, William V Boynton, Clark R Chapman, Andrew F Cheng, George Gloeckler, James W Head Iii, et al. The messenger mission to mercury: Scientific objectives and implementation. *Planetary and Space Science*, 49(14-15):1445–1465, 2001.

Steven Soter and Juris Ulrichs. Rotation and heating of the planet mercury. *Nature*, 214 (5095):1315, 1967.

John R Spencer. A rough-surface thermophysical model for airless planets. *Icarus*, 83(1): 27–38, 1990.

Emerson J Speyerer, Reinhold Z Povilaitis, Mark S Robinson, et al. Quantifying crater production and regolith overturn on the moon with temporal imaging. *Nature*, 538(7624): 215, 2016.

PD Spudis, DBJ Bussey, SM Baloga, JTS Cahill, LS Glaze, GW Patterson, RK Raney, TW Thompson, BJ Thomson, and EA Ustinov. Evidence for water ice on the moon: Results for anomalous polar craters from the lro mini-rf imaging radar. *Journal of Geophysical Research: Planets*, 118(10):2016–2029, 2013.

NJS Stacy, DB Campbell, and PG Ford. Arecibo radar mapping of the lunar poles: A search for ice deposits. *Science*, 276(5318):1527–1530, 1997.

LAK Staveley, LQ Lobo, and JCG Calado. Triple-points of low melting substances and their use in cryogenic work. *Cryogenics*, 21(3):131–144, 1981.

Richard Montgomery Stephenson. *Handbook of the thermodynamics of organic compounds*. Springer Science & Business Media, 2012.

BD Stewart, E Pierazzo, DB Goldstein, et al. Simulations of a comet impact on the moon and associated ice deposition in polar cold traps. *Icarus*, 215(1):1–16, 2011.

JD Stopar, MS Robinson, EJ Speyerer, et al. Regolith characterization using lroc nac digital elevation models of small lunar craters. In *Lunar and Planetary Science Conference*, volume 43, page 2729, 2012.

Julie D Stopar, Mark S Robinson, Olivier S Barnouin, Alfred S McEwen, Emerson J Speyerer, Megan R Henriksen, and Sarah S Sutton. Relative depths of simple craters and the nature of the lunar regolith. *Icarus*, 298:34–48, 2017.

Y Sun. Statistical ray method for deriving reflection models of rough surfaces. *JOSA A*, 24 (3):724–744, 2007.

HCM Susorney, OS Barnouin, CM Ernst, and PK Byrne. The surface roughness of mercury from the mercury laser altimeter: Investigating the effects of volcanism, tectonism, and impact cratering. *Journal of Geophysical Research (Planets)*, 122:1372–1390, 2017.

Megan Bruck Syal, Peter H Schultz, and Miriam A Riner. Darkening of mercury's surface by cometary carbon. *Nature Geoscience*, 8(5):352–356, 2015.

Paul J Thomas, Roland D Hicks, Christopher F Chyba, and Christopher P McKay. *Comets and the Origin and Evolution of Life*. Springer Science & Business Media, 2006.

Harold Clayton Urey. *The planets: their origin and development*. Yale Univ. Press, 1952.

Hendrik Christoffel Van de Hulst. *Light scattering by small particles*. Courier Corporation, 1981.

Ashwin R Vasavada, David A Paige, and Stephen E Wood. Near-surface temperatures on mercury and the moon and the stability of polar ice deposits. *Icarus*, 141(2):179–193, 1999.

J Veverka, Paul Helfenstein, Bruce Hapke, et al. Photometry and polarimetry of mercury. *Mercury*, pages 37–58, 1988.

Karl J Vogler, Paul E Johnson, and Richard W Shorthill. Modeling the non-grey-body thermal emission from the full moon. *Icarus*, 92(1):80–93, 1991.

Kenneth Watson, Bruce C Murray, and Harrison Brown. The behavior of volatiles on the lunar surface. *Journal of Geophysical Research*, 66(9):3033–3045, 1961.

MS Westley, RA Baragiola, RE Johnson, and GA Baratta. Photodesorption from low-temperature water ice in interstellar and circumsolar grains. *Nature*, 373(6513):405, 1995.

DR Williams and GW Wetherill. Size distribution of collisionally evolved asteroidal populations: Analytical solution for self-similar collision cascades. *Icarus*, 107(1):117–128, 1994.

J-P Williams, DA Paige, BT Greenhagen, and E Sefton-Nash. The global surface temperatures of the moon as measured by the diviner lunar radiometer experiment. *Icarus*, 283: 300–325, 2017.

DF Winter and JM Saari. A particulate thermophysical model of the lunar soil. *The Astrophysical Journal*, 156:1135, 1969.

Warren J Wiscombe and Stephen G Warren. A model for the spectral albedo of snow. i: Pure snow. *Journal of the Atmospheric Sciences*, 37(12):2712–2733, 1980.

Jiunn-Jong Wu. Simulation of rough surfaces with fft. *Tribology International*, 33(1):47–58, 2000.

Marie Yseboodt and Jean-Luc Margot. Evolution of mercury's obliquity. *Icarus*, 181(2): 327–337, 2006.

Jo Ann Zhang and David A Paige. Cold-trapped organic compounds at the poles of the moon and mercury: Implications for origins. *Geophysical Research Letters*, 36(16), 2009.